Stratabound tungsten mineralisation in the Ivisaartoq Greenstone Belt, southern West Greenland

Thesis submitted for the degree of Master of Science

Diplomarbeit zur Erlangung des akademischen Grades eines Diplomingenieurs

Philipp Hartlieb

June, 2008

Supervisors

Ao. Prof. Dr. Johann G. Raith[1)]
Ao. Prof. Mag. Dr. Thomas Meisel[2)]

[1)] Department for Applied Geosciences and Geophysics
Chair of Mineralogy and Petrology, University of Leoben, Austria
[2)] Chair of General and Analytical Chemistry, University of Leoben, Austria

I declare in lieu of oath, that I wrote this thesis and performed the associated research myself, using only literature cited in this volume.

Philipp Hartlieb Leoben, June 2008

Table of Contents

1. ABSTRACT 1

2. ZUSAMMENFASSUNG 3

3. INTRODUCTION 5

4. REGIONAL GEOLOGY 7

4.1. GEOLOGICAL OVERVIEW AND GEOLOGICAL HISTORY 7

4.1.1. Itsaq Gneiss Complex 8

4.1.2. Terranes in the NE Nuuk region 10

4.1.3. Tectonic framework 11

4.2. THE LITHOSTRATIGRAPHY OF THE IVISAARTOQ GREENSTONE BELT (IGB) 12

4.3. FIELD OBSERVATIONS 15

4.3.1. General remarks 15

4.3.2. Pillow basalt structures and Type I calc-silicate alteration 15

4.3.2. Type II calc-silicate alteration 20

4.3.3. Scheelite mineralisation 24

4.3.4. Metapelitic rocks 25

4.3.5. Magnetic Marker 26

5. METHODS 27

5.1. MICROSCOPY 27

5.2. INDUCTIVELY COUPLED PLASMA – MASS SPECTROMETRY (ICP-MS) 27

5.2.1. Assembly of ICP-MS 27

5.2.2. Application in this study 29

5.3. X-RAY FLUORESCENCE ANALYSIS (XRF) 29

5.3.1. Principles of XRF analysis 29

5.3.2. Assembly of XRF instruments 31

5.3.3. XRF – analysis and this study 32

5.4. ELECTRON MICROPROBE ANALYSIS (EMP) 32

5.4.1. EMP and this study 33

6. PETROGRAPHY 35

6.2. CALC-SILICATE ROCKS 35

6.2.1. Type I calc-silicate rocks 35

6.2.2. Type II calc-silicate rocks 39

6.2.3. Scheelite-rich calc-silicate rocks 44

6.3. METAPELITIC ROCKS 47

7. MINERAL CHEMISTRY 54

8. GEOTHERMOBAROMETRY 58

9. GEOCHEMISTRY 62

9.1. PILLOW BASALTS AND TYPE I CALC-SILICATE ROCKS 62

9.1.1. Pillow rims 63

9.1.1.1 Major elements 63

9.1.1.2. Trace elements 63

9.1.1.3. Rare earth elements 66

9.1.2. Pillow basalt cores – calc-silicate rocks Type I 68

9.1.2.1. Major elements 68

9.1.2.2. Trace elements 68

9.1.2.3. Rare earth elements 69

9.2. CALC-SILICATE ROCKS OF TYPE II AND THEIR HOST ROCKS 70

9.2.1. Host rocks not affected by calc-silicate alteration 70

9.2.1.1. Major elements 70

9.2.1.2. Trace elements 70

9.2.1.3. Rare earth elements 73

9.2.2. Calc-silicate rocks of Type II 74

9.2.2.1. Major elements 74

9.2.2.2. Trace elements 74

9.2.2.3. Rare earth elements 75

9.2.3. Transition type rocks 77

9.2.3.1. Major elements 77

9.2.3.2. Trace elements 77

9.2.3.3. Rare earth elements 77

9.3 TUNGSTEN ENRICHED CALC-SILICATE ROCKS 79

9.3.1 Major elements 79

9.3.2. Trace elements 81

9.3.3. Rare earth elements 81

9.4. CHEMICAL CHARACTERISTICS OF CALC-SILICATE ALTERATIONS 82

9.4.1. Isocon calculations 82

9.4.1.1. Calc-silicate alteration (Type I) of pillow basalts 82

9.4.1.2. Type II calc-silicate alteration 85

9.4.2. Mass balance calculations 89

9.4.2.1. Calc-silicate alteration (Type I) of pillow basalts 89

9.4.2.2. Type II calc-silicate alteration 91

9.4.3. Element mobilities 92

9.4.3.1. Calc-silicate rocks Type I 92

9.4.3.2. Calc-silicate rocks Type II 94

9.4.4. Chemical changes in the transition zone vs Type II calc-silicate rocks 94

9.5. CLASSIFICATION OF METABASITES 96

10. DISCUSSION 98

10.1. COMPARISON OF THE TWO TYPES OF CALC-SILICATE ROCKS 98

10.2. STRATABOUND TUNGSTEN DEPOSITS 101
10.2.1. Overview about stratabound tungsten deposits 101
10.2.2. Genesis of tungsten mineralisation in the IGB 103
10.3. CONCLUSIONS 106

11. ACKNOWLWEDGMENTS 107

12. REFERENCES 108

13. APPENDICES 113

APPENDIX A – SAMPLE LIST 113
APPENDIX B 117
B1. EMP – data and calculated cations for sample C71B 117
B2. EMP – data and calculated cations for sample IV26F 120
B3. EMP – data and calculated cations for sample IV33 126
APPENDIX C 130
C1. Thermocalc 3.26, calculations for sample C71B 130
C2. Thermocalc 3.26, calculations for sample IV26F 132
C3. Thermocalc 3.26, calculations for sample IV33 134

1. Abstract

In the course of the project „Greenstone belts in the central Gothabsfjord region, southern West Greenland" carried out by the Geological Society of Denmark and Greenland (GEUS) Ao. Prof. Dr. Johann G. Raith did field work for several weeks in the summers 2004 and 2005 in the Ivisaartoq Greenstone Belt (IGB) focussing on stratabound tungsten mineralisation in this area. The samples taken and the field observations made during these field trips are the basis for this MSc thesis, which focused on discriminating the two occurring alteration types according to their geochemical behaviour as well as petrography and giving P/T estimations for metamoprhism. Aged ~3075 Ma the IGB is one of the Mesoarchaean greenstone belts in southern West Greenland. It is part of the so-called Kapisilik Terrane situated between the Isukasia and Færinghaven Terranes, which both contain Early Archean rocks. The rocks of the Kapisilik Terrane are predominantly trondhjemitic and granitic orthogneisses and amphibolite dominated supracrustal units. The IGB is composed of metamorphosed mafic to ultramafic volcanics with minor gabbros, diorites and metasediments. Pegmatites are also common. The IGB is divided into a lower and an upper amphibolite unit separated by the magnetite-rich Magnetic Marker horizon. It is associated with metasediments (schists, felsic gneisses, tourmaline rocks) and calc-silicate rocks from which strata-bound scheelite mineralisation was reported before. Two different types of calc-silicate rocks are distinguished in the study area. Type I is the result of pillow basalt alteration with preserved pre-metamorphic zoning. It is predominantly composed of epidote, clinopyroxene, plagioclase and quartz as well as calcite, scapolite, ilmenite and titanite, the assemblages now reflecting reequilibration under upper amphibolite facies of regional metamorphism. Type II calc-silicate rocks postdate Type I and formed synkinematically between the two main deformation events (D2, D3) in the IGB and during low-P regional metamorphism. Type II rocks are richer in calcic garnet that coexists with clinopyroxene, epidote, quartz, calcite, titanite and plagioclaseand they have generally higher tungsten contents. Whereas Type I rocks do not show systematic chemical changes during alteration Type II calc-silicate alteration is characterised by enrichment of Ca, depletion of LIL elements and considerable variation in and mobility of HFS elements and REE. Comparison of altered rocks with their unaltered protoliths indicates that there is for example an enrichment of Ca, Nb, Ta, Be and U together with W.

Metapelites containing garnet, plagioclase, biotite, muscovite, staurolite, chlorite, amphibole and ilmenite were used for geothermobarometrical investigations and yielded average

temperatures and pressures ranging between 550 and 650°C and 5.0 to 5.7 kbar, respectively for peak of regional metamorphism. Tungsten mineralisation is clearly stratabound because it is hosted by calc-silicate rocks of Type II that can be traced for several kilometres along strike. However, field relationships and the results of the chemical investigations do not support a syngenetic-exhalative origin of tungsten mineralisation.

2. Zusammenfassung

Im Zuge des Projekts „Greenstone belts in the central Gothabsfjord region, southern West Greenland“ des Geologischen Dienstes von Dänemark und Grönland (GEUS) konnte Ao. Prof. Dr. Johann G. Raith in den Jahren 2004 und 2005 Geländearbeiten im Ivisaartoq Grüngesteinsgürtel (Ivisaartoq Greenstone Belt, IGB) durchführen. Das Hauptaugenmerk der Geländearbeiten und Probennahme lag dabei auf den dort vorkommenden schichtgebundenen Wolframmineralisationen. Die von ihm genommen Proben und Geländebeobachtungen stellen die Basis für die vorliegende Diplomarbeit dar. Die vorliegende Diplomarbeit hat hauptsächlich die chemische Charakterisierung der beiden vorkommenden Typen von Kalksilikatgesteinen und deren Petrographie, aber auch die Berechnung der Druck-Temperatur-Bedingungen der Metamorphose zum Thema.

Der IGB ist ~3075 Ma alt und ist einer von mehreren mesoarchaischen Grüngesteinsgürteln in SW-Grönland. Er wird zum Kapisilik Terrane gestellt, das zwischen dem Isukasia und dem Færinghaven Terrane liegt, die beide hauptsächlich aus früharchaischen Gesteinen aufgebaut sind. Das Kapisilik Terrane besteht im wesentlichen aus trondhjemitischen und granitischen Orthogneisen und suprakrustalen Amphibolit-dominierten Gesteinsabfolgen. Der IGB selbst beinhaltet sowohl metamorphe mafische und ultramafische Vulkanite als auch untergeordnet Gabbros, Diorite und Metasedimente. Auch Pegmatite sind recht weit verbreitet. Man unterteilt den IGB in eine Untere und eine Obere Amphibolit Einheit, die durch den Magnetic Marker Horizont, einen bis zu mehreren Zehnermetern mächtigen Horizont stark deformierter und metamorph-metasomatisch umgewandelter Ultramafite, getrennt werden. Dieser wird von geringmächtigen Metasedimenten (Granat-Biotot-Sillimanit-Schiefer, felsische Gneise, Turmalingesteine) und Kalksilikatgesteinen, aus denen schichtgebundene Wolframmineralisationen bekannt sind und von bis zu mehreren hunderten Metern mächtigen Pillow Basalten mit zwischengeschalteten Ultramafitkörpern überlagert.

Man unterscheidet zwei Typen von Kalksilikatgesteinen: Typ I ist das Ergebnis einer Alteration der Pillow Basalte, wobei bevorzugt die Kernbereiche von Pillows alteriert wurden. Dieser Typ besteht hauptsächlich aus Epidot, Klinopyroxen, Plagioklas und Quarz sowie aus Kalzit, Skapolith, Ilmenit und Titanit. Diese Alteration erfolgte im Zuge einer Ozeanbodenmetamorphose und wurde von der amphibolitfaziellen Regionalmetamorphose überprägt, wobei in Zonen geringerer Deformation die prämetamorphe Zonierung der Pillow-

Strukturen oft erhalten blieb. Typ II Kalksilikatgesteine sind jünger als Typ I. Sie haben sich synkinematisch zwischen den beiden Hauptdeformationsereignissen (D2, D3) und der sie begleitenden Niedrig-Druck Regionalmetamorphose gebildet. Typ II Gesteine sind reicher an kalzischem Granat, der zusammen mit Klinopyroxen, Epidot, Quarz, Plagioklas, Calcit, Titanit und Scheelit vorkommt. Höhere Wolframgehalte sind nur charakteristisch für Typ II. Typ I Kalksilikatgesteine zeigen keine systematischen chemischen Veränderungen während der Alteration, wohingegen Typ II Gesteine klar durch die starke Anreicherung von Ca, die signifikante Abreicherung von LIL Elementen und die beachtliche Mobilität von HFS Elementen und REE gekennzeichnet sind. Vergleiche von alterierten Kalksilikatgesteinen mit nicht alterierten Nebengesteinen lassen darauf schließen, dass im Zuge der Alteration Ca, Nb, Ta, U, Be gemeinsam mit W angereichert wurden. Die Typ II Kalksilikatgesteine belegen daher eine chemische Affinität zu granitischen / pegmatitischen Fluiden.

Metapelitische Gesteine führen Granat, Sillimanit, Biotit, Muskowit, Chlorit, Plagioklas, Quarz und Ilmenit. Staurolith kommt nur als Relikt vor. In einer untersuchten Probe koexistieren Amphibole mit Granat, Plagioklas etc. Für drei Proben wurden die durchschnittlichen Drucke und Temperaturen der regionalen Metamorphose mit Thermocalc berechnet. Die Temperaturen liegen zwischen 550 und 650°C die Drucke zwischen 5.0 und 5.7 kbar. Für die Peak-Metamorphose im IGB lassen sich demnach Bedingungen der oberen Amphibolitfazies ableiten

Die Wolframmineralisation im IGB ist hauptsächlich an Kalksilikatgesteine des Typs II gebunden, wobei der Haupthorizont im Hangenden des Magnetic Marker über mehrere Kilometer entlang des Streichens verfolgt werden kann. Die Scheelitvererzung kann daher als schichtgebunden bezeichnet werden. Die Feldbeziehungen belegen aber, dass die Typ II Kalksilikatgesteine nach einer ersten penetrativen Deformation während der regionalen Metamorphose gebildet wurden. Auch die Ergebnisse der chemischen Untersuchungen deuten eher eine geochemische Affinität zu Wolframlagerstätten, die mit sauren plutonischen Gesteinen assoziiert sind, an. Das in der Vergangenheit diskutierte syngenetisch-exhalative Genesemodell der Wolframvererzung wird durch die Ergebnisse dieser Studie daher nicht unterstützt.

3. Introduction

In summer 2004 the Geological Society of Denmark and Greenland (GEUS) started the project "Greenstone belts in the central Gothabsfjord region, southern West Greenland" with emphasis on providing geological information about the greenstone belts and their mineral occurrences in southern West Greenland and triggering mineral exploration in SW Greenland. In the course of this project Ao.Univ.Prof. Dr. Johann G. Raith had the possibility to do field work in the Ivisaartoq area in the summers 2004 and 2005 focussing on stratabound scheelite mineralisation there. In early 2006 I was offered the chance to work on some aspects of this project within an MSc project at the University of Leoben.

The studied samples are from the ~3075 Ma Ivisaartoq Greenstone Belt, one of the best - preserved greenstone belts of Mesoarchaean age in southern West Greenland. It lies about 150 km SW of the well studied Paleoarchaean Isua Greenstone Belt, where the oldest rock record for geological processes on the Earth's surface are preserved in supracrustal rocks of ~3.7 Ga age.

The focus of this thesis lies on studying the two main types of calc-silicate rocks occurring in the IGB. On one hand there are altered zoned pillow basalts, which show a calc-silicate alteration of the pillow cores (Type I), on the other hand there are vein type to massive layered calc-silicate rocks (Type II), which are noticeably enriched in tungsten containing scheelite as the main tungsten carrier.

The aims of this study are:

- To document the petrography of Type I versus Type II calc-silicate rocks, their unaltered host rocks as well as the transitional rocks formed during alteration.
- To obtain chemical data of major and trace elements including REE for these rocks.
- To support the differences of the two types of calc-silicate alteration as established from field relationships by petrographical and chemical data.
- To work out the chemical fingerprints for the two types of calc-silicate alteration.
- To establish the P-T conditions of peak metamorphism by applying quantitative geothermobarometry.

A major aim of this project was to compare the chemistry of the two types of calc-silicate alteration to see if they are genetically related and if tungsten has also been concentrated during pre-metamorphic Type I calc-silicate alteration. For this purpose several methods were used. Information about field relationships (outcrop documentation, structural relationships) was provided by J.G. Raith. My own work started with the petrographical investigation of altered and unaltered rocks. Chemical data were used to get an overview over the mobility of certain elements during the different alteration events. Altered calc-silicate rocks were compared to unaltered host rocks. For Type I calc-silicate alteration this was done by comparing altered pillow cores with unaltered outer pillow zones and rims. For Type II calc-silicate alteration the transition from calc-silicate altered to unaltered host rocks was sampled (outcrop to hand specimen scale). Chemical data have been acquired using inductively coupled plasma – mass spectrometry at the University of Leoben and X-ray fluorescence at the University of Graz.

Rare metasediments containing garnet + sillimanite + biotite + muscovite + quartz ± plagioclase ± amphiboles were also investigated to estimate the pressure and temperature conditions of the main metamorphic event in the Ivisaartoq Greenstone Belt. Data about the chemical composition of minerals were obtained by electron microprobe (EMP) analysis at the University of Leoben. Mineral chemical data were used to calculate average P-T conditions using Thermocalc and the results confirm that the IGB was metamorphosed under conditions of the upper amphibolite facies.

4. Regional geology

4.1. Geological overview and geological history

This study deals with the Ivisaartoq Greenstone Belt (IGB) located in the Nuuk region in southern West Greenland. In the Nuuk region some of the oldest rocks on Earth, they are exposed in the Isua Greenstone Belt and on Akilia Island, are known and dated at 3700 Ma – 3800 Ma and ≥ 3850 Ma, respectively (Nutman *et al.*, 2004). In addition to these Palaeoarchaean greenstone belts there are several Meso- to Neoarchaean greenstone belts known in the Nuuk region, including the studied Ivisaartoq Greenstone Belt whose age is constrained between about 2.96 and 3.07 Ga (see chapter 4.2).

Much research has been done over the last 35 years and several models for the Archaean evolution of the Nuuk region were postulated. McGregor (1973, 1979) was the first to recognise that the predominant gneissose rocks in the Nuuk region are orthogneisses of a mostly granodioritic-tonalitic composition. This was opposing the view that these gneisses derived from quartzo – feldspatic metasediments.

Based on the field studies by McGregor (1973, 1979) and on isotope studies by Black *et al.* (1971) and Moorbath *et al.* (1972) it was concluded that there must have been several stages of juvenile crust formation of different age in the Nuuk region. Two main types of orthogneisss were distinguished; i.e. the Palaeoarchaean Amitsoq gneisses and the younger Mesoarchaean Nuuk gneisses. McGregor (1973) had already differentiated the two types of gneisses by recognising that a suite of mafic dykes, the Ameralik dykes, intruded the Amitsoq gneisses but not the younger Nuuk gneisses. Today the Palaeoarchaean Amitsoq gneiss is the dominant member of the Itsaq Gneiss Complex (Nutman *et al.*, 1996).

According to early concepts this two main stages of juvenile crust formation were followed by a single event of granulite – amphibolite facies metamorphism (Wells, 1976, 1979) of roughly Meso- to Neoarchaean age. Regional metamorphism was postdated by emplacement of post-orogenic crustal granites; e.g. the Qorqut granite, 2550 Ma ± (Brown *et al.*, 1981).

With the increasing number of ages (e.g. Baadsgaard & McGregor, 1981) it was soon no longer possible to interpret the tectono-metamorphic evolution of the Nuuk region with a

simple two-phase model of crustal melting. Friend *et al*. (1987, 1988) therefore introduced the terrane concept to the Nuuk region. Initially four terranes were distinguished in the Nuuk region, i.e. the Færinghaven, Tre Brødre, Tasiusarsuaq and Akia terranes. In later studies the Tre Brødre and Færinghaven Terranes were also referred to as composite Akulleq terrane (Friend *et al*., 1996). More recently this strict separation into four terranes was abandoned by Friend & Nutman (2005b) who introduced two new terranes in the NE Nuuk region, the Palaeoarchaen Isukasia terrane and the 3075 - 2960 Ma Kapisilik terrane. These two terranes were juxtaposed and metamorphosed together at ~2950 Ma.

Each of these terranes represents a stand-alone evolution of juvenile, tonalitic crust and preserves early metamorphic structures and an age inventory that is unique for each single terrane; e.g., the Gea 2900 – 2800 Ma granulitic facies event has only been reported from the Tasiusarsuaq terrane (Friend *et al*., 1996). Between c. 2950 Ma and 2700 Ma these terranes were tectonically assembled during several mid- to Neoarchaean terrane assembly events, with superimposed "orogenies" (Friend & Nutman, 2005a).

4.1.1. Itsaq Gneiss Complex

The Itsaq Gneiss Complex is mainly composed of grey, banded orthogneisses with lenses and inclusions of mafic and ultramafic material. Sediments like quartzite and banded iron formations occur as minor lithologies (Friend & Nutman, 2005a).

The chronology of the Itsaq Gneiss complex starts with processes of crustal accretion dated between 3850 – 3690 Ma and is followed by a 3670 – 3500 Ma event (Friend & Nutman, 2005b). These events include high-grade metamorphism and migmatisation, as well as intrusion of gabbros and granites with a deep crustal origin. Combining this with 3650 – 3600 Ma metasediments of complex composition lead to the interpretation of an orogeny superimposed on the original tonalite – trondhejmite – granodiorite (TTG) series (Friend & Nutman, 2005a).

Transformation of the originally discordant granitoids into banded gneisses took place during several Archaean deformation events, combined with amphibolite to granulite facies metamorphism. These processes happened between 3850 and 2550 Ma.

The ~3.5 Ga Ameralik dykes intruded the Palaeoarchaean Itsaq Gneiss complex. Their appearance is in form of discordant, boudinaged, tabular amphibolite bodies (McGregor, 1979). According to Chadwick (1990) there are at least seven generations of Ameralik dykes aged between 3500 Ma and 3450 Ma (Nutman *et al*., 2004). Following the interpretations of White *et al*. (2000a), Nielsen *et al*. (2002) and Nutman *et al*. (2004) they can be related to a rifting process at ~3500 Ma.

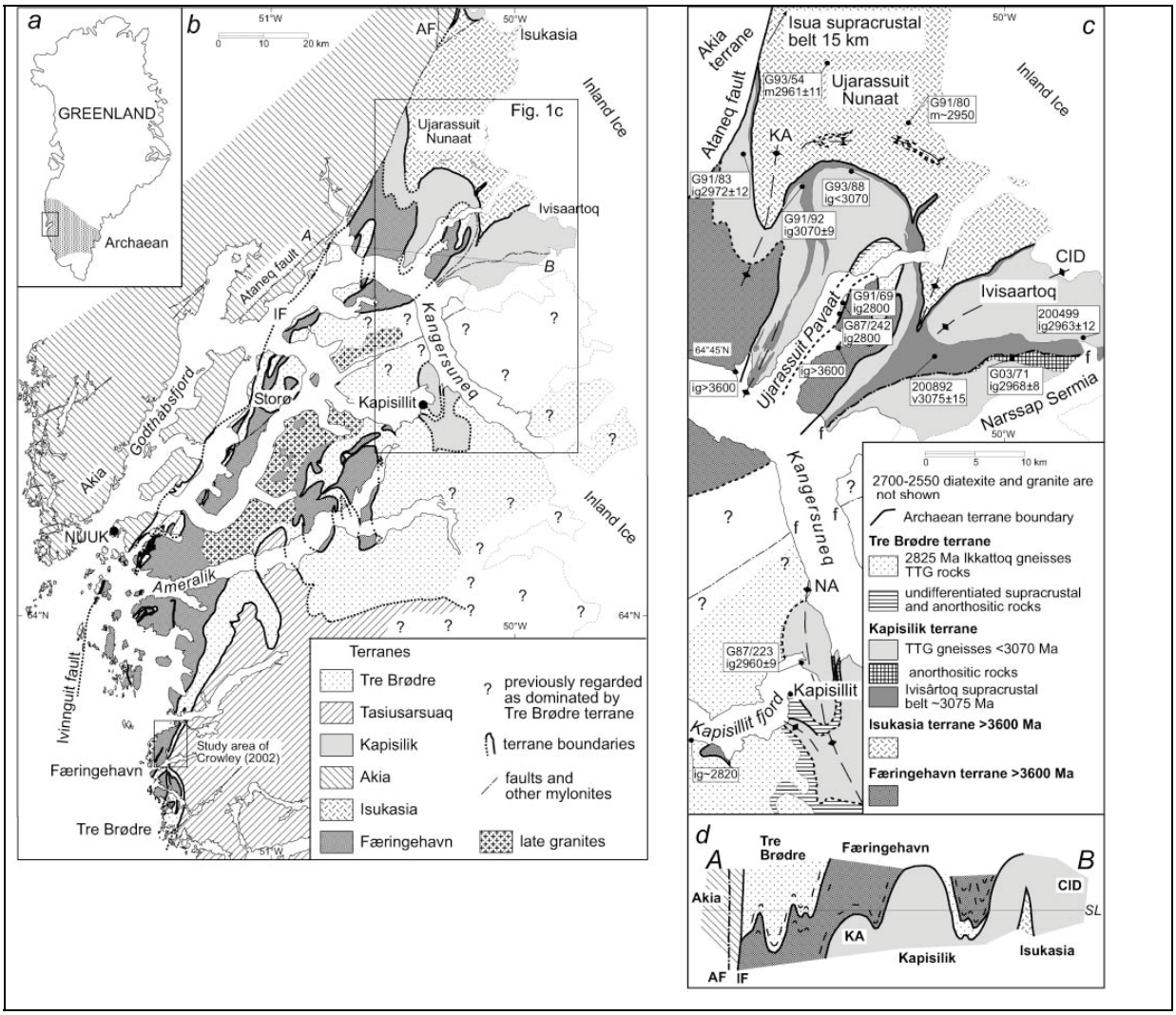

Figure 4.1.1: Sketch map of the terranes in the Nuuk region and their position. (**a**) Position of the Nuuk region in West Greenland. (**b**) The different terranes of the Nuuk region. (**c**) Map of the inner Gothabsfjord for better recognition of the Kapisilik and Isukasia terranes as well as the Ivisaartoq Greenstone Belt (**d**) Cross section along line AB; from Friend & Nutman (2005b).

4.1.2. Terranes in the NE Nuuk region

Isukasia and Færinghaven terrane

U-Pb dating of zircon provides evidence that rocks in the Isukasia terrane formed between ~3.65 to 3.8 Ga; these include 3.8–3.7 Ga tonalities, 3.65 Ga granites and ~3.8 - 3.7 Ga supracrustal, ultramafic and gabbroic rocks (Friend & Nutman 2005a and references therein).

The ~3.5 Ga discordant Ameralik dykes cut lithologies in the northern part of the Isukasia terrane. Its southern part differs from the northern one because of more intense deformation and the formation of metamorphic zircons dated at 2960 Ma and 2700 Ma (Friend & Nutman, 2005a)

The Færinghaven terrane is exposed in the southern Nuuk region. It is mainly composed of rocks dated between 3850 Ma and 3600 Ma, which underwent granulite facies metamorphism in the Palaeoarchaean (~3600 Ma) and were also affected by various metamorphic events in the Neoarchaean (from 2800 Ma onwards). The 3500 Ma Ameralik dykes can also be found in the Færinghaven terrane.

Considering the facts that Ameralik dykes are found in both terranes but that the various metamorphic events are of different age in each terrrane Friend & Nutman (2005b) interpret the two terranes as parts of an older Palaeoarchaean complex that drifted apart at ~3500 Ma. This extensional event induced the emplacement of Ameralik dykes. In the Neoarchaean these two older terranes were juxtaposed to the younger Kapisilik and Tre Brødre terranes. According to Friend & Nutman (2005b) this Palaeoarchaean rifting has analogues in northern Greenland (Aasivik terrane, Rosing *et al.*, 2001; Qarlit Tasersuat, Nutman *et al.*, 2004a).

Kapisilik terrane

The Kapisilik terrane is composed of 3075 - 2960 Ma old rocks east of the Ivinnguit fault (Figure 4.1.1; Friend & Nutman, 2005b). The Kapisilik terrane lies between the Isukasia terrane in the north and the Færinghaven terrane in the south. The Kapisilik terrane contains

mainly trondhjemitic and granitic orthogneisses and amphibolite dominated supracrustal units of which the Ivisaartoq Greenstone Belt is the largest one.

The so-called Central Ivisaartoq dome, composed of granitic rocks and migmatites (Chadwick, 1990), is enclosed by the greenstone belt. In the marginal parts the Ivisaartoq Greenstone Belt (Hall & Friend, 1983) is intruded by granitic gneisses dated at 2961 ± 11 Ma (Friend & Nutman, 2005a). Hence this age must be considered as the minimum age of the belt.

In the north the Ivisaartoq Greenstone Belt is bound by a 2 m thick mylonitic zone, which separates the belt from anorthosites and leucogabbros that are dated at 2963 ± 8 Ma (Friend & Nutman, 2005a). Thus, these authors concluded that the mylonitic structures deforming the Kapisilik terrane formed after 2960 Ma.

4.1.3. Tectonic framework

Although the terranes in the Nuuk region are relatively small and only deeper crustal levels are exposed Friend & Nutman (2005a) see analogies to modern orogenies. According to their interpretation the initial TTG–series that can be found in all terranes are indications of melting processes in subduction zone settings and during early crustal accretion due to continental collision.

After the rifting of the first Palaeoarchaean continent and the simultaneous intrusion of the Mesoarchaean Ameralik dykes the following reconsolidation of terranes happened in at least two different events (Friend & Nutman 2005a). The first was the juxtaposition of the Kapisilik terrane over the Isukasia terrane at ~2950 Ma. Later, at about 2800 Ma, this block was amalgamated with the Færinghaven and Tre Brødre terrane. This implies that the Isukasia terrane is the unit lying in the deepest tectonic position and that it is successively overlain by the Kapisilik, Tre Brødre and Færinghaven terranes (Figure 4.1.1 (d)).

4.2. The lithostratigraphy of the Ivisaartoq Greenstone Belt (IGB)

As stated above the IGB is the largest continuous occurrence of supracrustal rocks in the Kapsilik Terrane. Its geology has been studied in detail by Chadwick (1985, 1986, 1990). A recent paper dealing with its geochemical characteristics has been published by Polat *et al.* (2007).

The age of this belt is bracketed by U-Pb zircon ages between ~2960 and 3075 Ma. The maximum age of the belt is deduced from the 3075 ± 15 Ma age of detrital zircons from quartz-rich rocks (Friend & Nutman, 2005a) The minimum age is deduced from weakly deformed granite dykes of the Central Ivisaartoq dome that intrude the greenstones at 2961 ± 11 Ma (Friend & Nutman, 2005a).

The IGB is mainly composed of metamorphosed, mafic to ultramafic volcanic rocks, gabbros and diorites (Chadwick, 1985, 1986, 1990). Remnants of pillow structures give evidence that the mafic and ulltramafic units originated from ultramafic to tholeiitic flows (e.g. Hall et al. 1987 in Friend & Nutman, 2005a). Metasediments are, as shown in Figure 4.2.1, only sporadically found.

In his publications in 1986 and 1990 Chadwick divided the Ivisaartoq Greenstone Belt in a lower and an upper amphibolite unit and distinguished several ultramafic layers within the upper unit, which he used as marker horizons for mapping. The lower and upper unit are separated by an up to 50 m thick and 8 km long horizon called the Magnetic Marker. This horizon includes various magnetite-rich ultramafic schists, which are associated with metasediments and calc-silicate rocks. Scheelite was first reported from these calc-silicate rocks by Appel (1988b). The degree of deformation of the pillow basalts is increasing towards the contact of the two amphibolite units. Thus, this contact is believed to be tectonic (Polat *et al.*, 2007).

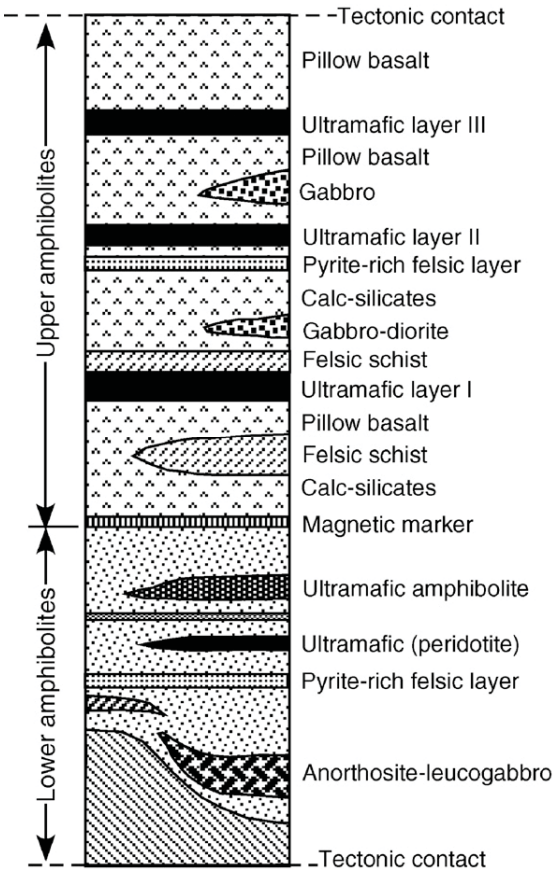

Figure4.2.1: Simplified stratigraphic sketch of the Ivisaartoq Greenstone Belt. After Chadwick (1990), taken from Polat *et al*. (2007)

Metabasites in the lower amphiolite unit are more intensely deformed and are more homogeneous than in the upper unit. For example foliation in the lower unit is better defined than in the upper one. An up to 50 m thick and up to 5 km long layer of pyrite rich, felsic schist is intercalated in the lower amphibolite unit. Furthermore this unit is characterised by intercalations of a peridotitic as well as an ultramafic amphibolite layers (Figure 4.2.1).

In its stratigraphically deeper parts the Magnetic Marker is dominated by magnetite-rich ultramafic schists composed of magnetite, olivine, spinel, carbonates and chlorite. There are also disseminated sulfides, especially pyrite and chalcopyrite, reported from this lower part of the Magnetic Marker (Chadwick, 1990). Massive layers of greenschists overlie this lower part of the Magnetic Marker. Veins and layered bodies of calc-silicate rocks with diopside, garnet and hornblende etc. and of variable thickness (up to several meters) are mainly found in the upper part of the Magnetic Marker but can also be found in the lower parts of the upper amphibolite series. Scheelite mineralisation is mostly associated with these calc-silicate rocks (Appel, 1988a, 1988b, 1994).

According to Chadwick (1990) deformed pillow basalts, volcanic breccia, foliated amphibolite, actinolite schist, ultramafic cumulate, serpentinite and metasedimentary rocks are the main constituents of the upper amphibolite unit. As shown in Figure 4.2.1 there are three layers of serpentinised ultramafic rocks (ultramafic layers I to III) distributed within the upper amphibolite unit. They occur in the form of boudinaged bodies with a maximum length of 600 m and a width of up to 200 m. These layers are separated by pillow basalts and it is to be noted that pegmatites are commonly intercalated in the whole sequence (Chadwick, 1990).

Chadwick (1990) reported minor tectonically disrupted siliciclastic metasedimentary rocks with sharp contacts to the volcanic series in the upper amphibolite series. Gabbros and minor diorites form up to several meter thick sills and dykes in the pillow basalts. The whole sequence was affected by two main stages of metasomatic calc-silicate alteration (Polat *et al.*, 2007; Raith, 2004). Occasionally the pillow basalts of the upper amphibolite unit preserve a well-defined mineralogical and chemical zonation (Polat *et al.*, 2007).

4.3. Field observations

4.3.1. General remarks

The geology of the area of interest, based on the geological map 1: 100.000 (Chadwick & Coe, 1988) is shown in Figure 4.3.1. Sample locations are indicated with numbers (e.g. IV20, C77). These have been added to the map using the geographic coordinates of sampling sites collected during field work in the years 2004 and 2005 by J. G. Raith (see Appendix A).

As can be seen many samples were taken along the Magnetic Marker horizon and the lower part of the upper amphibolite unit. Only few sample locations (e.g. C63, C64, C65) lie within the lower amphibolite unit. This bias in sampling is caused by the fact that the main target during field work was the scheelite mineralisation, which is mostly found along this tectono-stratigraphic horizon.

As it was not possible to do field work myself, the following brief description of key outcrops and field observations and their photographic documentation are based on field work by the supervisor of this thesis, J.G. Raith. Hence, the purpose of this chapter is to set the scene for the petrography and geochemistry work performed and to provide the basic information necessary for interpreting these data.

4.3.2. Pillow basalt structures and Type I calc-silicate alteration

In some low-strain parts of the IGB pillow structures in metabasites are extremely well preserved (Chadwick, 1990; Appel, 1994, 1997; Polat *et al.* 2007). Cores and rims can be distinguished in individual pillow structures. The outer pillow cores contain lighter mm- to cm-sized ellipsoidal ocelli that are embedded in a finer grained darker matrix. In the inner pillow core matrix and ocelli are commonly replaced by metasomatic calc-silicate assemblages (diopside + epidote + quartz etc., see chapter 6). Sometimes, empty or quartz-filled drainage cavities are also developed in the inner cores. The outer pillow cores are reported to be devoid of calc-silicate alteration. The dark, nearly black pillow rims are of an amphibole-rich composition. It is thought that the outer pillow cores and the pillow rims preserve initial basaltic compositions (Polat *et al.*, 2007).

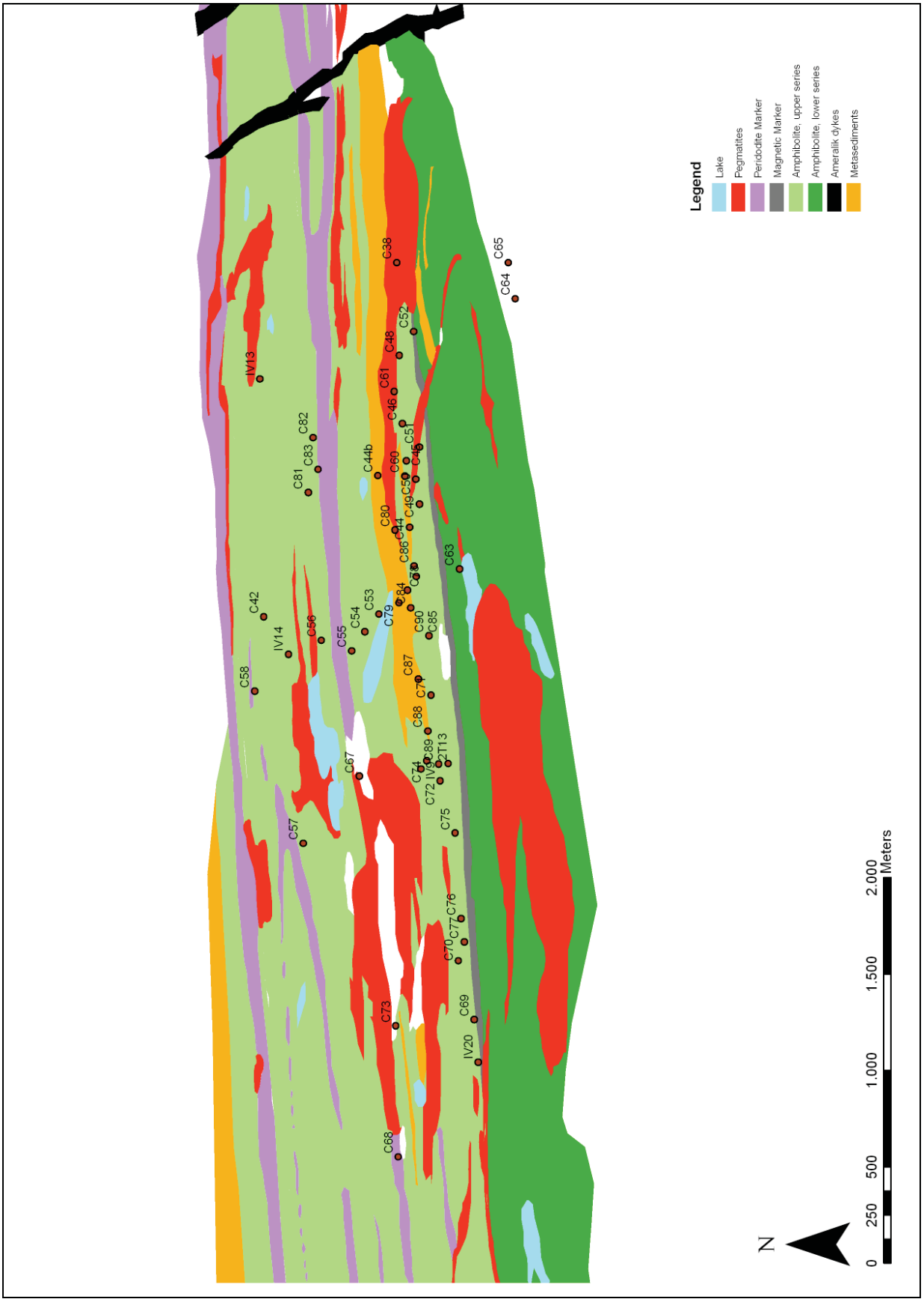

Figure 4.3.1: Geological map of the investigated area. Numbers indicate the localities of taken samples. Geology simplified after Chadwick (1988).

This type of early calc-silicate alteration of pillow cores (Type I according to Raith, 2004) shows similarities to epidosites and has been related to hydrothermal ocean-floor metamorphism (Polat *et al.*, 2007). In addition to this early stage calc-silicate alteration there is silicification observed in some outcrops of pillow basalts; this stage of alteration is also regarded as pre-regional metamorphic (J.G. Raith, personal communication).

In strongly deformed outcrops pillows are stretched and flattened. Strong deformation finally results in development of banded amphibolites in high strain areas concealing the original pillow structures of these rocks.

Figure 4.3.2 shows an extremely well-preserved spectacular pillow basalt (outcrop C42). One can very clearly distinguish an inner calc-silicate-rich core, which is rich in epidote surrounded by an ocelli-rich grey outer core zone and a thinner dark black rim. In some pillows from the same outcrop the inner cores contain quartz-rich cavities and veins (Figure 4.3.3). Outcrop C57 lying within the upper amphibolite unit south of the second peridotite marker also shows well-preserved zoned pillow basalts with an epidote-rich core containing quartz veins. These veins show some tectonically controlled orientation (Figure 4.3.3) and therefore can not be drainage cavities as discussed by Polat *et al*. (2007).

Occasionally, pillow basalts were also affected by silicification. In the outcrops this type of alteration is to be seen as “bleaching” of pillow structures. As shown in outcrop C67 (Figure 4.3.4) the pillow basalts become light coloured, individual pillows developing white/grey pillow cores and dark rims. In outcrop C67 a ~10 cm wide deformed pegmatite vein crosscuts the silicified pillows indicating that this alteration predated pegmatite emplacement.

Outcrop IV35 lies at the contact of metasedimentary gneisses, metagabbro, altered pillow basalts and pegmatite. Figure 4.3.5 shows deformed, elongated meter-sized pillows with epidote-rich cores. Elongation of calc-silicate-rich cores is well visible.

Figure 4.3.2: Outcrop C42; altered inner core – ocelli-rich outer core zone – dark rims can be distinguished in individual up to 1m sized pillows.

Figure 4.3.3: Outcrop C42; zoned pillow structure. Altered inner pillow core with quartz filled cavities, ocelli rich outer core, and black rim.

Figure 4.3.4: Outcrop C57; altered pillow core with quartz veins in inner core (partly weathered out), grey ocelli-rich outer core zone and black rim plus silicified (white) interstitial material.

Figure 4.3.5: Outcrop C67; silicified pillows crosscut by folded pegmatite.

Figure 4.3.6: Outcrop IV35; deformed pillow basalts with elongated epidote-rich cores in contact with 1m metagabbro to the right.

4.3.2. Type II calc-silicate alteration

Type II calc-silicate rocks are distinguished form earlier Type I calc-silicate alteration based on the following criteria: (a) field relationships indicate that they postdate early stage-alterations. (b) Their mineralogical composition is different; the calc-silicate rocks are rather garnet-rich and garnet normally coexists with clinopyroxene. (c) They are characterised by a generally higher content in tungsten and show a distinct geochemical trace element pattern (see chapter 9). Actually these are the immediate host rocks of scheelite mineralisation.

In outcrop C55 (Figure 4.3.7) a garnet-rich calc-silicate layer in pillow basalts can be seen. The layer is parallel to the dominant foliation of the host rocks (foliated pillow basalts) and shows internal zonation. As shown in Figure 4.3.7 the central part is garnet-rich and contains lots of extensional quartz veins whereas the contact to the metabasalts is made up of cm-thick fine-grained green alteration halos. The discordant subvertical quartz-garnet veins crosscut the calc-silicate rocks. These veins can contain up to 10 cm big garnet crystals (not shown on photo). These quartz-veins are interpreted as extension veins developed during the second stage of regional deformation (late D2 in Raith, 2004) in the more competent calc-silicate layers.

Similar to outcrop C55 also in C73 a zoned garnet-rich calc-silicate layer can be seen (Figure 4.3.8). As shown in the Figure it is composed of a lens-shaped garnet-quartz vein crosscutting pillow basalts. The contact to these adjacent metabasalts is composed of fine-grained green garnet free alteration halos which are comparable to those from outcrop C55

In the same outcrop a ~1 m thick mafic dyke is exposed (Figure 4.3.9). This dyke has a sharp contact to the surrounding bleached pillow basalts. On the left side of this dyke lies a ~10 cm wide calc-silicate vein. It shows similar zonation as the above described calc-silicate veins with coarse-grained garnet in the center and a fine-grained green alteration zone at the outer rim. Additionally a discordant quartz vein crosscuts the mafic dyke.

Calc-silicates of type II can also occur as boudinaged bodies / layers (Figure 4.3.10, outcrop IV10). The massive to banded calc-silicate rocks as such show the same features as the calc-silicate veins described earlier. However, the green alteration halo is not as well defined.

Individual calc-silicate bodies are intercalated with thin amphibolitic layers. Meter-sized unaltered metabasites surround these boudins.

Outcrop IV20 lies at the contact between the Magnetic Marker and adjacent metasediments (Figure 4.3.1). Locally developed green calc-silicates are replacing the metamorphic layering and foliation. As shown in Figures 4.3.11 and 4.3.12 a diffuse front of greenish rocks is replacing the F1 fold, which accordingly to Raith (2004) is interpreted as an early S1 fabric, in a felsic gneiss.

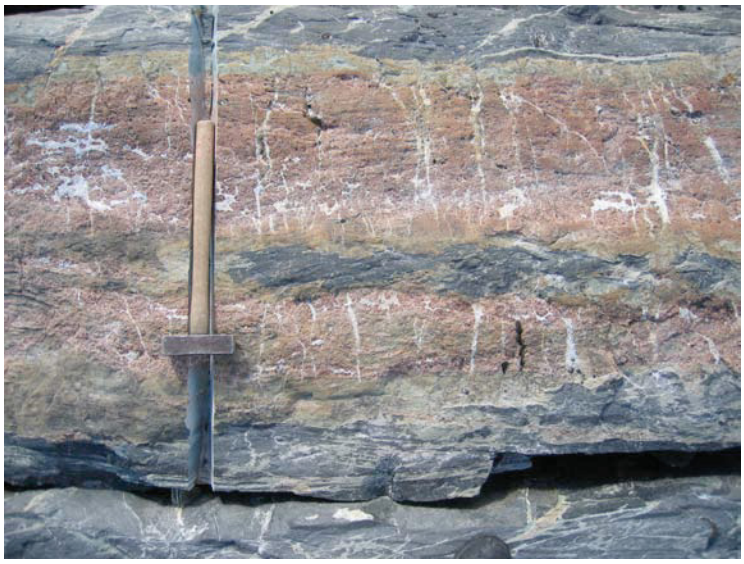

Figure 4.3.7: Outcrop C55; garnet-rich calc-silicate rock with quartz-filled extension veins in pillow basalts.

Figure 4.3.8: Outcrop C73; zoned calc-silicate vein in pillow basalt.

Figure 4.3.9: Outcrop C73; mafic dyke in altered pillow basalts; calc-silicate vein at left side; crosscutting quartz vein in the dyke.

Figure 4.3.10: Outcrop IV10; boudinaged calc-silicate layers in metabasite.

Figure 4.3.11: Outcrop IV20; Type II calc-silicates replacing S1 foliation in interlayered amphibolite-gneiss rock

Figure 4.3.12: Outcrop IV20; Type II calc-silicates replacing F1 fold in felsic gneiss.

4.3.3. Scheelite mineralisation

Type II calc-silicates are the host rocks of the scheelite mineralisation and have also been described in chapter 4.3.2. The following chapter is dedicated to showing field relationships in scheelite-bearing outcrops.

The central part of outcrop IV5 is composed of green to pale red calc-silicate rock. It contains up to 1 cm scheelite porphyroblasts showing pale yellow fluorescence in short UV range. This inner zone is surrounded by an up to 10 – 20 cm thick zone of sulphide-bearing coarse-grained hornblende-plagioclase-quartz rock grading into well foliated biotite gneiss and biotite-sillimanite schist. (Figure 4.3.14; see also Stückler, 2007). As one can see in Figure 4.3.13 the mm – cm foliation wraps around the calc-silicate body forming an open fold

Figure 4.3.13: Outcrop IV5; banded biotite-gneiss wrapping around calc-silicate rocks in an open fold.

Figure 4.3.14: Outcrop IV5; contact zone of biotite-gneiss (left) and coarse hornblende-plagioclase-quartz rock (right).

4.3.4. Metapelitic rocks

As pointed out in chapter 4 the metasedimentary rocks lie on top of the calc-silicate horizon and the Magnetic Marker. They are for instance well exposed in outcrop IV7, which can be traced over 30 – 40 m along strike. The metasediments are well foliated and layered. Some layers contain mm-sized elongated white porphyroblasts that are aligned in the main foliation. In thin sections these have been identified as sillimanite-rich aggregates showing elongation. In some of these layers garnet has been observed. Garnet and sillimanite-richer layers alternate with foliated biotite gneiss.

In some places orthogneisses that crosscut the biotite gneiss were observed. Figure 4.3.15 also shows a deformed quartz vein, which is one of several sheared veins that can reach a thickness of up to 40 cm.

The metasedimentary units of outcrop C86 (Figure 4.3.16) are composed of sulfide-bearing layers causing the rusty weathering colours of this outcrop. From the left to the right four different lithologies can be distinguished: 1) garnet-bearing metapelite. 2) garnet-bearing muscovite-biotite schist with rusty layers. 3) felsic to quartzitic gneiss 4) cm up to dm boudins of calc-silicate layers rich in clinopyroxene.

Figure 4.3.15: Outcrop IV7; biotite gneiss with "porphyroblast-rich" layers containing sillimanite (top part of the photo), sheared quartz vein in biotite gneiss (bottom part of the foto).

Figure 4.3.16: Outcrop C86; garnet-bearing metapelites showing rusty weathering colours.

4.3.5. Magnetic Marker

As a major stratigraphic horizon in the IGB the Magnetic Marker separates the lower and the upper amphiblite units (see chapter 4). Outcrop IV19 is an example of the well foliated ultramafic schists which are exposed in the footwall of the metasediments and the scheelite-bearing calc-silicate rocks. These rocks were not the topic of this MsC thesis and are therefore not dealt with in more detail.

Figure 4.3.17: Outcrop IV19; typical outcrop of the Magnetic Marker horizon.

5. Methods

5.1. Microscopy

Microscopical investigation was done with an Olympus BX40F4 polarising microscope at the Chair of Mineralogy and Petrology at the Department of Applied Geosciences, University of Leoben. Digital photos were taken using a UEye UI-1460-C digital camera adapdet to a Zeiss Axiolat polarising microscope.

5.2. Inductively Coupled Plasma – Mass Spectrometry (ICP-MS)

5.2.1. Assembly of ICP-MS

Using ICP-MS means combining the two methods of mass spectrometry (MS) and inductively coupled plasma ionisation (ICP). In geosciences this form of analysis is commonly used to gather multi-trace element data. The principal components of an ICP-MS instrument are shown in Figure 5.1

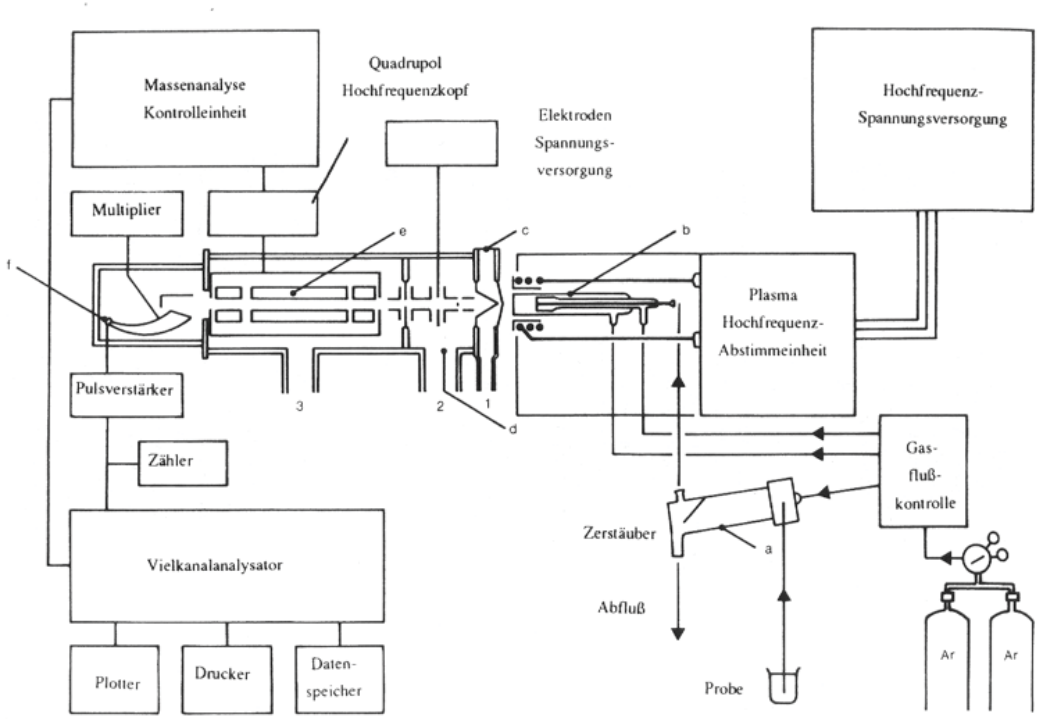

Figure 5.1: Principal construction of an ICP-MS instrument(Jochum et al. 2000).

The generation of inductively coupled plasma is maintained by a plasma torch by transmitting energy via an induction coil to the gas. A typical plasma flare as used in ICP-MS can be seen in Figure 5.2. It is made up of three concentrical quartz pipes whose upper parts are covered with a copper coil. This coil is in turn connected with a high frequency voltage. Argon gas is fed into the system and produces argon plasma at the open end of the torch.

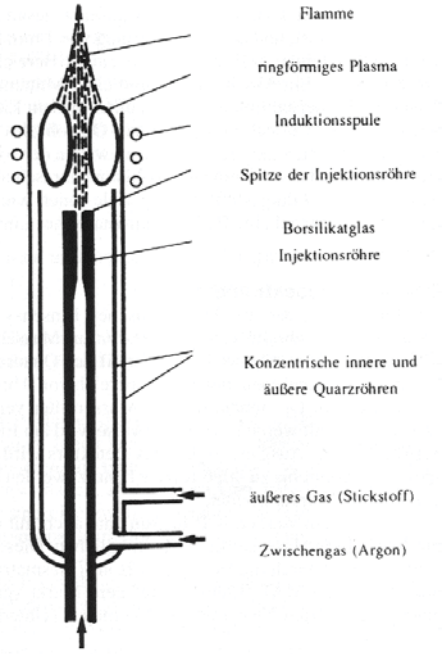

Figure 5.2: Design of a torch (Jochum *et al.* 2000).

In a first step the sample is brought into the plasma flow and ionized. Then the ions are separated from the plasma in an ion extraction interface. A quadrupole mass filter achieves mass separation. The mass filter is made up of four metallic sticks. Each opposed pair is connected electronically whereas a positive and a negative d.c. voltage of the same dimension are attached to either pair. A detector is counting the ions leaving this mass filter (Jochum *et al*. 2000).

Inserting the samples into the plasma flow can be maintained in two different ways. The injection of an aerosol is best for the analysis of fluids such as dissolved rocks (Jochum *et al.*, 2000). The second method is so called Laser Ablation (LA) – ICP-MS, which has the big advantage of omitting time intensive decomposition to obtain a solvent of the sample. In the latter case the material for the analysis is directly emitted of the solid materials by the interaction of the laser with the solid sample.

5.2.2. Application in this study

ICP-MS was used to obtain trace element and rare earth element composition data. Powdered samples were dissolved using a modified Na_2O_2 sinter decomposition technique (Meisel *et al.*, 2002)(Meisel et al., 2002). 0.1 g of sample material were mixed with 0.5 g of Na_2O_2 and homogenized in an oven at a temperature of 480°C. The resulting sinter cake is dissolved by adding H_2O and the residue in a second step with HCl. The dissolved sample is then diluted with distilled water in a ratio of 1:1000. Finally 4 ml 1% HNO_3 and 0.2 ml of solutions, each containing 1ppm Re and 1ppm In were added to 1 ml sample before the actual measurement.

Analysis was accomplished at the Department of General and Analytical Chemistry at the University of Leoben using a Hewlett Packard inductively coupled quadrupol plasma mass spectrometer (ICP-QMS) (HP 4500). Calibrations were accomplished with geological reference materials. Details can be found under http://institute.unileoben.ac.at/chemie/

5.3. X-ray fluorescence analysis (XRF)

5.3.1. Principles of XRF analysis

X-ray fluorescence analysis is a common method to gather qualitative and quantitative data of the element composition of geological materials. XRF analysis is to a great extent non-destructive because the X-rays used for analysis only invades the outermost parts of a sample (2 – 50 μm).

With the invasion of a beam a characteristic X-ray radiation of the atoms is induced by interaction with electron-, ion-, X- or gamma rays. Because of a direct coherence between chemical composition and fluorescence radiation this effect can be used in chemical analytics. The high-energy radiation induces a fluorescence radiation that is composed of a characteristic line spectrum for each element and the breaking continuum, inferred by the slowing down of activated radiation.

The energy of the animating radiation must therefore be at least as intense as the binding energy of the affected electron. Thus activation of K – lines of Fe (Z=26) cannot be maintained by a Cr – duct where Z = 24 (Weber-Diefenbach, 2000).

Irradiation of a sample by high-energy radiation (electron-, ion-, x-ray- or gamma rays) causes the removal of electrons out of the inner shells of affected atoms. Electrons of shells with a higher number of quanta thereupon fill up the resulting gap. Binding energy of these outer lying shells is higher than those of the inner lying ones and thus the resulting difference in energy is yielded in form of a so called X-ray quant (Weber-Diefenbach, 2000).

The radiation obtained in this way is distinctive for each element. Resulting K-, L- and M-lines are called discrete maxima of intensity and are caused by the fill up of missing electrons in the K-, L- or M-shell. Further distinction is achieved by a close look on the original orbitals of the substituting electrons (Figure 5.3). Their intensity decreases from K via L to M shell (Weber-Diefenbach, 2000).

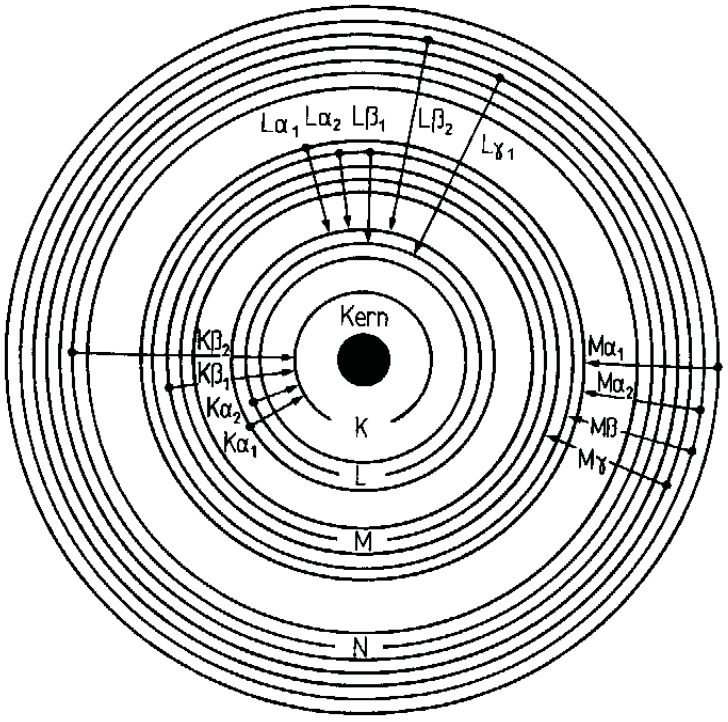

Figure 5.3: Most important lines of X-ray fluorescence radiation (Weber-Diefenbach, 2000)

The electrical field of atoms slows down the X-ray beam that penetrates the matter. The energy set free in this process is released stepwise as X-ray radiation. This braking radiation

or continuum radiation is additionally set free by the X-ray ducts besides the characteristical radiation (Weber-Diefenbach, 2000).

5.3.2. Assembly of XRF instruments

There are two different types of XRF modes used for analysis; the wavelength dispersive XRF (WDXRF) and the energy dispersive XRF (EDXRF) mode.

As shown in Figure 5.4 the emitted radiation of a sample in WDXRF mode is diffracted and reflected at the grid of an analyzer crystal after passing a so-called collimator. The fluorescence radiation is fractionated by the reflection according to the wavelength. Afterwards it hits the detector (Weber-Diefenbach, 2000).

With the EDXRF on the contrary the X-ray quant hits the semiconductor analyzer directly. Thus analysis can be maintained rapidly and simultaneously what is the big advantage of EDXRF (Weber-Diefenbach, 2000).

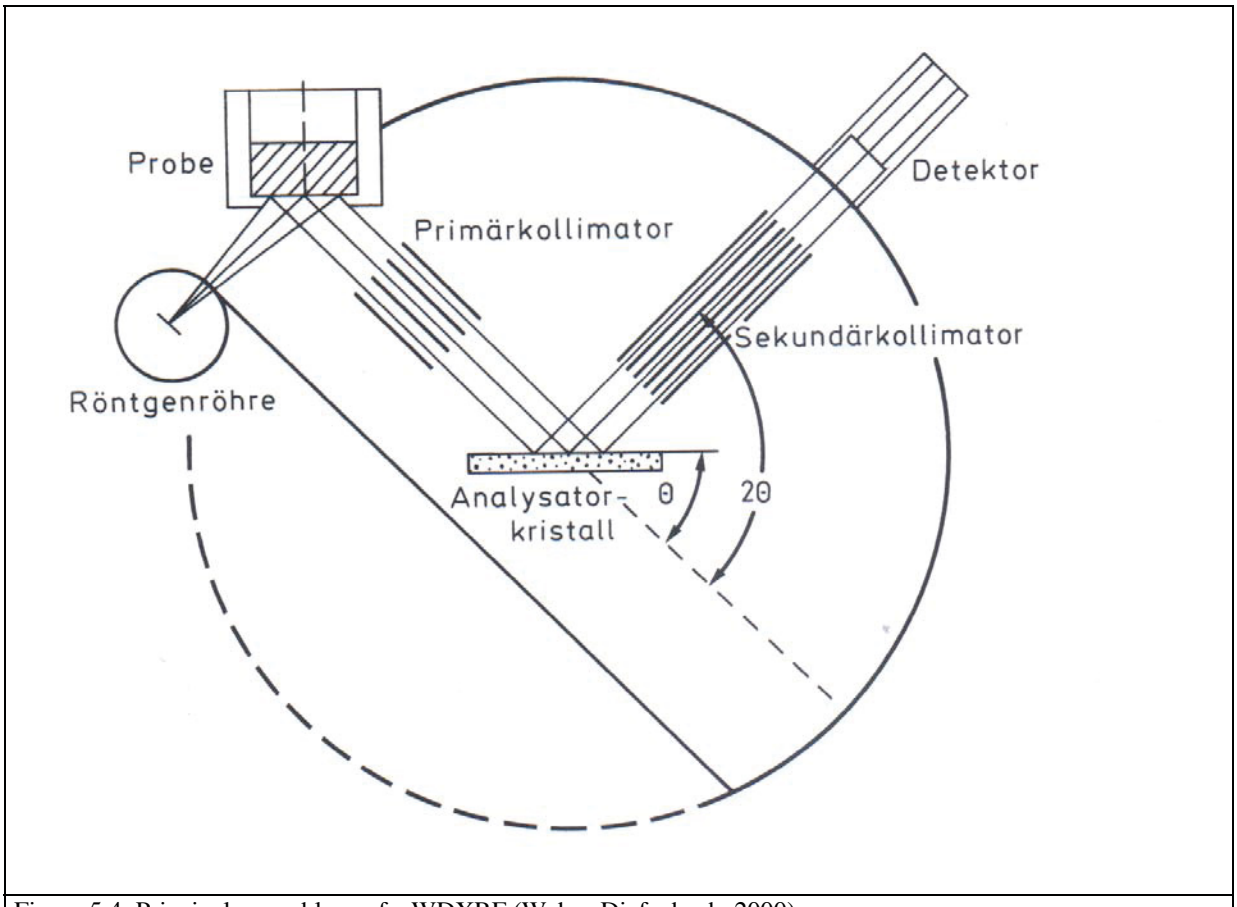

Figure 5.4: Principal assemblage of a WDXRF (Weber-Diefenbach, 2000)

5.3.3. XRF – analysis and this study

In this work XRF – analysis was used to obtain the major element distribution of the 35 samples studied. The analyses were accomplished at the Institute for Geosciences at Karl Franzens Universität Graz, using a wavelength dispersive X-ray fluorescence spectrometer Bruker Pioneer S4. The spectrometer was calibrated with 40 reference materials. Detection limits are 0.05 wt. % for major elements and 20 ppm for trace elements.

Major elements were analysed on fused discs prepared by melting of 1 g sample powder with 7 g of di-lithiumtetraborate as flux melting agent. This mixture was heated to 1300°C and casted to tablets to be measured automatically afterwards.

5.4. Electron microprobe analysis (EMP)

The electron microprobe is a combination of a light microscope, raster electron microscope and X-ray spectral analyser. In the electron microprobe a focused electron beam activates a characteristic X-ray spectrum in the solid sample (Pavicevic, 2000).

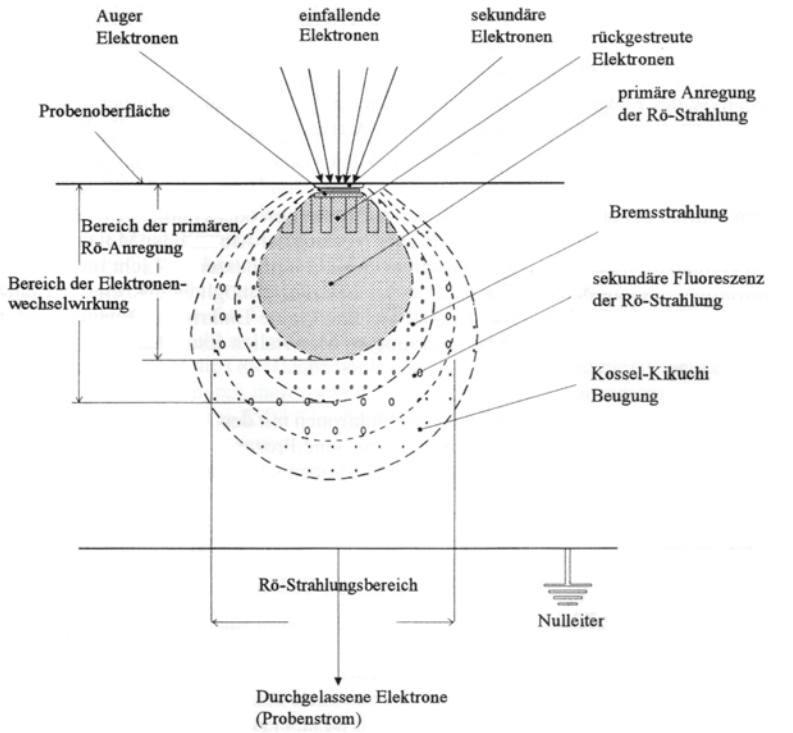

Figure 5.5: Schematical sketch of the interaction between primary electrons and solid sample (from Pavicevic, 2000)

EMP analysis is a microchemical method allowing in-situ analyses of solid materials. The advantages of EMP – analyses lie in the possibility to measure single grains in the matrix, the use of only small amounts of sample and the quantitative acquisition of the chemical variation within a single grain.

As shown in Figure 5.5 the incoming primary electrons of the beam interact with the atoms of the sample on and close to the sample surface. This leads to the generation of a primary X-ray radiation by effects of scattering. Knowledge of the kind and quantity of elements can be obtained from the emitted wavelength and the intensity of the characteristic X-ray spectrum.

A further effect is the inelastic scattering of incoming electrons when interacting with atoms of the sample. These inferred secondary electrons (SE) are dependent on the energy of the beam and the atomic number of the sample. Analysis of secondary electrons allows us to define the structure of the sample. However, a flat sample surface is a precondition (Pavicevic, 2000).

Analysis of emitted element-characteristic X-ray radiation can be maintained by two different means; wavelength dispersive spectrometry (WDS) or energy dispersive spectrometry (EDS).

The WDS diffracts the X-ray spectrum at analyser-crystals, which are afterwards registered and counted. For a proper quantitative analysis the element concentration in the sample is compared to the concentration in a standard (Pavicevic, 2000).

The EDS on the contrary analyses the sample by using a semi-conducting detector. In most cases Si- or Ge diodes are being used (Pavicevic, 2000).

5.4.1. EMP and this study

In this thesis EMP analysis was used to gather data about the mineral chemistry of samples. This was done with a JEOL-JXA 8200-WD/ED combined microanalyzer microprobe at the Chair of Mineralogy and Petrology at the Department of Applied Geosciences, University of Leoben. The instrument is part of the E. F. Stumpfl microprobe laboratory of the Universitätszentrum Angeandte Geowissenschaften Steiermark (UZAG).

Measurements were done with an accelerating voltage of 15 kV at 1.185 E^{-8} A and with a probe diameter of 5 μm for 9 elements (Si, Ti, Al, Fe, Mn, Mg, Ca, Na, K). For different minerals different standards were used (Table 5.1). The applied correction for all analyses is ZAF.

Mineral group	Garnet	Ilmenite	Plagioclase
SiO_2	Garnet_S06	S08_Kearsutit	S08_Kearsutit
TiO_2	Titanit_P26	Titanit_P26	S08_Kearsutit
Al_2O_3	Garnet_S06	S08_Kearsutit	S08_Kearsutit
FeO	Garnet_S06	Ilmenite	S08_Kearsutit
MnO	Rhodonite_S23	Rhodonite_S23	Rhodonite_S23
MgO	Garnet_S06	S08_Kearsutit	S08_Kearsutit
CaO	Titanit_P26	S08_Kearsutit	S08_Kearsutit
Na_2O	Jadeite_P31	Albite_S02	Albite_S02
K_2O	Adular_S01	Adular_S01	Adular_S01

Table 5.1: Standards used for different mineral groups; the standardisation for plagioclase was also used for micas.

6. Petrography

In this chapter the petrography of rocks important for this study area will be described in more detail. For descriptive purposes four groups of rocks are distinguished; i.e. metabasites including metamorphosed pillow basalts, calc-silicate rocks, metapelites, and meta-ultramafic rocks.

6.2. Calc-silicate rocks

Confirming field observations calc-silicate rocks are classified in two groups. The first group includes calc-silicate rocks developed through alteration of pillow basalts (Type I). The second group (Type II) includes the scheelite- bearing calc-silicate rocks.

6.2.1. Type I calc-silicate rocks

Type I calc-silicate rocks formed during calc-silicate alteration of the inner zones of pillow cores. They have high contents of epidote, clinopyroxene, plagioclase and quartz. Calcite, garnet and scapolite can sporadically be found as well as ilmenite and titanite. The metamorphic paragenesis of wallrocks not affected by this kind of alteration is characterised by the occurrence of hornblende, plagioclase, ± clinopyroxene, ± epidote.

Sample JR05C42A

This thin section was prepared from the core zone of a dm-sized pillow structure (Chapter 4; Figure 4.3.2 & Figure 4.3.3). It exhibits the transition from a coarser grained inner part of the pillow to the less altered outer core zone.

Epidote-group minerals, clinopyroxene, plagioclase are the major mineral phases of this sample. Hornblende and quartz are minor constituents, titanite is an accessory phase. Two parts, separated by a gradational transition zone, can be distinguished in this thin section with respect to grain size and variation of modal composition. The inner core part is composed of large, up to mm-sized anhedral clinopyroxene and epidote grains and minor quartz, plagioclase and hornblende. It shows a gradational transition into a zone of much smaller

grain size (average gain size is about 0.1 mm; Figure 6.2.1). This fine-grained zone is composed of plagioclase, quartz (?), hornblende and clinopyroxene and minor epidote defining a granoblastic to nematoblastic fabric. Clinopyroxene tends to form slightly larger poikiloblastic to skeletal crystals overgrowing the fine-grained plagioclase + hornblende assemblage. In the transition zone between the two parts large poikiloblastic clinopyroxene plus minor epidote are to be found. They are rich in inclusions (of most likely plagioclase and/or quartz) but otherwise they look very similar to the large clinopyroxene and epidote grains in the inner zone (Figure 6.2.2).

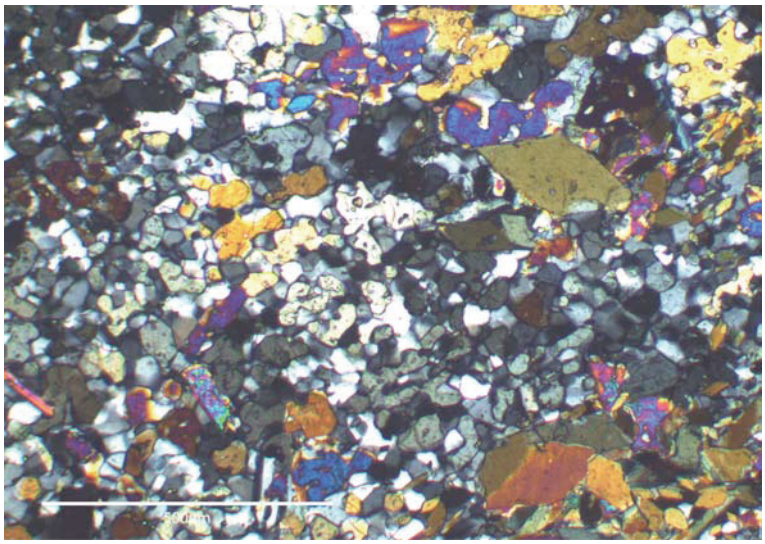

Figure 6.2.1: Fine grained hornblende, plagioclase and epidote from outer zone of sample C42A

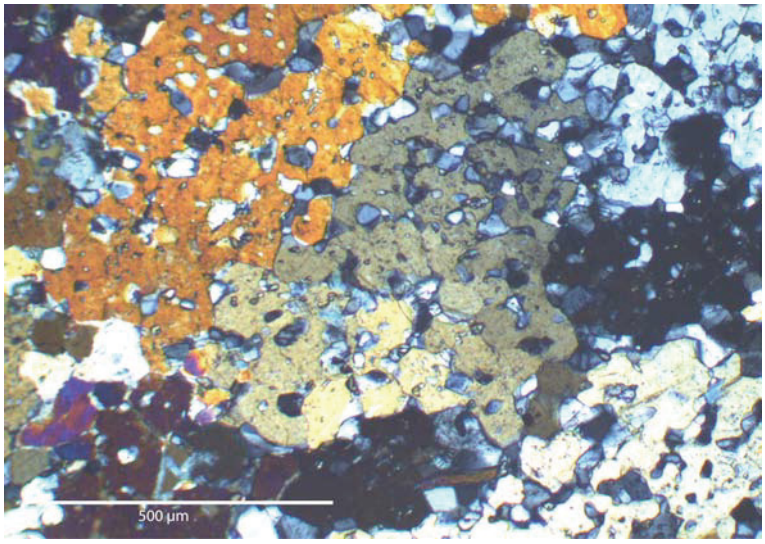

Figure 6.2.2: Sample C42A; Large inclusion-rich clinopyroxene grains with minor epidote and quartz.

Sample JR05C57A - Metabasite with calc silicate – quartz veins

In this section unaltered metabasite and calc-silicate alteration related to veining can be observed. The main minerals in the unaltered metabasite are hornblende, plagioclase and

clinopyroxene + biotite. These minerals are fine-grained and define a preferred planar grano- to nematoblastic fabric. Clinopyroxene tends to form larger anhedral poikiloblastic to skeletal grains. Epidote crystallised post-kinematically (Figure 6.2.3). The sample is crosscut by several thin (mm to < 1cm) quartz veins, which in addition to quartz contain minor clinopyroxene, epidote, calcite and plagioclase. These discordant veins are deformed as indicated by folding and rotation of the veins into the planar fabric.

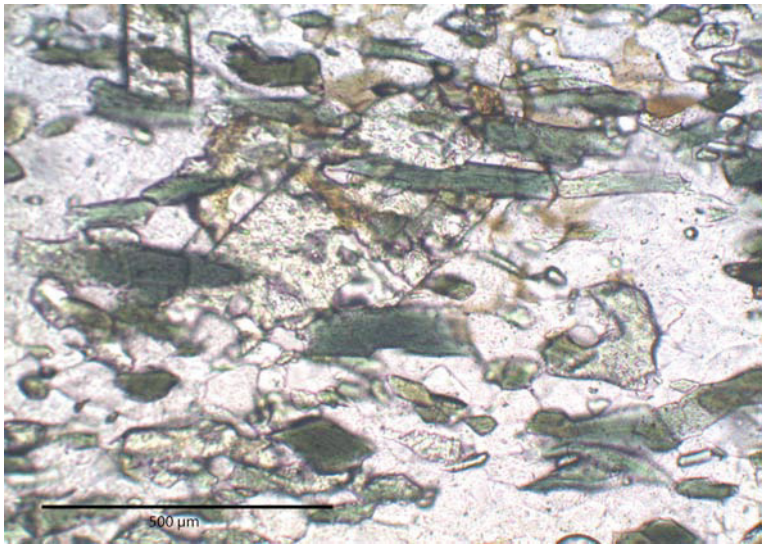

Figure 6.2.3: Epidote grain postkinematically overgrowing hornblende + plagioclase etc; sample C57A.

Sample JR05C57B - Metamorphosed pillow basalt with Type I calc-silicate alteration

This thin section (5 x 5 cm) of a pillow basalt shows the gradation from a core zone into the outward zones of a pillow richer in darker minerals within a cm scale (Figure 6.2.4). Three mineralogically distinct zones can be distinguished; i.e. an outer zone rich in darker minerals with partly preserved planar fabric, an intermediate epidote-rich zone (zone 2) and an inner zone containing light minerals (zone 3). Zone 1 is essentially composed of the fine-grained metabasite assemblage clinoamphibole (hornblende?) + plagioclase + clinopyroxene + quartz ± epidote. An oriented planar fabric defined by variation in modal contents of these minerals is preserved. These parts of the section show a fine-grained grano- to nematoblastic microfabric. In some bands/layers euhedral epidote crystals overgrow this fabric. These epidote cystals are not oriented and must therefore have grown post-kinematically with respect to the main planar fabric in the metabasite. Zone 2 is composed of epidote + quartz+ clinopyroxene ± clinoamphibole. Locally there is interstitial scapolite. Zone 3 in the pillow core is composed of coarse-grained quartz + scapolite. Scapolite has a similar refraction of light as quartz but it can be discriminated from quartz by its higher birefringence, the presence

of cleavage, and especially by its uniaxial negative optical character. Furthermore scapolite has a tendency to develop euhedral to subhedral morphology (Figure 6.2.5).

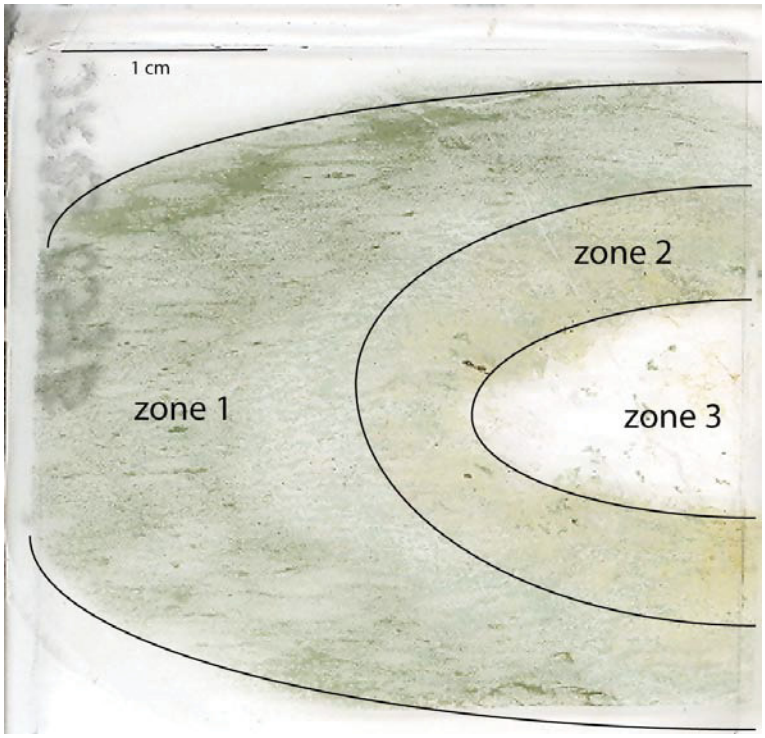

Figure 6.2.4: Three zones can be distinguished in thin section C57B; see text for details.

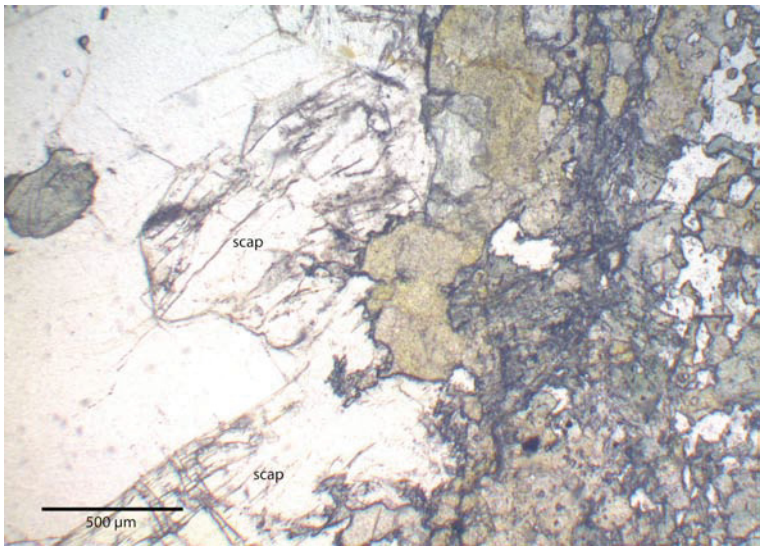

Figure 6.2.5: Contact of the inner core zone of sample C57B with scapolite + quartz to epidote-rich zone 2.

Sample C67A – Altered pillow basalt with calc-silicate core

This sample of Type I calc-silicate rocks can be divided into two different microareas. Area 1 is mainly composed of plagioclase + epidote + quartz, which make up the coarse-grained (grains up to 1 mm) granoblastic fabric. A layering is defined by coarser and finer grained layers of the same minerals. Epidote may also form some larger anhedral crystals with

inclusions of e.g. quartz and titanite. Plagioclase shows polysynthetic twinning and some grains show optical zoning. Plagioclase contains tiny inclusions titanite (Figure 6.2.6). The plagioclase-rich zone of this thin section has a perfect granoblastic fabric.

Plagioclase + epidote + clinopyroxene + quartz make up the mineral assemblage of area 2. Clinopyroxene is forming anhedral grains that are concentrated in layers. Partly zoned epidote shows a reaction corona with symplectitic clinozoisite / epidote.

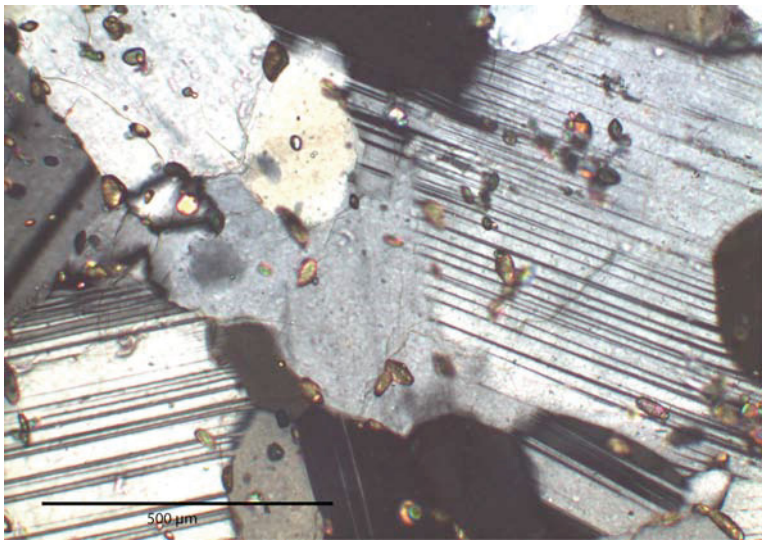

Figure 6.2.6: Inclusion rich feldspar grains from sample C67A-II.

6.2.2. Type II calc-silicate rocks

The main constituents of this type of calc-silicate rocks are quartz, clinopyroxene, epidote and garnet. In some cases titanite and clinozoisite can accessorily be found.

Sample JR05C55A is from the contact between a metabasite and a Type II calc-silicate rock. The metabasitite (Zone 1) shows nematoblastic fabric containing pleochroic hornblende and interstitial plagioclase ± quartz. Hornblende crystals are aligned in the main planar fabric together with xenoblastic clinopyroxene (Figure 6.2.7). The clinopyroxene xenoblasts are elongated and also oriented in the main planer fabric. Titanite is an accessory phase.

Zone 2 is dominated by epidote + clinopyroxene + titanite of variable grain size and modal amounts in individual layers. Whereas the contact to zone 1 is extraordinary rich in epidote the amount of clinopyroxne increases away from this gradational contact.

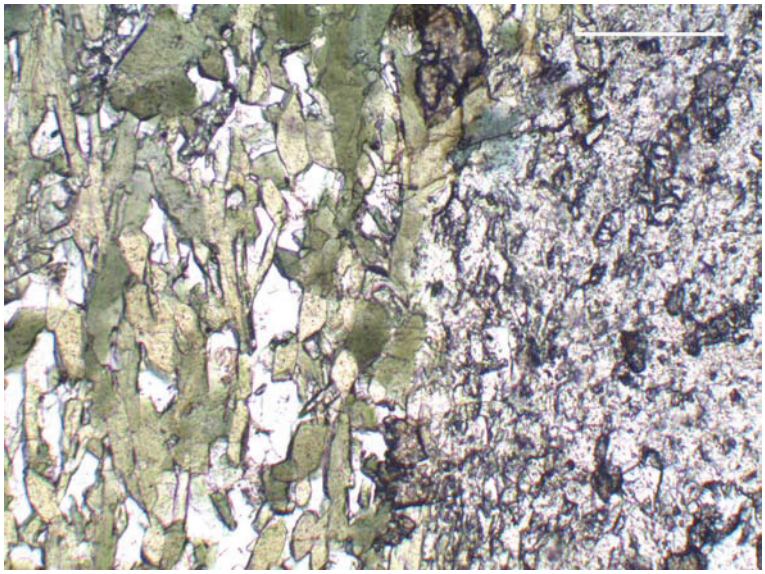

Figure 6.2.7: Transition from amphibole (Zone 1, left) to calc-silicate area (Zone 2, right) of sample C55A.

Sample JR05C73A

This thin section was made from the contact zone of unaltered metabasite to Type II altered calc-silicate rocks. In this thin section several micro-areas are to be distinguished.

The unaltered metabasite is composed of amphibole, plagioclase, quartz and some minor epidote and accessory titanite formed from replacement of ilmenite. As shown in Figure 6.2.8 the mineral assemblage is well equilibrated showing a grano- to nematoblastic fabric. Amphibole is aligned in the planar fabric and parallel to the contact with the altered zone.

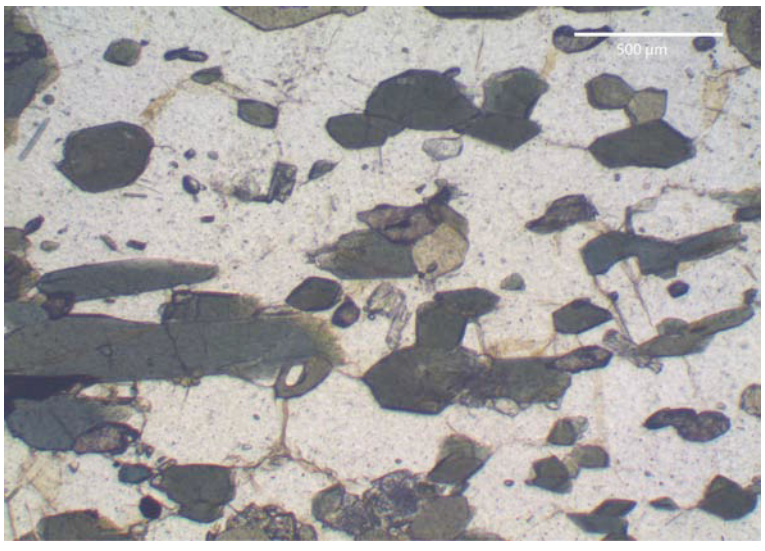

Figure 6.2.8: Unaltered part of sample C73A;

The altered zone is composed of a coarse-grained assemblage of quartz + epidote + clinopyroxene + garnet (Figure 6.2.9). Relics of minor calcite are preserved in garnet. Garnet

tends to develop euhedral morphology when in contact with quartz. Delicate growth zoning and a change in colour from core to rim (colourless to weakly “brownish”) are observed in some euhedral garnet crystals. Titanite is an accessory phase.

The transition zone between the unaltered and altered rock shows a variable mineralogical composition with changes on the cm scale. Generally an increase in quartz is observed towards the calc-silicate assemblage. Next to the unaltered metabasite there is an about 1 cm thick zone rich in epidote. This edpidote often exhibits symplectitic microtexture (Figure 6.2.10). Epidote is associated with a colourless clinoamphibole, most likely tremolite, minor quartz and titanite. The epidote-rich layer grades into a zone containing thin foliation-parallel quartz-epidote veins. Clinozoisite ± tremolite seem to overprint the earlier epidote-rich assemblage. Within one layer an unknown mineral has been totally replaced by very fine-grained aggregates of a colourless pyllosilicate, most likely talc.

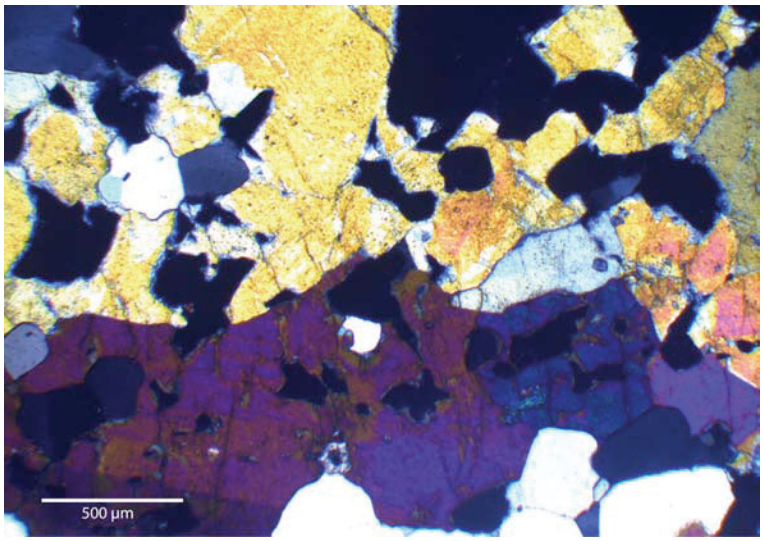

Fig 6.2.9: Large, partly well defined grains of epidote + clinopyroxene + garnet from the altered part of sample C73A.

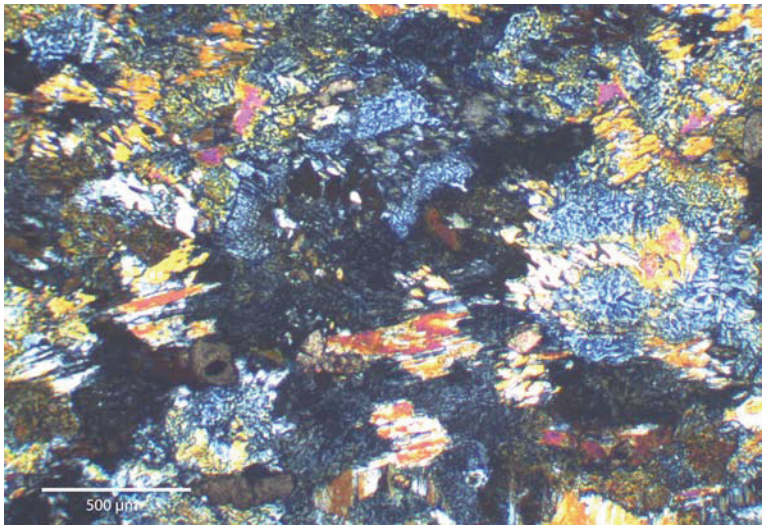

Figure 6.2.10: Epidote and clinopyroxene grains in the transition zone of sample C73A are anhedral and show symplectitic intergrowths.

Sample JR04IV10C

This thin section was prepared from the contact zone of a calc-silicate rock to an amphibolitie.

Clinopyroxene and epidote make up the major part of this thin section. They form finer-grained domains with a granoblastic fabric which are especially rich in clinopyroxene. In some areas additional garnet as well as ± epidote and accessory titanite is occurring. Garnet is generally highly irregular and is often replaced by clinopyroxene and epidote. As shown in Figure 6.2.11 this part of the section is crosscut by a late thin vein of epidote. Other domains are very coarse-grained and are made up of epidote/clinozoisite + clinopyroxene + titanite.

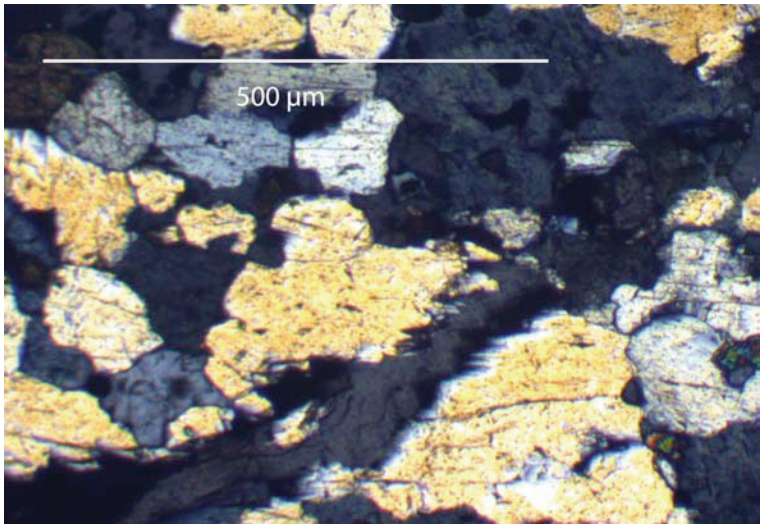

Figure 6.2.11: Epidote veinlet crosscuting larger clinopyroxene crystals; sample IV10C.

Sample JR04IV20B

Sample JR04IV20B is a Type II calc-silicate rock that for descriptive purposes is divided into two separate microareas. Area 1 is composed of plagioclase + quartz + clinoamphibole + biotite ± epidote. Biotite and hornblende define a planar fabric that is aligned in foliation. Clinoamphibole grains are sometimes overgrown by symplectitic epidote. The rock can be named a biotie-hornblende- gneiss. Towards the transition to area 2 more symplectitic epidote is occurring. Additionally reaction textures around relics of clinopyroxene are observed. Clinopyroxene is altered to clinoamphibole, which is colourless and shows oblique extinction and is thus identified as tremolite but also shows epidote coronas (Figure 6.2.12, Figure 6.2.13). Plagioclase and quartz form a finer-grained granoblastic fabric.

Area 2 is relatively rich in clinopyroxene ± epidote ± titanite. The layered granoblastic fabric is medium- to coarse-grained with variable grain size of clinopyroyene. This could due to varying degrees of recrystallisation in individual layers. Epidote is concentrated in some layers and it also recrystallised to a patchy mosaic. Partly, it replaces clinopyroxene in some layers.

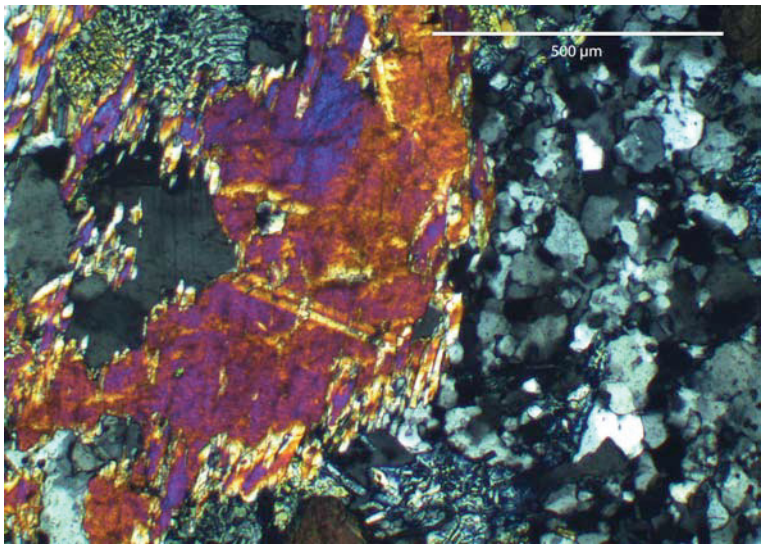

Figure 6.2.12: Altered clinopyroxene with reaction rim / core to quartz, plagioclase and clinozoisite; sample IV20B..

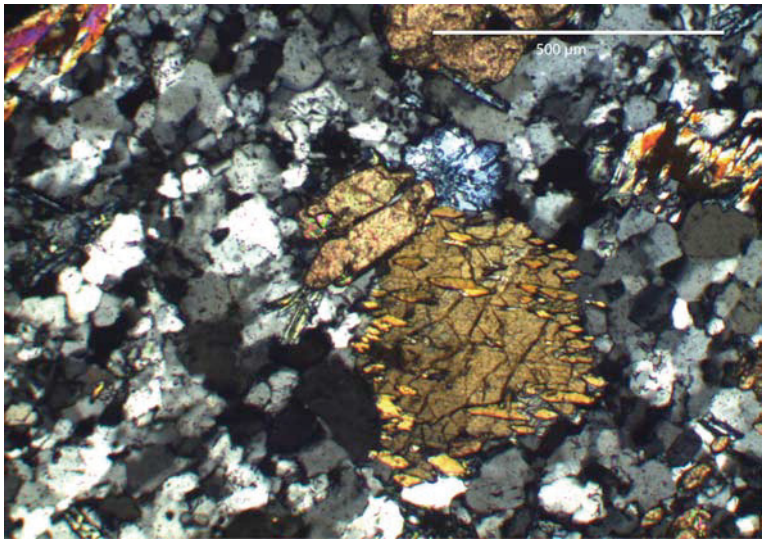

Figure 6.2.13: Clinopyroxene altered to lighter yellow clinoamphibole; sample IV20B.

6.2.3. Scheelite-rich calc-silicate rocks

Scheelite in Ivisaartoq is bound to Type II calc-silicate rocks. These rocks have the same petrographic composition as Type II calc-silicates described in chapter 6.2.1 but are distinguished by the occurrence of higher amounts of scheelite. Scheelite in these samples has already been observed macroscopically using a UV lamp and was carefully studied under the microscope.

Sample JR052T16 – Scheelite-bearing calc-silicate rock

Epidote + garnet + quartz is the dominant mineral assemblage in this calc-silicate sample. Some calcite grains occur in minor amounts. The fabric is generally relatively fine-grained. Garnets are rather anhedral and surround / include calcite + quartz + epidote grains. The granoblastic fabric is crosscut by one single mm-sized garnet-epidote vein. Scheelite occurs in minor amounts but forms relatively large mm-sized porphyroblasts as shown in Figure 6.2.14. Bigger scheelite porphyroblasts can be observed in the hand specimen where scheelite grains of up to 5 cm can be seen. They show ble fluorescence in ultraviolet light. Scheelite porphyroblasts contain several trails of unidentified inclusions.

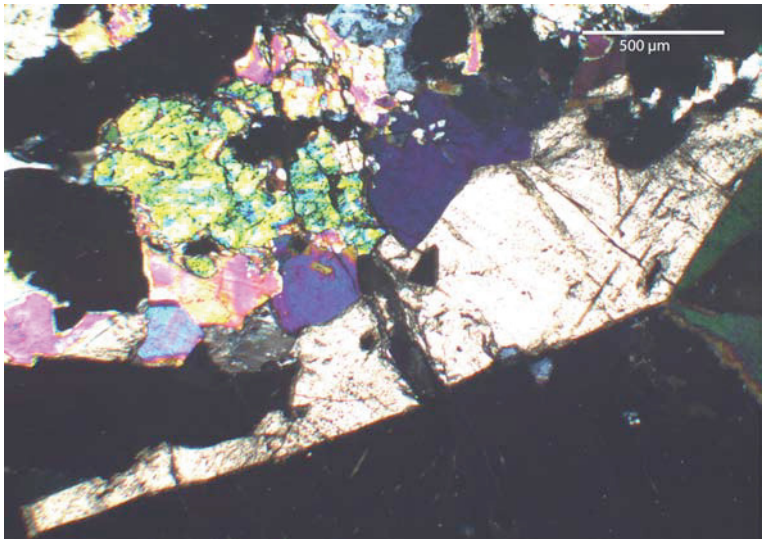

Figure 6.2.14: Scheelite with epidote and garnet; sample 2T16

2T19 Scheelite-bearing calc-silicate marble

The main minerals in this sample are epidote, clinopyroxene and calcite, which is more common compared to other samples of this type, whereas quartz is less common. The non-oriented fabric of this sample is characterised by the occurrence of rather small grains that reach diameters of up to 1 mm (Figure 6.2.14). Scheelite grains are rather small (~ 0.1 mm) and always occur as inclusions in other minerals such as epidote.

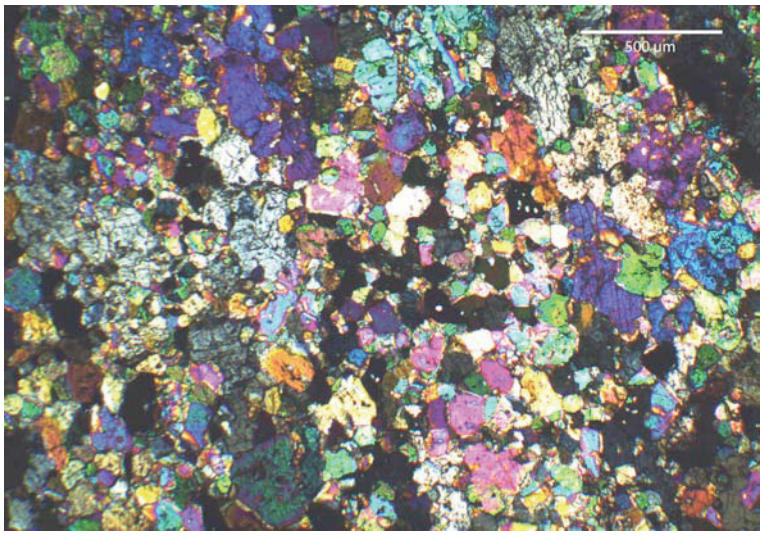

Figure 6.2.15: Granoblastic fabric in sample 2T19

C51B-1- Scheelite-bearing calc-silicate rock

The major mineral phases are epidote, clinopyroxene, diopside and calcite, whereas garnet is a minor constituent and titanite and scheelite are accessories. Epidote forms large skeletal to

poikilitic grains. Clinopyroxene grains are generally smaller but some large grains with microfractures filled with epidote and calcite can be seen. Locally clinopyroxene recrystallised. Accessory titanite tends to form euhedral grains. Scheelite often is in contact with clinopyroxene (Figure 6.2.16) but it is additionally associated with calcite and garnet patches. The grain size of this sample is very fine and no oriented fabric is noticeable and all minerals form intergrowths and inclusions with or within each other. The higher amount of calcite in this sample was already mentioned. It occurs interstitially between the other minerals but in one case also forms a small vein. In some cases it seems as if the calcite replaces garnet.

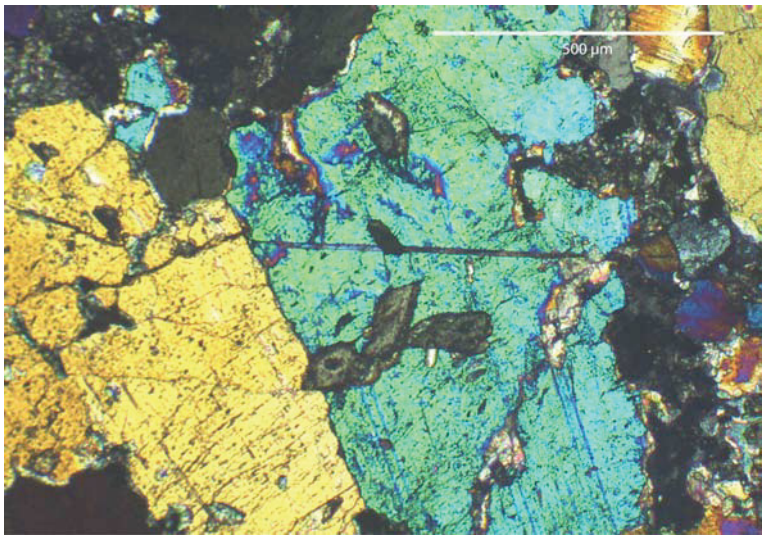

Figure 6.2.16: Scheelite minerals in calc-silicate rock; sample C51B-1

JR04IV5/4 – Scheelite-bearing calc-silicate rock

This sample represents a coarse-grained calc-silicate assemblage composed of quartz + epidote + garnet + diopside. Occasionally calcite and titanite are present. The rock is coarse-grained with an average grain size of 1.5 mm reaching up to 3 mm. Scheelite belongs to this coarse-grained calc-silicate fabric but it is of much smaller grain size (Figure 6.2.17). Scheelite is rich in tiny inclusions of other minerals, which were too small to be identified under the microscope. This coarse-grained zone is in contact with a zone of much smaller grains of the same minerals. The dominant mineral in this finer grained zone is garnet. One can have the impression that the zone is made up of only one big but strongly degenerated garnet grain. All other minerals seem to be replacing this decomposed garnet grain

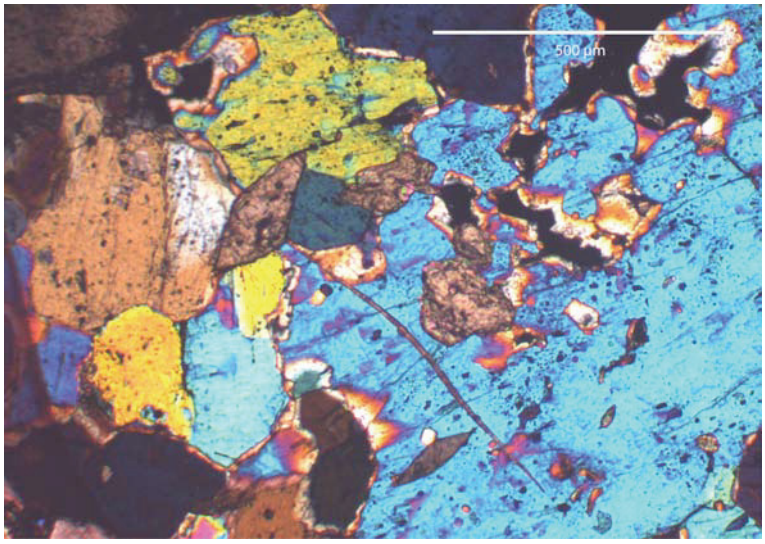

Figure 6.2.17: Scheelite minerals in epidote; sample IV5/4

6.3. Metapelitic rocks

The mineral paragenesis of these rocks is considered being excellent for geothermobarometric investigations. The matapelites studied contain quartz + garnet + muscovite + biotite + plagioclase ± sillimanite and accessory staurolite as well as sporadic apatite. Especially the micas and sillimanite defin a well-oriented fabric. But also quartz and plagioclase domains can be more or less orientated. Micas and sillimanite wrap around garnet porphyroblasts. In some cases tiny inclusions of sillimanite and muscovite are included in quartz and plagioclase. These inclusions trails show a similar orientation as the in the mica-rich matrix.

Sample JR05C71B – Garnet-biotite-sillimanite schist

The metamorphic assemblage of this metapelite is garnet + biotite + sillimanite + muscovite + quartz + plagioclase. Due to its modal composition and its porphyroblastic to fibro-/ nematoblastic fabric the rock is termed a garnet-biotite-sillimanite schist.

Garnet forms spectacular up to cm large porphyroblasts, which preserve two growth stages; i.e. inclusion-rich cores and inclusion-free rims (Figure 6.3.1). The garnet cores contain trails of aligned and rotated inclusions, mainly of quartz with some minor opaque phases. The internal foliation (s_i) defined by these trails is different to the external one (s_e), which is defined by the biotite-sillimanite fabric in the surrounding matrix. The outer garnet zones lack these small inclusions although larger quartz grains containing fibrolitic sillimanite inclusions are intergrown with the garnet rims (Figure 6.3.2). In the matrix biotite-sillimanite rich layers

alternate with quartz-plagioclase rich layers. Muscovite is a minor phase. Staurolite has been identified as a relict phase within plagioclase. Tourmaline, apatite, ilmenite and magnetite are accessories.

Two crystallisation stages of garnet are preserved in this rock, each with a corresponding stage of deformation. The garnet cores overgrow an early fine foliation, now only preserved by the quartz-rich inclusion trails within garnet. The rotation of these trails indicates that the garnet cores must have formed syn-kinematically with respect to this *early* (pre-peak metamorphic) deformation. The inclusion-free garnet rims coexist with sillimanite + biotite + quartz and are interpreted to have formed during peak metamorphism. The continuation of the folded / bended biotite + sillimanite fabric into the outer garnet zone (Figure 6.3.2) indicates that the peak assemblage formed syn-kinematically during development of the main S1 foliation of the schist. Because the internal and the external foliation show different orientation and because there is a sharp boundary between the two growth stages (Figure 6.3.1) it can be speculated that the two growth stages did not form in a continuous metamorphic process.

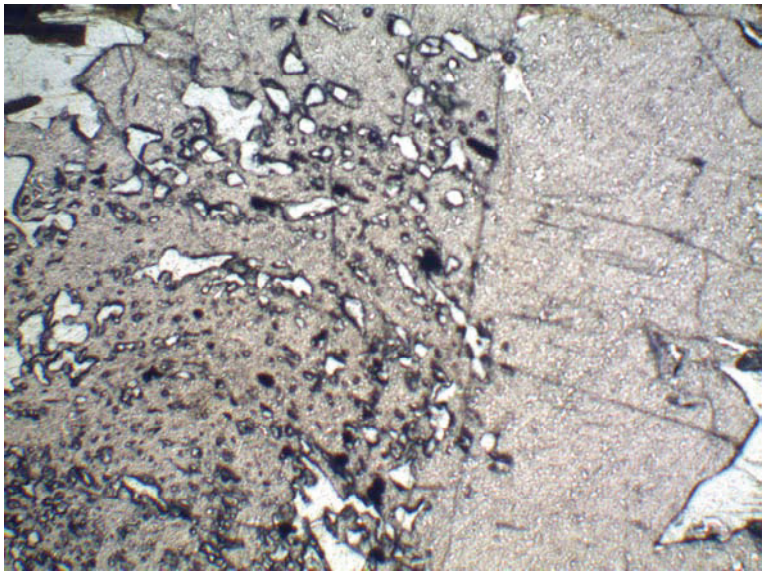

Figure 6.3.1: Inclusion-rich garnet core(left) and inclusion-free garnet rim (right); sample C71B.

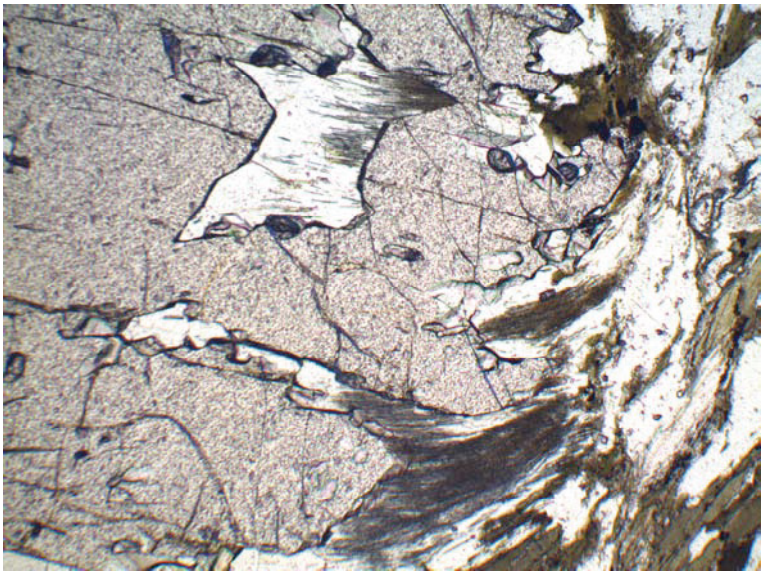

Figure 6.3.2: Edge of garnet grain from sample C71B; surrounding minerals are clearly bent around the garnet grain

Sample JR04IV6D – Garnet-bearing biotite-sillimanite gneiss

The assemblage of this rock is made up of quartz + muscovite + biotite + sillimanite + plagioclase + garnet. Considering its modal composition and the fibrolitic to nematoblastic fabric especially of sillimanite and biotite this rock can be named a garnet-bearing biotite-sillimanite schist.

The sample is characterised by the clear alignment of both mica and fibrolitic sillimanite defining the main foliation in this rock. Plagioclase often contains oriented inclusion trails of sillimanite and / or muscovite ± quartz (Figure 6.3.3). This internal orientation of trails in palgioclase is approximately parallel to the external foliation defined by coarser sillimanite and micas. Garnet forms ± euhedral porphyroblasts that are rich in inclusions, mainly quartz. Contrariwise to sample C71B these inclusions do not show a distinct orientation. Tourmaline, apatite, zircon and opaques are minor accessory phases.

Only one direction of foliation is preserved in this rock. Inclusion trails in feldspars are about parallel to the main external foliation.

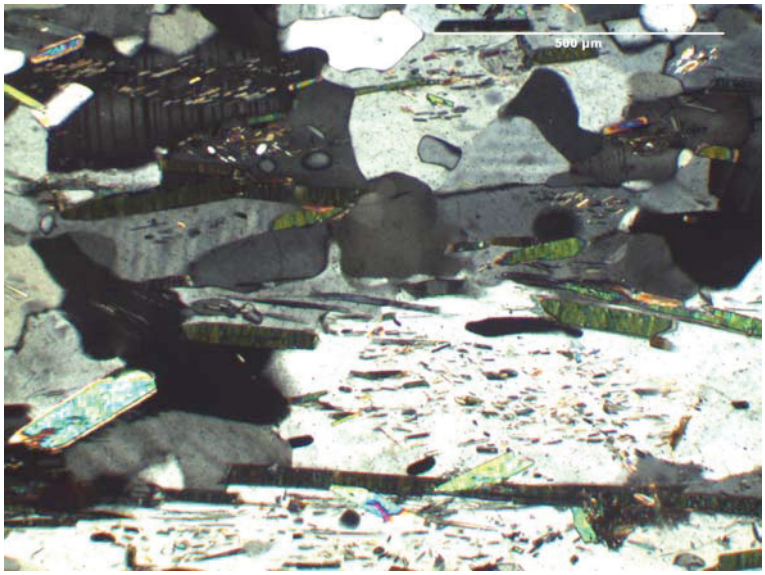

Figure 6.3.3: Sillimanite-rich inclusion trails in inf Feldspar grains of sample IV6D.

Sample JR04IV6E – Garnet-bearing metepelite

The mineral assemblage of sample IV6E is very similar to that of sample IV6D. The main constituents are quartz + plagioclase + biotite + sillimanite + garnet ± muscovite. Relictic staurolite and tourmaline are accessories. The porphyroblastic to nematoblastic frabric and the modal composition describe this rock as garnet-bearing biotite-sillimanite schist.

A clear foliation defined by biotite and sillimanite can be observed. They define a penetrative foliation and are aligned around garnet crystals (Figure 6.3.5). Also quartz and plagioclase grains are preferentially oriented in this foliation. Similar to sample IV6D plagioclase may contain inclusions of biotite as well as sillimanite and as a relictic phase staurolite (Figure 6.3.4). These inclusions do not show a preferred orientation.

The staurolie relics indicate that this mineral was stable during prograde metamorphism but reacted to biotite + sillimanite + garnet during peak metamorphism.

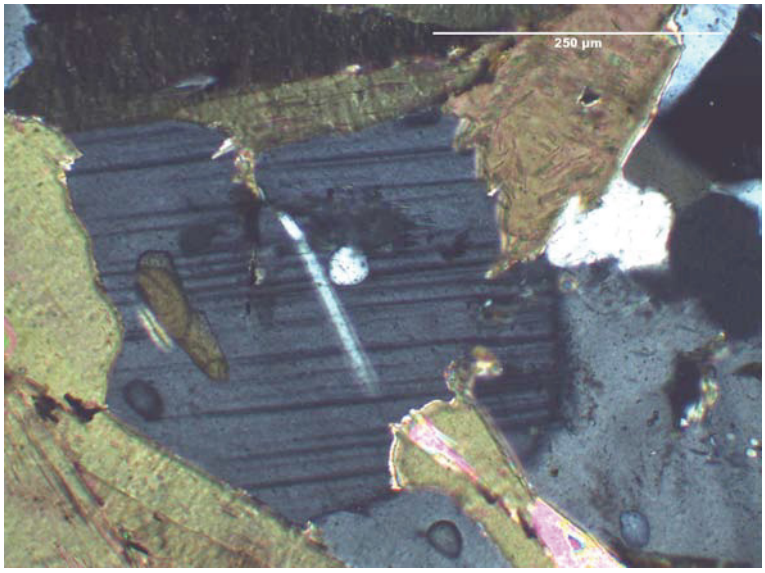

Figure 6.3.4: Inclusion of staurolite in plagioclase; Sample IV6E.

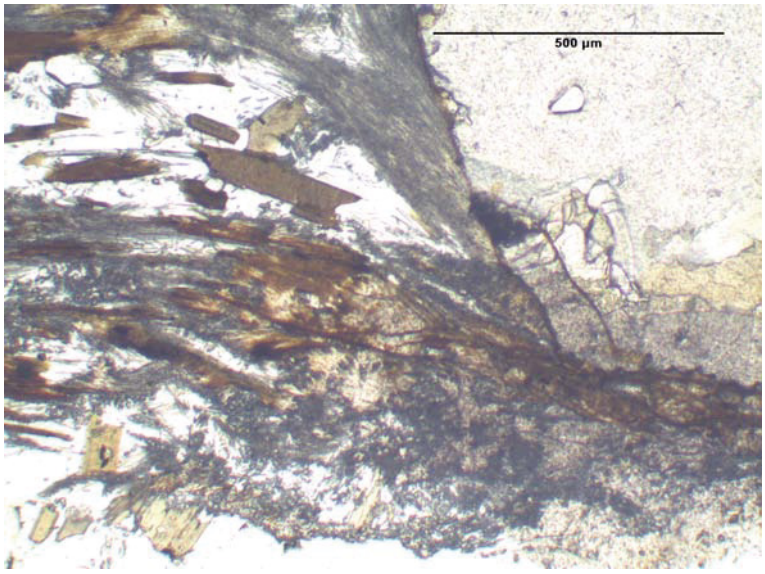

Figure 6.3.5: Contact between garnet (top right), sillimanite and muscovite; Sample IV6E.

Sample JR04IV26F – Biotite–hornblende schist

In this sample two main layers can be distinguished. One is dominated by a garnet + biotite assemblage. Garnet occurs in form of large anhedral porphyroblasts whereas biotite-rich planes alternate with quartzo-feldspatic planes. In some cases biotite shows chloritisation. Amphibole is very minor this layer. A coarse-grained quartz vein crosscuts the fabric (Figure 6.3.6). The second layer on the other hand is dominated by amphibole + plagioclase + quartz with minor garnet and garnet-rich layers are aligned in the main foliation. Some amphiboles show a zonation with brighter cores and darker rims.

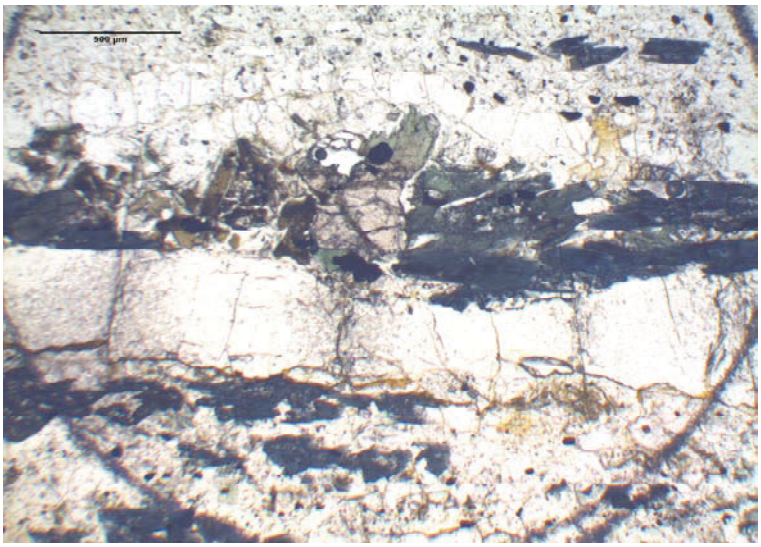

Figure 6.3.6: Thin section of sample IV26F; amphibole + garnet + plagioclase with foliation parallel qtz-vein.

Sample JR04IV33 – garnet-biotite-sillimanite schist

This rock is dominated by biotite + sillimanite + quartz + plagioclase ± muscovite. The main schistosity is defined by micas, especially biotite. However, big elongated sillimanite aggregates are most eye-catching. In some cases they are of a fibrolithic occurrence but can occur as bigger needles, too. The coarser-grained sillimanite has clearly developed later than the fibrolitic variety (Figure 6.3.8). Garnet forms up to cm large anhedral to subhedral porphyroblasts preserving two growth stages. The cores of these garnet grains are inclusion-rich whereas the rims are inclusion-free (Figure 6.3.7). To different inclusion assemblages can be reported: A quartz rich assemblage and one with ilmenite ± biotite.

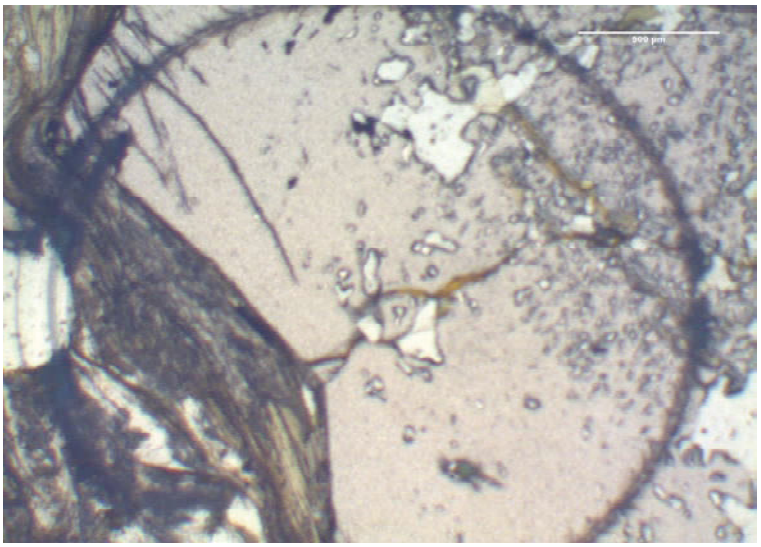

Figure 6.3.7: Thin section of sample IV33; two phase grt-grain with qtz-inclusions in the core surrounded by sillimanite + biotite intergrowths.

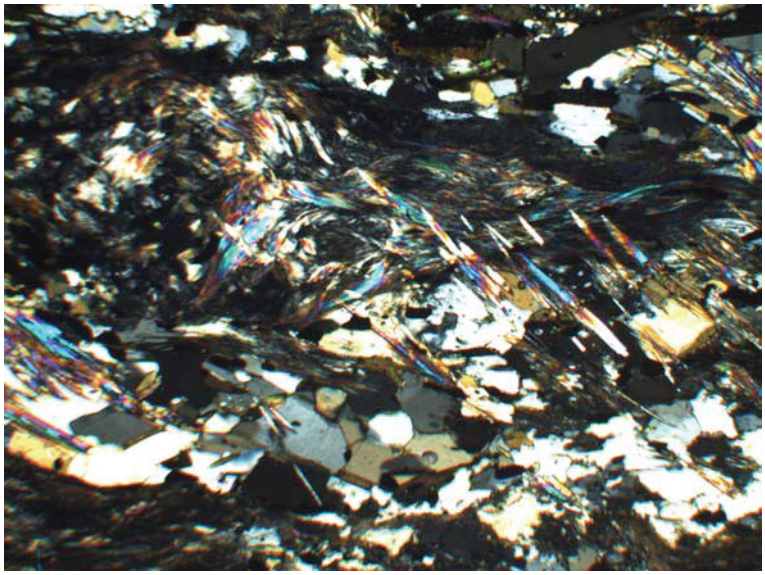

Figure 6.3.8: Two generations of sillimanite in sample IV33, coarse-grained sillimanite needles grow oblique over fibrolitic aggregates.

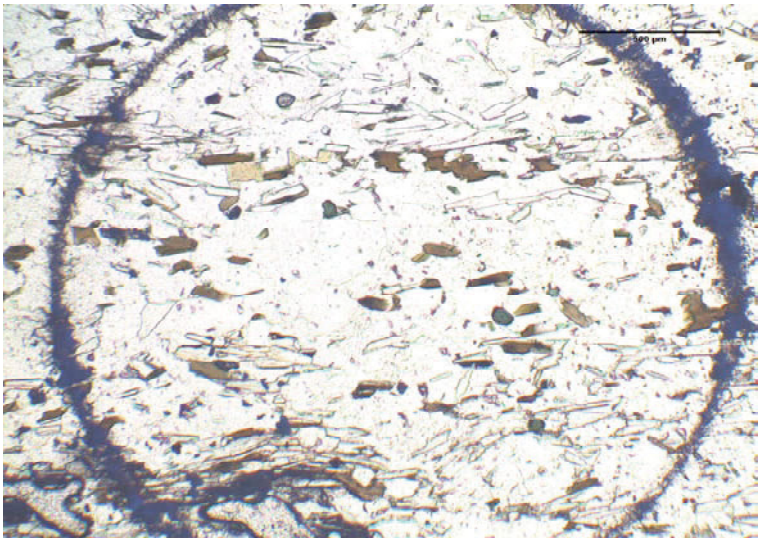

Figure 6.3.9: Thin section of sample IV37A; intercalation of biotite and muscovite with tourmaline and plagioclase.

Sample JR04IV37A – Biotite-muscovite gneiss

The matrix of sample JR04IV37A, a biotite-muscovite gneiss, is a fine grained assemblage dominated by quartz with minor occurrence of plagioclase. Biotite + muscovite–richer layers define the well-developed planar fabric and the continuous schistosity (Figure 6.3.9). Accessory tourmaline + apatite ± staurolite may also occur. This sample is characterised by a relatively small grain size and the whole fabric can be described as grano- to lepidoblastic. Individual larger, polycrystalline quartz grains are ± aligned in the main direction of foliation. It is assumed that the interlayering is sedimentary and that the protholith was a quartz + feldspar – rich sediment.

7. Mineral chemistry

This chapter focuses on the mineral chemical data acquired by means of electron microprobe analyses on three metapelitic rocks from the IGB. Details about the methods are given in chapter 5.

Three metapelite samples (Samples C71B, IV26F, IV33; see also chapter 4 on the regional geology and chapter 6 on the petrography) were investigated in more detail because metapelitic rocks are considered being best suitable for further geothermobarometric investigations. Thus, the main focus was to obtain high quality mineral chemical analyses of metamorphic minerals showing extensive solid solutions; i.e., garnet, plagioclase, biotite and muscovite. In addition staurolite, chlorite, amphibole and ilmenite were analysed. Results are listed in Appendices B1 – B3.

Sample C71B

Garnet of this sample is Fe-rich. The FeO contents range from 36.6 to 37.1 wt.%. Values of SiO_2 vary between 35.1 and 36. 7 wt.%, of Al_2O_3 between 20.3 and 21.2 wt. %. MnO, CaO and MgO contents are low; MnO varies between 1.9 and 2.2 wt. %, MgO between 1.8 and 2.2 wt. %, and CaO between 1.5 and 1.8 wt. %, respectively. Calculated garnet end-member compositions are 81.1 to 83.1 mol. % almandine and 8.3 % to 9.3 mol. % pyrope. The spessartine content varies between 4.5 % and 5.0 %. The recalculation of garnet formulae on the basis of 12 oxygens and 8 cations reveals minor Fe^{3+} (below 0.69 mol. %) in the garnet structure. The X_{Mg} of garnet varies between 0.07 and 0.09.

Plagioclase has 56.3 % to 57.5 wt.% SiO_2. Al_2O_3 contents range from 26.2 % to 26.7 wt.%, CaO from 7.1 to 8.6 wt.% and Na_2O from 7.9 to 9.1 wt. %. The X_{An} of plagioclase ranges between 0.3 and 0.4.

Biotite and also muscovite analyses do generally not sum up to totals of 100 wt. % due to the high water content of approximately 4 wt. % that cannot be measured by EMP. SiO_2 in C71B biotites varies between 33.2 % and 33.8 %. FeO contents range from 22.7 % to 23.7 % followed by Al_2O_3 with contents between 19.6 % and 20.0 %. The X_{Mg} of biotite varies between 0.27 and 0.28. The Al contents in the tetrahedral position (Al^{IV}) is around 2.80 mol.

%, the number of Ti cations varies between 0.27 and 0.30 calculated on the basis of 22 O per formula unit (p.f.u)

Muscovites have SiO_2 in the range of 43.9 % to 44.4 %, Al_2O_3 contents between 35.1 % and 35.6% and K_2O contents of 10.6 % to 10.8 %. The X_{Mg} of C71B muscovites ranges between 0.25 and 0.28. Tetrahedral Al^{IV} ranges between 6.1 and 6.2 cations p.f.u.on the basisof 22 O.

Sample IV26F

FeO contents for garnets in sample IV26F vary from 32.8 wt. % to 35.8 wt. %. SiO_2 values lie between 35.3 wt. % and 36.3 wt. %. The third major element in these garnets is Al_2O_3 ranging from 20.2 wt. % to 20.6 wt. %. MnO ranges from 2.7 wt. % to 3.5 wt. %. CaO contents vary from 2.4 wt. % 3.2 wt. %, MgO between 1.3 and 1.7 wt. %. These total oxide composition leads to a calculated end-member composition that is dominated by almandine, which ranges from 76.5 wt. % to 79.0 mol. %. This is followed by pyrope (5.2 to 7.1 mol. %) and spessartine (6.8 to 8.1 mol. %) The grossular end-member varies between 5.3and 7.1 mol. % whereas andradite is occurring in minor amounts (1.9 % to 2.8 mol. %). The recalculation of garnet formulae on the basis of 12 oxygens and 8 cations reveals miner Fe^{3+}, between 0.37 and 0.55 mol. %. The XMg ranges from 0.06 and 0.07.

Plagioclase of sample IV26F has 61.4 to 65.3 wt. % SiO_2, 20.0 to 23.7 wt. % Al_2O_3, followed by Na_2O (10.9 wt. % - 13.4 wt. %) and CaO (1.2 wt. % - 4.4 wt. %). The X_{An} of plagioclase varies between 0.06 and 0.18.

The biotite composition is dominated by SiO_2 ranging from 33.2 wt. % to 34.2 wt. %. FeO ranges from 24.6 wt. % to 26.1 wt. % followed by Al_2O_3 with values between 16.2 wt. % and 17.1 wt. %. K_2O between 9.0 wt. % and 9.8 wt. % is followed by MgO ranging from 5.8 wt. % to 6.8 wt. %. TiO_2 contents are 2.4 wt. % to 2.8 wt. %.The X_{Mg} of biotites is between 0.25 and 0.30. Al in the Tetrahedral position Al^{IV} lies between 13.27 mol. % and 12.81 mol. %. Ti contents range between 1.48 mol. % and 1.58 mol. % calculated on the basis of 22 O per formula unit.

IV26F is the only sample in which amphibole is part of the mineral assemblage. Amphiboles show a variable composition and likely there is more than one type of amphibole present in

this rock. According to their chemical composition the amphiboles studied are classified as ferro-pargasite to ferro-gedrite as well as alumino-tschermakite (following the classification scheme of (Leake *et al.*, 1997)

The variation in amphibole composition is expressed in changes in SiO_2 values ranging between 36.2 wt. % and 40.4 wt. %, and FeO values have a minimum at 21.2 wt. % for ferri-alumino-tschermakite and a maximum of 35.1 wt. % for ferro-gedrite. The minimum Al_2O_3 is 15.3 wt. % and stands for an anlysis of ferro-pargasite, whereas the maximum value of Al_2O_3 is 21.0 wt. % representing a ferro-gedritic amphibole. Except for MgO (0.9 wt. % in ferro-gedrite and 4.4 wt. % in alumino-hornblende) all other oxides are of negligible.

Ilmenite in sample IV26F has 53.8 wt. % to 54.5 wt. % TiO_2 and 45.1 wt. % to 46.1 wt. % FeO.

Sample IV33

Garnets from sample IV33 have SiO_2 contents between 35.0 wt. % and 37.0 wt. %. FeO ranges from 35.8 to 37.3 wt. %. MgO contents are between 2.1 and 2.6 wt. %. Contents are of CaO (1.4 - 1.9 wt. %) and MnO (1.3 to 1.6 wt. %) are low. The calculated end member compositions are 79.7 to 83.1 mol. % almandine, 8.6 to 11.1 mol. % 3.1 to 3.7 mol. % pyrope, 3.1 to 3.7 mol. % spessartine, 1.8 to 4.4 mol. % grossular and 0.3 to 2.5 mol. % andradite. Recalculating the amount of ferric iron from the formulae (on the basis of 12 O and a total of 8 cations) gives 0.29 to 0.59 cations of Fe^{3+}. X_{Mg} of garnets lies between 0.08 and 0.11.

Only 4 measurements of plagioclase are available for this sample. Their SiO_2 values range from 57.6 to 58.3 wt. %. Al_2O_3 lies between 25.5 and 26.0 wt. %. CaO and Na_2O range from 6.8 to 9.1 wt. %. X_{An} ranges from 0.29 to 0.31; hence the plagioclase is classified as an oligoclase.

Biotites from this sample have SiO_2 contents between 33.3 and 34.2 wt. % followed by FeO with contents ranging from 21.4 to 22.5 wt. %. Al_2O_3 values range from 19.5 to 20.1 wt. % and K_2O lies between 9.1 and 9.5 wt. %. The X_{Mg} of biotites lies between 0.28 and 0.30. Tetrahedral positioned Al^{IV} ranges from 13.50 to 14.20 mol. % calculated on the basis of 22 O p.f.u. Ti contents vary between 0.68 and 1.27 mol. %.

Muscovites from the same sample are made up of 43.9 to 44.4 wt. % SiO_2, 34.4 to 35.4 wt. % Al_2O_3 and 9.5 to 10.4 wt. % K_2O. Minor amounts of FeO and Na_2O lie between 1.1 and 2.6 wt. %. The X_{Mg} of IV33 muscovites lies between 0.21 and 0.31. Tetrahedral Al^{IV} has values range from 5.97 to 6.15 mol. %.

Two ilmenite analyses have TiO_2 contents of 52.1 wt. % and FeO contents of 45.5 and 46.1 wt. %.

8. Geothermobarometry

For geothermobarometric calculations EMP – data presented in chapter 7 were used. Calculations were done with the program *Thermocalc 3.26* by Holland and Powell (http://rock.esc.cam.ac.uk/astaff/holland/). Thermocalc uses an internally consistent thermodynamic data set (Holland & Powell, 1998; Powell & Holland, 1988) and hence more consistent P-T estimates are obtained through this approach compared to conventional geothermobarometry which is based on individulal geothermometers and –barometers. This internally consistent data set either uses the same thermodynamic data and activities for all phases involved or has been calibrated against the same set of empirical data. This allows providing an important check whether all phases within a sample are in equilibrium or not. End-members with large systematic errors are easily recognised and can be omitted from calculations.

Activities of mineral end-members of minerals forming solid solutions are necessary as input data for Thermocalc. These have been calculated with the program A-X (Holland and Powell, http://rock.esc.cam.ac.uk/astaff/holland/) from mineral chemical data (chapter 7, Appendix C1 – C3). End-members and activities used for calculating average P and average T are listed in Table 8.1.

Sample C71B

As pointed out in chapter 6 sample C71B is a garnet-biotite-sillimanite schist with the assemblage garnet + biotite + sillimanite + muscovite + quartz + plagioclase. Calculation of P and T for sample C71B is based on the following 7 independent sets of reactions:

1) gr + q + 2sill = 3an
2) 2pa + gr + 3q = 3an + 2ab + $2H_2O$
3) 3east + 6q = phl + 2mu + py
4) 7phl + 12sill = 3east + 4mu + 5py
5) phl + cel + 2sill = 2east + 5q
6) ann + q + 2sill = mu + alm
7) 5phl + 3fcel + 12sill = ann + 7mu + 5py

The calculated average temperature for this sample is 634°C ± 21°C, the average pressure is 5.7 ± 0.9 kbars (Figure 8.1, Table 8.1). The sigfit parameter giving an estimation of the quality of the calculation is 1.40. It should be < 1.49 for 95% confidence.

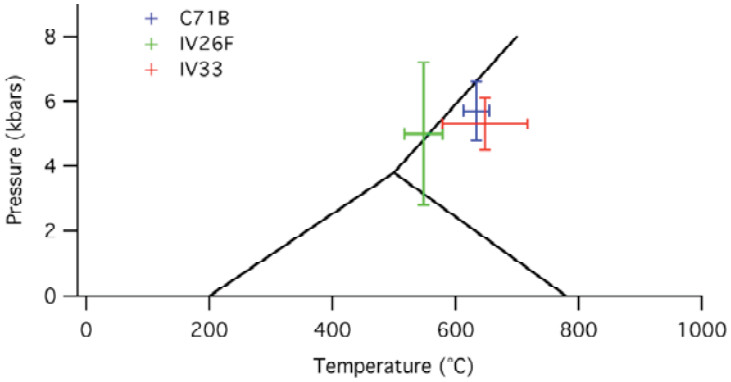

Figure 8.1: Average P-T data for samples C71B, IV26F and IV33; Error bars indicate single standard deviation. The aluminosillicate diagram after Holdaway (1971) is shown for reference.

Sample IV33

Sample IV33 is a garnet-biotite-sillimanite schist (chapter 6). It contains the assemblage garnet + biotite + sillimanite + quartz + plagioclase ± muscovite Thermobarometric results are comparable to those of sample C71B. The P-T calculation is based on 6 independent sets of reactions.

1) gr + q + 2sill = 3an
2) 3east + 6q = phl + 2mu + py
3) 7phl + 12sill = 3east + 4mu + 5py
4) 4phl + 3cel + 12sill = 7mu + 5py
5) ann + q + 2sill = mu + alm
6) 3phl + 3ilm + 4gr + 12sill = 3east + 12an + 3geik + alm

Thermocalc yielded an average tempterature of 648 ± 69 °C at 5.3 ± 0.8 kbar (Figure 8.1; Table 8.1). The sigfit value for this sample is 0.77. For 95 % confidence it should be < 1.54.

Sample IV26F

Sample IV26F has the assemblage amphibole + plagioclase + quartz + garnet + biotite (chapter 6). Calculations for sample IV26F are based on a set of 10 independent reactions:

1) 15ts + 6gr + 22q = 7tr + 34an + 2clin
2) 8ts + 3gr + 11q = 4tr + 17an + ames
3) 3ts + 2py + 4gr + 12q = 3tr + 12an
4) 5ts + 3gr + 11q = 3tr + 13an + $2H_2O$
5) daph + 7gr + 5alm + 19q = 4fact + 13an
6) 6fact + 21an = 11gr + 10alm + 27q + $6H_2O$
7) 3east + py + 2gr + 6q = 3phl + 6an
8) 45ts + 10ann + 18gr + 66q = 21tr + 10phl + 102an + 6daph
9) 71ts + 22ab + 24gr = 17tr + 22parg + 136an + 8clin
10) 2tr + parg + 16an + 2clin + 3alm + 9geik = 11ts + ab + 9ilm

An average temperature of 548 ± 31°C and a pressure of 5.0 ± 2.2 kbar were calculated (Table 8.1, Appendix y). Because of the high uncertainty in the P calculation the sample overlaps all three divariant fields in the aluminosilicate diagram (Figure 8.1). The sigfit factor, which should be below 1.39 for 95% confidence is as high as 3.65 indicating the big uncertainty of this calculation.

The results are slightly different to those of the other two samples discussed in this chapter. Especially uncertainties on pressure are much higher whereas the error estimations for temperature are about the same as for the two other amphibole-free samples. Due to the limited number of samples investigated it remains unclear whether the lower T calculated for sample IV26F is geologically relevant or simply an artefact.

	C71B	IV33	IV26F
Plagioclase			
an	0.561	0.5	0.31
ab	0.662		0.82
Biotite			
phl	0.018	0.0274	0.0169
ann	0.093	0.097	0.13
east	0.027	0.029	0.018
Muscovite			
mu	0.757	0.74	
cel	0.011	0.0116	
fcel	0.029		
pa	0.529		
Garnet			
py	0.001	0.0017	0.00049
gr	0.0002	0.00012	0.00097
alm	0.498	0.54	0.41
Amphibole			
tr			0.0013
fact			0.0262
ts			0.00017
parg			0.00023
Chlorite			
clin			0.0036
daph			0.089
ames			0.0071
Ilmenite			
ilhem		0.97	0.96
geik		0.0023	0.0056
Others			
q	1	1	1
H2O	1	1	1
sill	1	1	
Results			
T (°C)	634	648	548
sd	21	69	31
P (kbar)	5.7	5.3	5.0
sd	0.9	0.8	2.2
Fit	1.4	0.77	3.65
Reactions	7	6	10

Table 8.1: End-member activities and results from *Thermocalc 3.26* calculations. sd single standard deviation.

9. Geochemistry

Geochemical investigations focused on the determination of specific chemical patterns and on the mobility of certain elements during the two major types of calc-silicate alteration, which were distinguished on the basis of field relations and petrography. The first part of this chapter is dealing with calc-silicate alteration in the pillow basalts (Type I calc-silicate rocks), the second one with the tungsten-bearing calc-silicate rocks (Type II calc-silicates rocks). The general approach used was to compare chemical data of altered and unaltered lithologies. For this purpose samples from both the altered as well as the adjacent unalterd rock type (and sometimes transition zone) were taken from different zones at the same outcrop or even the same hand specimen.

Important questions addressed are: (1) Are the two types of calc-silicate alteration comparable with respect to chemical changes and are they genetically related? (2) What are the geochemical fingerprints of calc-silicate alteration related to tungsten mineralisation? (3) To which geological processes are the two alteration types linked?

9.1. Pillow basalts and Type I calc-silicate rocks

As already pointed out by Chadwick (1990), Appel (1994) and more recently by Polat *et al.* (2007) pillow basalts in the Ivisaartoq Greenstone Belt preserve excellent pre-metamorphic zoning. Field relationships and textures of pillow basalts are shown in chapter 4 and their petrography is documented in chapter 6. Commonly greenish calc-silicate-rich inner cores and black rims are distinguished; sometimes a greyish outer core zone containing mm-sized ocelli is also present (Figure 4.3.2)

The rims and the outer core zone are supposed to be the unaltered (or less altered) pillow parts whereas the calc-silicate rich cores seem to have formed through some kind of alteration. Several samples showing a transition from core to rim on the hand specimen scale were taken and analysed separately. In the following results are presented first for the pillow rims and intermediate zones and then for the pillow cores. For two samples the ocelli-rich outer core zone was separately analysed.

9.1.1. Pillow rims

9.1.1.1 Major elements

Data for major elements from XRF analysis are listed in Table 9.1.1. Pillow rims mainly contain SiO_2, CaO, Al_2O_3, and Fe_2O_3 (listed in order of decreasing abundance). The SiO_2 concentrations vary between 48.2 and 57.7 wt. %. CaO concentrations range from 8.6 to 20.0 wt. % those of Al_2O_3 from 13.4 to 19.8 wt. %. Fe_2O_3 concentrations vary between 3.9 and 12.0 wt. %, those of MgO between 1.3 and 9.0 wt.%. Concentrations of Na_2O are highly variable (0.8 to 5.4 wt. %), those of K_2O are negligible. Other major elements show concentrations of less than 1 wt. %. CaO, Fe_2O_3, MnO and MgO show broad negative correlations with SiO_2 (Figure 9.1.1). On the other hand Al_2O_3 correlates with SiO_2 in a positive manner. Na_2O, TiO_2 and P_2O_5 do not show any correlation with SiO_2 at all. LOI varies between 0.32 to 1.51 wt. %.

9.1.1.2. Trace elements

A total number of 21 trace elements excluding REE were measured by ICP-MS. The acquired data are listed in Table 9.1.1 The highest values are shown by Cr, V and Sr that reach up to 610, 301 and 430 ppm, respectively. The other trace elements have lower concentrations. Be, Ta, Th and U for example are always below 1 ppm. Sample C67A-II-R has peculiar high values of Zn (107 ppm) and Cu (335 ppm). This sample also shows the highest Ba, Sr, Nb, Zr and Ga values but has the lowest values of Co and Rb. It also has a different Nb/Ta ratio of 20 in comparison to 12 – 14 to the other samples and a very low Th/U ratio of 0.66. In other samples Th/U is between 3.3 and 4.5. In this study special attention was drawn to W and geochemically related elements like Mo. In most samples concentrations of W and Mo are low. Only in sample C57A-1 a maximum value of 48 ppm W was analysed. Molybdenum values are mostly below the detection limit of 0.5 ppm.

Sample	C42A-K	C57A-2	C57B-K	C67A-II-K	IV35B-K	C42A-R	C57A-1	C57B-R	C67A-II-R	IV35B-R
Type	core	core	core	core	core	rim	rim	rim	rim	rim
SiO_2	48.64	48.08	57.35	55.76	52.26	49.36	57.36	48.20	57.73	54.07
Al_2O_3	13.46	14.01	11.98	20.71	16.23	13.43	14.24	14.22	19.85	18.11
Fe_2O_3	9.60	10.86	7.40	3.88	7.50	8.84	6.23	11.95	3.88	5.77
MnO	0.26	0.25	0.20	0.08	0.18	0.24	0.18	0.23	0.07	0.15
MgO	5.12	8.08	4.36	0.90	2.28	6.09	4.17	8.95	1.78	1.27
CaO	21.12	15.25	16.21	12.93	18.51	19.99	16.15	13.22	8.57	17.28
Na_2O	0.36	1.09	0.62	3.43	0.44	0.67	0.71	1.25	5.35	0.83
K_2O	< 0.05	0.17	< 0.05	0.09	< 0.05	< 0.05	< 0.05	0.23	0.25	< 0.05
TiO_2	0.48	0.55	0.45	1.00	1.01	0.55	0.54	0.58	1.07	0.77
P_2O_5	0.05	0.05	0.05	0.09	0.08	0.05	0.05	0.05	0.06	0.11
LOI	0.82	1.50	1.24	0.87	1.34	0.56	0.32	0.90	0.92	1.51
Total	99.97	99.86	99.91	99.75	99.87	99.83	100.00	99.79	99.52	99.90
Ba	5.0	28	24	34	26	12	35	20	103	18
Be	0.85	0.20	0.79	1.1	0.18	0.76	0.21	0.25	0.55	0.86
Bi	< 1.0	< 1.0	< 1.0	< 1.0	< 1.0	< 1.0	< 1.0	< 1.0	< 1.0	< 1.0
Co	78	33	41	45	62	78	34	73	7	31
Cr	320	374	400	234	158	353	401	610	276	162
Cu	28	43	75	31	19	39	41	36	335	17
Ga	5.9	4.8	6.0	12	9.8	5.5	5.1	6.9	9.5	7.9
Hf	0.98	0.86	0.93	1.8	2.1	1.1	0.99	1.2	1.9	1.4
Mo	< 0.50	0.61	< 0.50	< 0.50	< 0.50	< 0.50	0.82	< 0.50	< 0.50	< 0.50
Nb	1.1	1.1	0.89	2.5	2.8	1.2	1.4	1.3	4.2	1.5
Pb	7.9	6.0	15	5.2	3.6	4.8	6.5	4.3	4.6	8.7
Rb	2.8	2.3	3.9	0.90	3.2	2.2	2.8	3.9	1.8	5.7
Sr	142	105	126	444	99	134	100	58	427	84
Ta	< 0.20	< 0.20	< 0.20	< 0.20	< 0.20	< 0.20	< 0.20	< 0.20	0.21	< 0.20
Th	0.60	0.47	0.71	0.46	0.52	0.79	0.51	0.58	0.39	0.46
U	0.24	0.20	0.23	0.51	0.34	0.21	0.20	0.14	0.53	0.17
V	218	161	176	326	248	220	265	256	285	301
W	< 1.0	37	3.2	2.3	3.1	< 1.0	48	5.5	3.1	10
Y	14	14	12	12	27	14	15	16	13	18
Zn	69	21	63	96	22	85	32	91	107	13
Zr	30	34	32	61	72	34	39	42	67	44
Th/U	3.0	3.3	3.4	0.85	2.0	4.5	3.3	3.5	0.66	4.2
Zr/Hf	31	39	34	34	34	32	39	36	36	31
Nb/Ta	12	12	10	14	18	12	14	12	20	13

Table 9.1.1: Major element (wt. %, XRF analyes) and trace element (ppm, ICP-MS) data of pillow basalt rocks. LOI Loss on ignition.

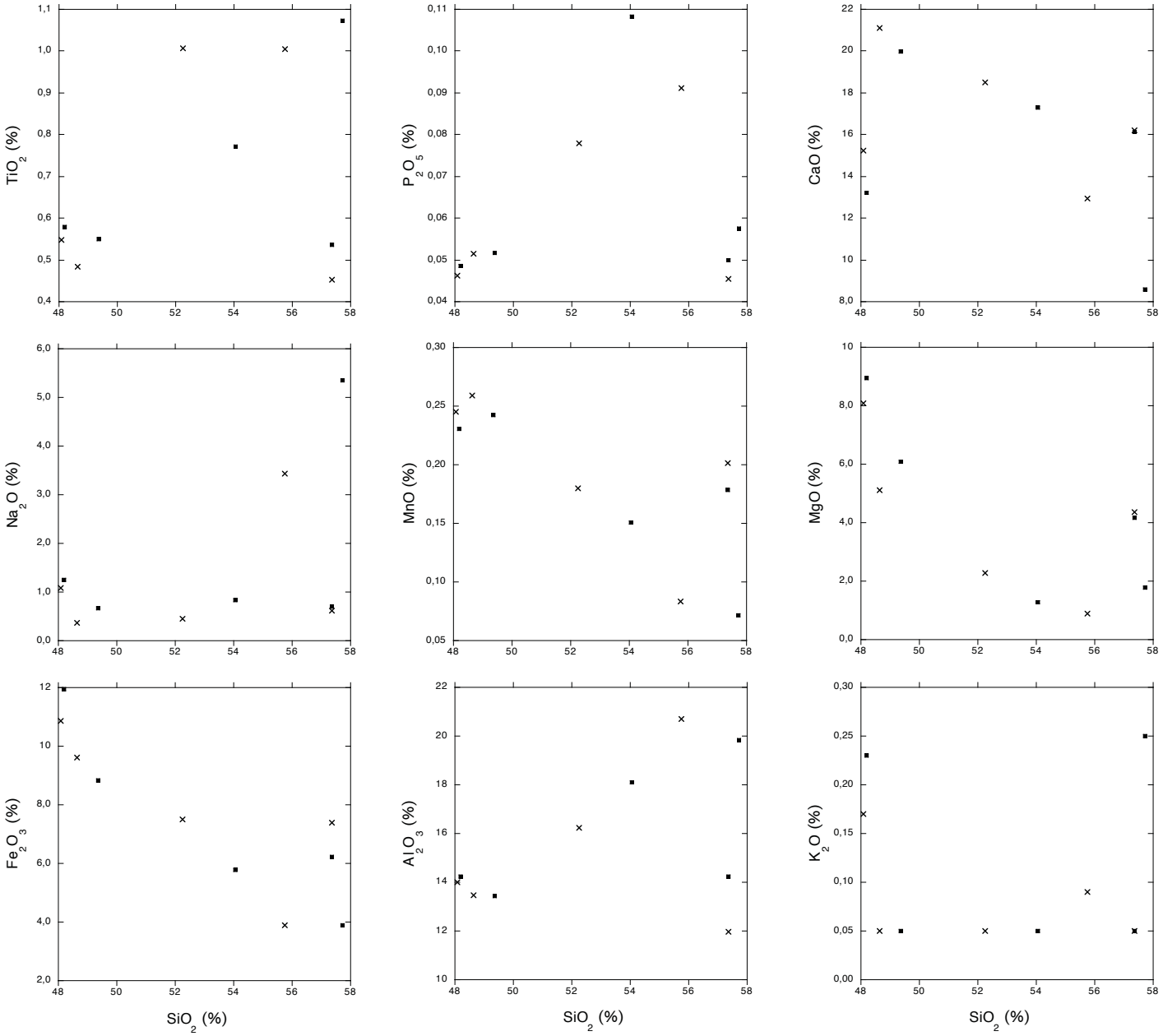

Figure 9.1.1: Plots of SiO_2 versus other major elements.(▪) Pillow basalt rims. (×) Pillow basalt cores.

Sample	C42A-K	C57A-2	C57B-K	C67A-II-K	IV35B-K	C42A-R	C57A-1	C57B-R	C67A-II-R	IV35B-R
Type	core	core	core	core	core	rim	rim	rim	rim	rim
La	2.9	2.8	3.1	4.3	5.6	2.7	3.2	3.1	3.0	4.0
Ce	6.4	6.1	6.4	11	13	6.3	6.8	7.3	8.7	9.5
Pr	0.88	0.84	0.86	1.7	1.9	0.89	0.93	1.0	1.3	1.4
Nd	4.4	4.0	4.0	8.2	10	4.5	4.4	4.8	6.5	7.1
Sm	1.4	1.3	1.2	2.4	3.0	1.4	1.4	1.5	2.0	2.0
Eu	0.50	0.47	0.51	0.88	1.2	0.48	0.51	0.43	0.72	0.68
Gd	2.0	1.7	1.7	2.6	3.9	2.0	1.9	2.1	2.3	2.6
Tb	0.38	0.32	0.31	0.41	0.72	0.39	0.35	0.39	0.39	0.48
Dy	2.5	2.1	2.1	2.5	4.2	2.6	2.3	2.5	2.4	2.9
Ho	0.56	0.45	0.47	0.51	0.88	0.56	0.50	0.56	0.49	0.63
Er	1.7	1.4	1.4	1.5	2.5	1.7	1.5	1.7	1.4	1.9
Tm	0.26	0.20	0.21	0.21	0.36	0.27	0.22	0.25	0.20	0.29
Yb	1.6	1.3	1.4	1.3	2.3	1.7	1.4	1.7	1.3	1.8
Lu	0.26	0.20	0.20	0.18	0.36	0.26	0.22	0.26	0.19	0.29
La/Lu	11	14	15	23	10	10	15	12	16	14
La_N/Lu_N	1.2	1.4	1.5	2.4	1.6	1.5	1.5	1.2	1.6	1.4
Gd/Lu	7.7	8.8	8.0	14	11	7.8	8.8	7.9	12	8.9
Eu/Eu*	0.92	0.95	1.1	1.1	1.1	0.86	0.97	0.75	1.1	0.90

Table. 9.1.2: Rare earth element data of Type I calc-silicate rocks analysed by ICP-MS; values in ppm. La_N, Lu_N = values normalised to chondrite, Eu/Eu* = Eu / √(Sm*Gd).

9.1.1.3. Rare earth elements

REE data are listed in Table 9.1.2 and plotted in relation to chondrite in Figure 9.1.2. In addition, the ratio of REE concentrations of altered to unaltered samples (normalised to 1) is shown in Figure 9.1.3; from the latter any alteration-induced changes in REE concentrations are easily visualised. The REE patterns of pillow basalts are quite flat with a slight enrichment of La and Ce in some samples (La_N/Lu_N varies from 1.2 to 1.5). Most samples show flat MREE to HREE patterns, only samples C67A-II and IV35B show weakly inclined patterns. Most samples also show negative to no Eu anomalies, i.e. (Eu/Eu* = 0.86 to 0.97). Only sample C67A-II-R shows a weak positive Eu anomaly with Eu/Eu* = 1.07.

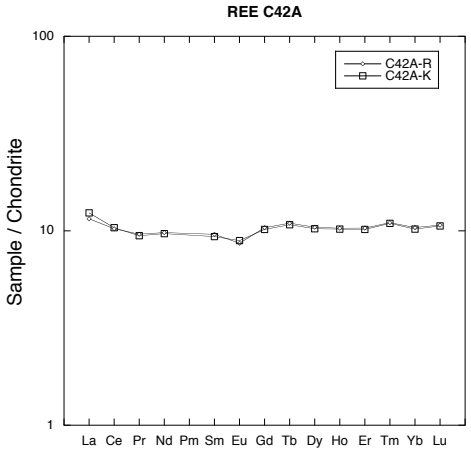
REE C42A
C42A-R
C42A-K
Sample / Chondrite
100
10
1
La Ce Pr Nd Pm Sm Eu Gd Tb Dy Ho Er Tm Yb Lu

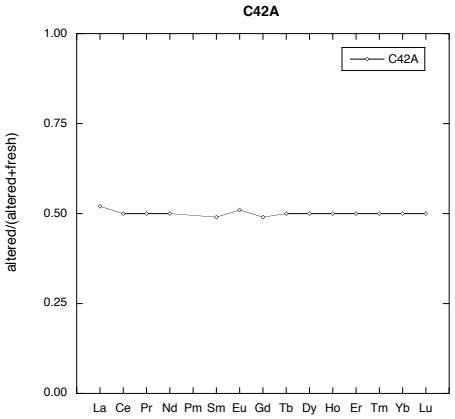
C42A
C42A
altered/(altered+fresh)
1.00
0.75
0.50
0.25
0.00
La Ce Pr Nd Pm Sm Eu Gd Tb Dy Ho Er Tm Yb Lu

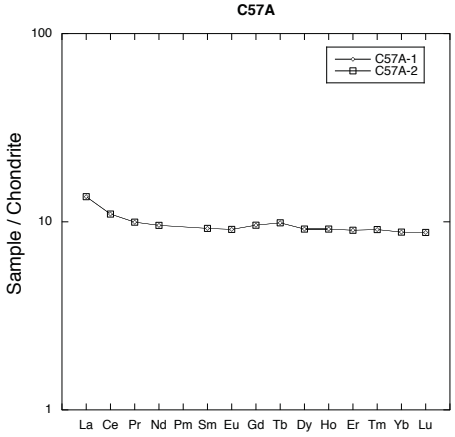
C57A
C57A-1
C57A-2
Sample / Chondrite
100
10
1
La Ce Pr Nd Pm Sm Eu Gd Tb Dy Ho Er Tm Yb Lu

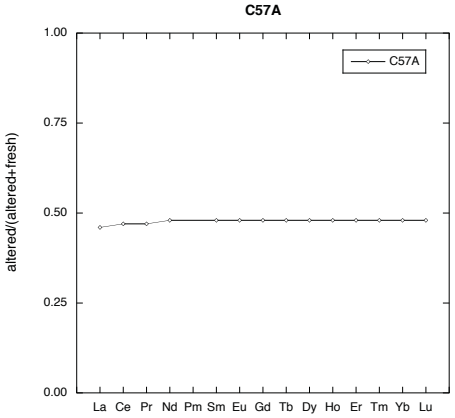
C57A
C57A
altered/(altered+fresh)
1.00
0.75
0.50
0.25
0.00
La Ce Pr Nd Pm Sm Eu Gd Tb Dy Ho Er Tm Yb Lu

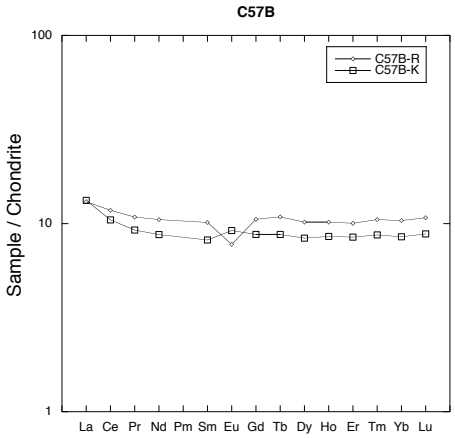
C57B
C57B-R
C57B-K
Sample / Chondrite
100
10
1
La Ce Pr Nd Pm Sm Eu Gd Tb Dy Ho Er Tm Yb Lu

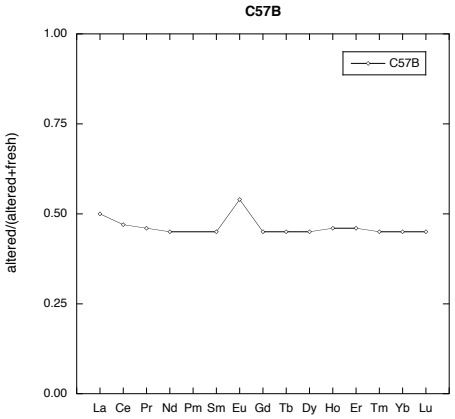
C57B
C57B
altered/(altered+fresh)
1.00
0.75
0.50
0.25
0.00
La Ce Pr Nd Pm Sm Eu Gd Tb Dy Ho Er Tm Yb Lu

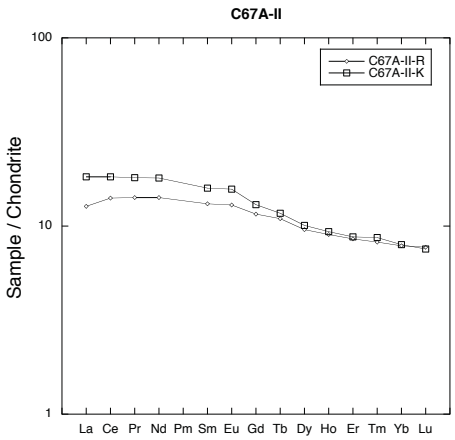
C67A-II
C67A-II-R
C67A-II-K
Sample / Chondrite
100
10
1
La Ce Pr Nd Pm Sm Eu Gd Tb Dy Ho Er Tm Yb Lu

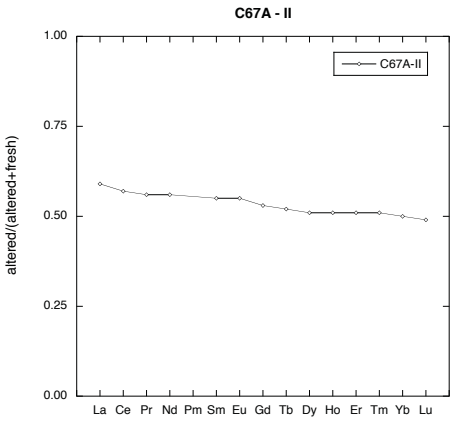
C67A - II
C67A-II
altered/(altered+fresh)
1.00
0.75
0.50
0.25
0.00
La Ce Pr Nd Pm Sm Eu Gd Tb Dy Ho Er Tm Yb Lu

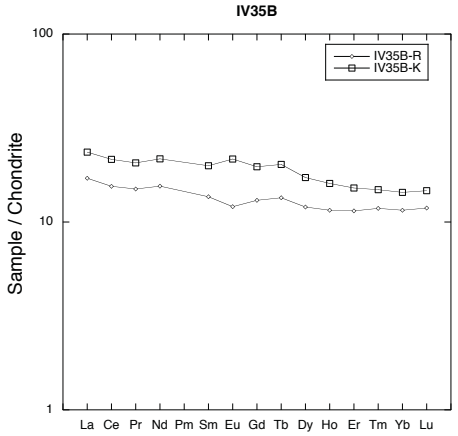

Figure 9.1.2: REE distribution of pillow rims and cores normalised to chondrite; logarithmic scale.

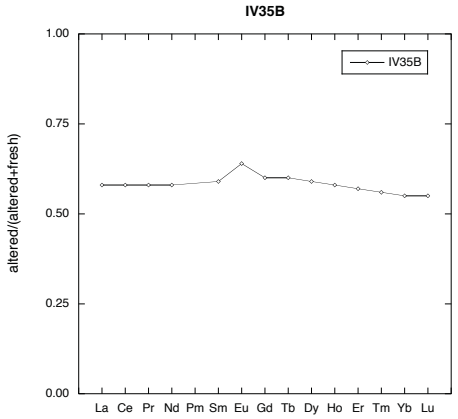

Figure 9.1.3: Comparison of altered and unaltered parts of pillow basalts. Values of 0.5 indicate no change, higher ones enrichment, lower ones depletion during alteration

9.1.2. Pillow basalt cores – calc-silicate rocks Type I

9.1.2.1. Major elements

Major element data are listed in Table 9.1.1. Like in pillow basalt rims SiO_2 has the highest values ranging between 48.0 and 57.4 wt. %. This is followed by CaO values ranging between 12.9 and 21.1 wt. % and by Al_2O_3 between 12.0 and 20.7 wt. %. The abundance of other major elements varies. Fe_2O_3 can reach values up to 10.9 wt. % as in sample C57A-2 and MgO is 8.1 wt % in the same sample. Concentrations of the other major elements are below 1 wt. %.

Major elements from pillow basalt cores show similar correlations like those of the pillow basalt rims (Figure 9.1.1). CaO, Fe_2O_3, MnO and MgO show broad negative correlations with SiO_2, Al_2O_3 a positively one. Na_2O, P_2O_5 and TiO_2 are not correlated with SiO_2. LOI varies between 0.82 to 1.50 wt. %.

9.1.2.2. Trace elements

Trace element data are listed in Table 9.1.1. Sr ranges from 98 to 444 ppm, Cr from 158 to 400 ppm and V from 161 to 326 ppm. Other trace element concentrations are below 100 ppm.

W values range from 1 up to 37 ppm in sample C57A-2, which is slightly lower than in corresponding pillow rims. Molybdenum concentrations are between < 0.5 and 0.61 ppm. Th/U ratios generally range from 2.0 to 3.4. Only sample C67A-II-K has a ratio of 0.85.

9.1.2.3. Rare earth elements

Data for REE gathered by ICP-MS are listed in Table 9.1.2. As seen from Figure 9.1.2 the five samples investigated show some variable REE patterns. Three samples can be grouped together but two show completely different patterns. Similarly to pillow basalt rims HREE are slightly depleted in comparison to LREE with La_N/Lu_N varying between 1.2 and 2.4. Eu/Eu* lie between 0.92 and 1.09 and hence are slightly negative or positive with no systematic trend. The most outstanding sample is C67A-II-K, which is far noticeably stronger enriched in LREE with La/Lu = 2.3. However this sample cannot really be distinguished by its Eu anomaly with Eu/Eu* = 1.1.

9.2. Calc-silicate rocks of Type II and their host rocks

Rocks dealt within this chapter are subdivided into two or three different subgroups, respectively. We distinguish between fresh unaltered and altered rocks. Sometimes a third transitional type was distinguished and analysed separately.

9.2.1. Host rocks not affected by calc-silicate alteration

9.2.1.1. Major elements

Concentrations of SiO_2 of unaltered rocks range between 48.2 and 64.4 wt. % (Table. 9.2.1) Al_2O_3 contents vary from 11.4 to 17.5 wt. %. Fe_2O_3, CaO and MgO vary considerably. Fe_2O_3 varies between 5.9 and 12.2 wt. %, CaO between 4.9 and 12.3 wt. % and MgO between 2.9 and 7.8 wt. %. Na_2O is between 2.4 and 2.5 wt. % but in one sample, C73A-R, has a maximum concentration of 5.2 wt. %. Other major elements and LOI are below 1 wt. %.

Fe_2O_3 shows a negative correlation with SiO_2 (Figure. 9.2.1), as do MgO, CaO and MnO. P_2O_5 and Na_2O show a positive correlation with SiO_2. TiO_2, K_2O and Al_2O_3 do not show any obvious correlation with SiO_2.

9.2.1.2. Trace elements

Trace element data gathered by ICP-MS are listed in Table 9.2.1. Barium shows a considerable variation, i.e. from 33 up to 2038 ppm. Strontium varies between 137 to 420 ppm and V ranges from 55 to 247 ppm. Tungsten mostly lies below the detection limit of 1 ppm but has a value of 8 ppm in sample IV10C-2. Molybdenum generally lies below the detection limit of 0.5 ppm.

Sample	C55A-1-R	C73A-R	IV10C-2	IV20B-1	C55A-1-K	C73A-K	IV10C-1	IV20B-2	C55A-1-M	C73A-M
Type	unaltered	unaltered	unaltered	unaltered	altered	altered	altered	altered	transition	transition
SiO_2	48.43	59.67	48.24	64.43	44.80	62.95	47.99	52.50	47.87	61.22
Al_2O_3	14.89	17.50	15.04	11.40	13.11	13.38	5.49	3.85	10.35	14.63
Fe_2O_3	11.91	5.90	12.18	5.85	7.65	5.02	13.58	12.25	10.14	5.15
MnO	0.22	0.06	0.21	0.12	0.48	0.09	0.34	0.25	0.44	0.08
MgO	7.78	2.88	7.44	3.60	3.02	1.46	6.67	7.44	7.09	2.88
CaO	12.32	4.86	11.18	9.43	28.43	15.15	24.10	22.15	22.20	11.21
Na_2O	2.40	5.17	2.54	2.42	0.03	0.27	0.11	0.19	0.81	2.21
K_2O	0.37	1.55	0.92	1.26	0.05	0.03	0.01	0.03	0.06	0.11
TiO_2	0.77	1.18	0.91	0.61	0.41	0.55	1.51	1.28	0.74	1.20
P_2O_5	0.07	0.12	0.08	0.15	0.05	0.07	0.13	0.12	0.06	0.10
LOI	0.56	1.00	0.66	0.38	1.43	1.11	-0.07	0.11	0.77	0.97
Total	99.72	99.89	99.41	99.65	99.45	100.08	99.84	100.17	100.53	99.77
Ba	33	730	841	2038	5.0	8.0	122	231	5.0	54
Be	0.88	1.1	1.3	4.0	2.5	7.0	4.1	4.4	6.8	4.7
Bi	< 1.0	< 1.0	< 1.0	< 1.0	< 1.0	< 1.0	< 1.0	6.0	< 1.0	< 1.0
Co	48	40	39	27	23	35	63	98	47	42
Cr	134	170	192	102	52	95	389	485	120	175
Cu	46	99	42	262	7.6	12	22	27	12	23
Ga	6.0	16	16	33	7.5	14	7.1	7.1	5.0	7.7
Hf	1.4	2.8	1.6	3.8	0.70	1.2	2.5	8.1	1.1	2.8
Mo	< 0.50	< 0.50	< 0.50	< 0.50	31	< 0.50	0.94	< 0.50	< 0.50	< 0.50
Nb	1.6	2.5	2.2	6.7	9.6	4.1	29	42	9.1	3.7
Pb	2.9	5.6	9.9	10	1.6	2.2	43	6.5	2.3	5.3
Rb	9.7	128	78	120	0.83	2.6	2.8	4.3	2.6	5.7
Sr	137	250	420	287	44	149	194	140	76	222
Ta	< 0.20	< 0.20	< 0.20	0.42	0.38	< 0.20	1.4	2.9	0.29	< 0.20
Th	0.34	1.6	0.29	4.7	0.10	0.59	2.1	12	0.23	1.3
U	0.19	0.29	0.19	1.9	0.67	0.36	1.2	3.2	0.55	0.31
V	247	128	232	55	179	146	181	89	149	86
W	< 1.0	< 1.0	8.0	< 1.0	586	2.2	19	122	13	1.8
Y	16	19	24	14	31	12	34	94	20	19
Zn	111	107	116	84	104	97	149	163	175	125
Zr	41	93	52	184	21	36	92	473	32	87
Th/U	2.1	4.9	2.2	2.5	0.14	1.5	1.8	3.5	0.43	3.6
Zr/Hf	30	34	33	49	30	30	38	58	29	31
Nb/Ta	12	14	18	16	25	44	21	14	32	18

Table 9.2.1: Major element (wt. %, XRF analyes) and trace element (ppm, ICP-MS) data of Type II calc-silicate rocks and their unaltered host rocks. LOI Loss on ignition.

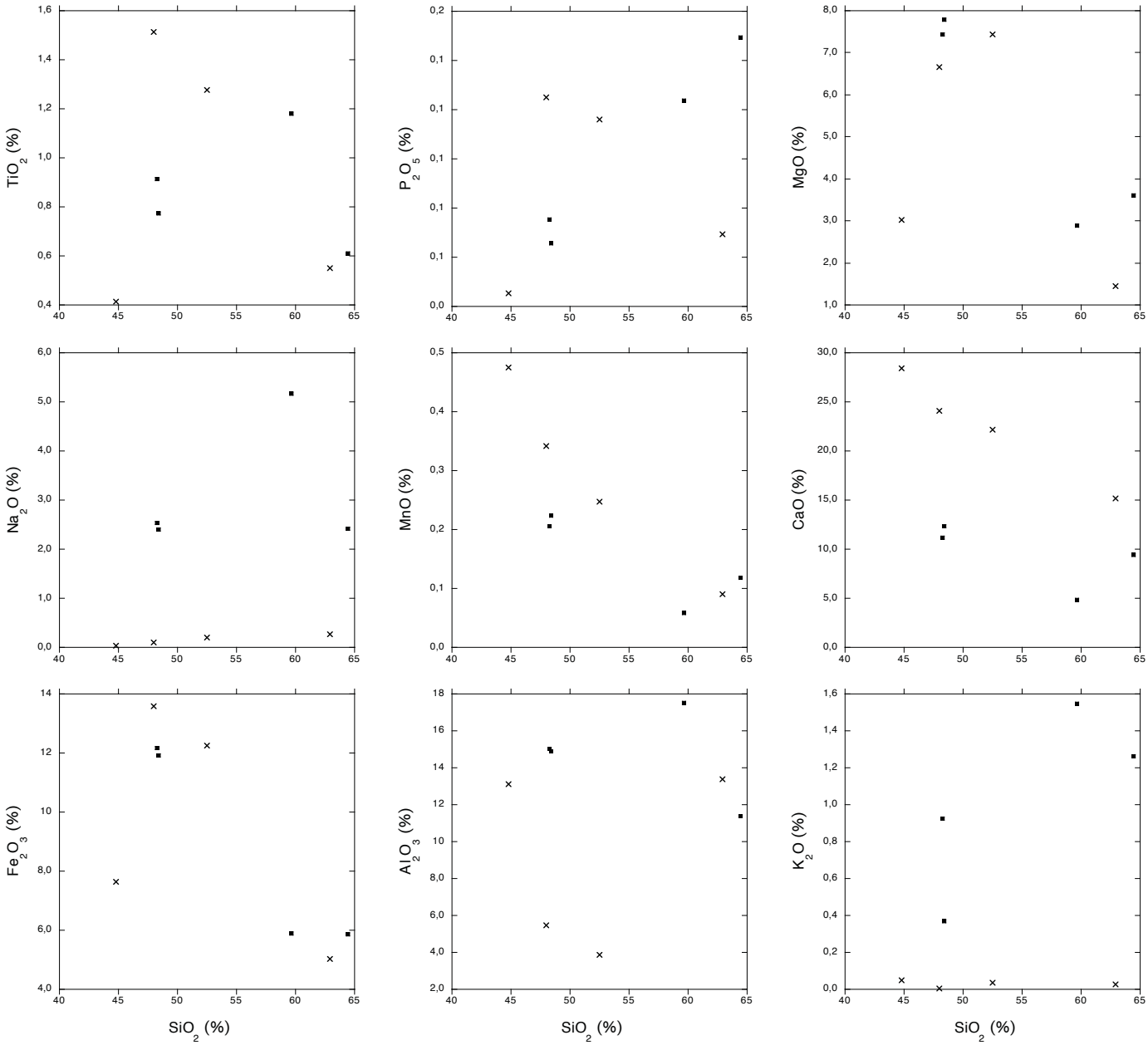

Figure 9.2.1: Plots of SiO_2 versus other major elements.(▪) Unaltered host rocks. (×) Type II calc-silicate rocks.

Sample	C55A-1-R	C73A-R	IV10C-2	IV20B-1	C55A-1-K	C73A-K	IV10C-1	IV20B-2	C55A-1-M	C73A-M
Type	unaltered	unaltered	unaltered	unaltered	altered	altered	altered	altered	transition	transition
La	2.7	8.6	3.0	15	1.7	20	67	67	2.8	11
Ce	7.0	24	7.5	31	3.7	31	130	132	6.3	30
Pr	1.1	3.5	1.2	3.5	0.51	3.7	15	15	0.97	4.2
Nd	5.9	16	6.4	13	4.2	14	62	59	5.3	19
Sm	1.9	3.9	2.1	2.6	1.8	2.8	11	11	1.8	4.5
Eu	0.67	1.2	0.86	0.91	0.70	1.1	2.7	2.0	0.63	1.2
Gd	2.7	4.1	3.1	2.3	3.2	2.8	8.5	9.7	2.7	4.6
Tb	0.49	0.66	0.59	0.34	0.64	0.41	1.2	1.6	0.50	0.73
Dy	3.2	3.9	3.7	2.0	4.7	2.3	5.6	10	3.4	4.2
Ho	0.69	0.79	0.79	0.40	1.3	0.45	0.97	2.2	0.78	0.85
Er	2.1	2.2	2.4	1.2	3.8	1.2	2.5	6.9	2.4	2.4
Tm	0.32	0.32	0.35	0.17	0.63	0.16	0.32	1.1	0.40	0.33
Yb	2.0	1.9	2.2	1.1	4.0	0.99	1.9	6.5	2.4	2.0
Lu	0.31	0.29	0.35	0.16	0.68	0.15	0.29	0.99	0.39	0.30
La/Lu	8.6	29	8.6	96	2.5	131	234	67	7.1	36
La_N/Lu_N	0.89	3.0	0.89	10	0.26	14	24	7.0	0.73	3.8
Gd/Lu	8.4	14	8.9	14	4.7	19	30	9.8	6.8	15
Eu/Eu*	0.90	0.94	1.0	1.2	0.88	1.2	0.85	0.59	0.88	0.80

Table 9.2.2: REE concentrations (in ppm) and selected ratios of Type II calc-silicate rocks and their unaltered host rocks.

9.2.1.3. Rare earth elements

Data for REE are listed in Table 9.2.2. Unaltered host rocks do not show uniform REE patterns. Patterns of samples C55A-1-R and IV10C-2 are very similar. Both have flat patterns with weak depletion in LREE with $La_N/Lu_N = 0.89$ (Figure 9.2.2). These are similar to those documented for the pillow basalts. One sample (IV10C-2) has a slightly positive Eu anomaly (Eu/Eu* = 1.0) the other one (C55A-1-R) a weakly negative one (Eu/Eu* = 0.9). In contrast sample IV20B-1 is strongly enriched in LREE and has rather low concentrations of HREE represented by $La_N/Lu_N = 10$. It also shows a marked positive Eu anomaly with Eu/Eu* = 1.2. Sample C73A-R is also enriched in LREE ($La_N/Lu_N = 3.0$) although La shows a light depletion relative to Ce. However HREE are depleted within this sample and it has a weak negative Eu anomaly. These two later samples represent different host rocks that are more fractionated (e.g. intermidiate igneous rocks like andesites or dacites)

9.2.2. Calc-silicate rocks of Type II

9.2.2.1. Major elements

XRF data of major elements are listed in Table 9.2.1. The most abundant element is SiO_2 with concentrations between 44.8 and 63.0 wt. %. CaO ranges between 15.2 and 28.4 wt. %. Al_2O_3 varies between 3.9 and 13.4 wt. %, Fe_2O_3 between 5.0 and 13.6 wt. %. Except MgO, which can reach up to 7.4 wt. % in sample IV20B-2, concentrations of all other major elements are below 1 wt. %. Sample IV10C-1 stands out with a negative LOI what means that it has gained weight during heating due to the oxidation of FeO to heavier Fe_2O_3.

Correlations of major elements with SiO_2 are similar to those reported for unaltered host rocks of Type 2 calc-silicate rocks (Figure 9.2.1). Fe_2O_3, CaO and MnO show a clear negative correlation with SiO_2. However, the contents of alkalis (Na_2O, K_2O) are very low. As the other major elements (TiO_2, Al_2O_3, MgO) they are not to poorly correlated with SiO_2.

9.2.2.2. Trace elements

As to be seen from Table 9.2.1 concentrations of most trace elements show considerable variation. For example Zr contents range from 21 to 473 ppm. A similar behaviour is seen for Cr and Ba, which are high in sample IV20B-2 (Cr = 485 ppm; Ba = 231 ppm) but much lower in sample C55A-1-K (Cr = 52 ppm; Ba = 5.0 ppm). Sample C55A-1-K contains 586 ppm W. Also sample IV20B-2 is enriched in W with a value of 122 ppm. Molybdenum is slightly enriched in sample C55A-1-K with a value of 31 ppm. Compared to the other three samples of this set C55A1-K can also be distinguished by very low Th/U = 0.14 compared to 1.5 to 3.5 in other samples Sample IV20B-2 is chemically unusual. On one hand it has the highest concentrations of siderophile elements (e.g. Cr, Co) indicating a more mafic protolith on the other hand it has the highest concentrations of lithophile elements (Rb,Ba, Ta, Nb, Zr, Hf, Y) of all Type II calc-silicate rocks analysed.

9.2.2.3. Rare earth elements

Rare earth element data are listed in Table 9.2.2. As shown in Figure 9.2.2 Type II calc-silicate rocks show very different patterns. Two general trends can be observed. Samples C73A-K, IV10C-1 and IV20B-2 all show enrichment in LREE and depletion in HREE with La_N/Lu_N varying between 7.0 for IV20B-2 and 24 for IV10C-1. Except C73A-K they show negative Eu anomalies with Eu/Eu* between 0.59 and 0.85. C73A-K has a positive Eu anomaly with Eu/Eu* of 1.2. This sample furthermore has a much higher Nb/Ta ratio of 44 in comparison to 14 and 21 in the other two samples. Sample C55A1-K is completely different to those three samples by showing extreme depletion in LREE and enrichment in HREE represented by $La_N/Lu_N = 0.26$. This sample has, however a negative Eu anomaly with Eu/Eu* = 0.88 and low Gd/Lu of 4.7 compared to 9.8 to 30.

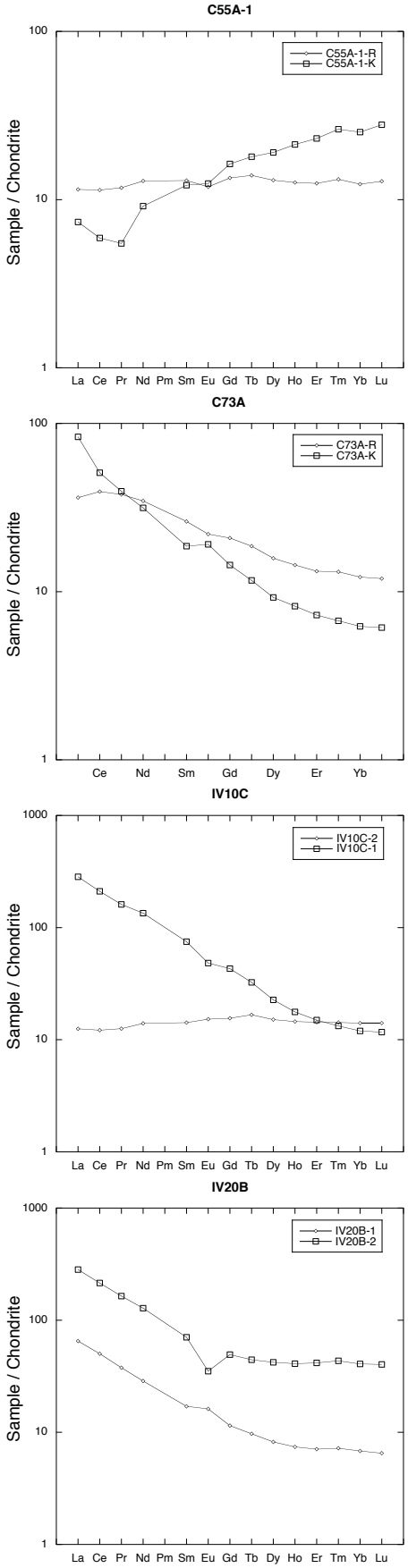

Figure 9.2.2: REE distribution of Type 2calc-silicate rocks and their unaltered host-rocks normalised to chondrite; logarithmic scale.

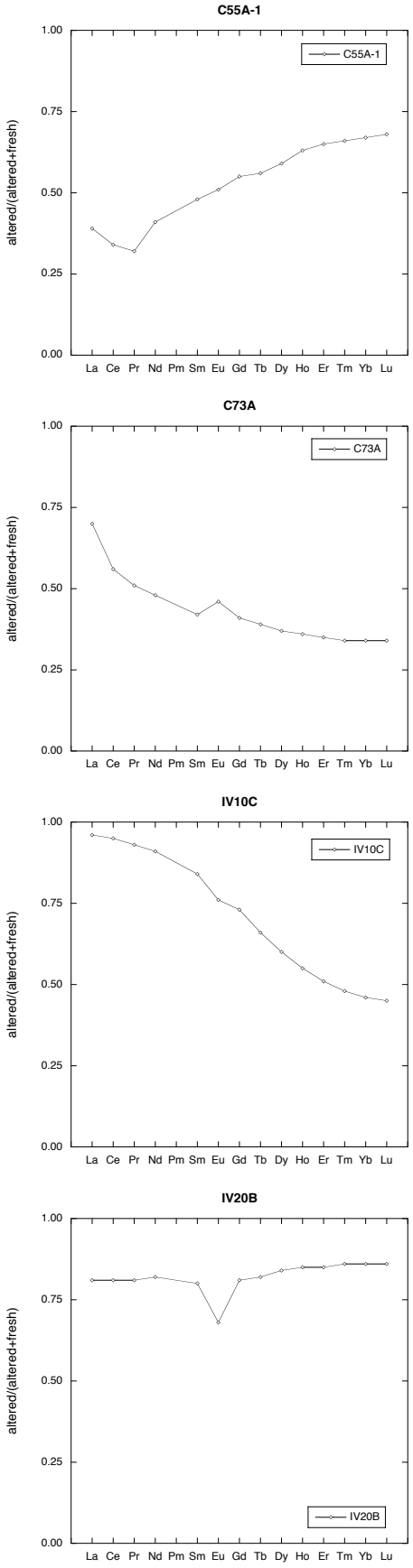

Figure 9.2.3: REE ratio of altered to unaltered samples (normalised to 1)

9.2.3. Transition type rocks

At two localities samples (C55A-1-M, C73A-M) of a transitional zone between the unaltered host rock and the intensely altered calc-silicate rocks were sampled and analysed.

9.2.3.1. Major elements

Major element data are listed in Table 9.2.1. The two samples have 47.9 and 61.2 wt. % SiO_2, respectively. Other elements with considerable variations include Al_2O_3 (10.3 and 14.6 wt %), Fe_2O_3 (5.2 and 10.1 wt. %) and CaO (11.2 and 22.2 wt %). Other elements like MgO (2.9 and 7.1 wt. %) are less abundant.

9.2.3.2. Trace elements

Chromium (120 – 175 ppm), V (86 – 1499 ppm), Sr (76 – 222 ppm) and Zn (125 – 175 ppm) are the most abundant trace elements (Table 9.2.1). Zirconium has a maximum value of 87 ppm. Tungsten contents in this transition zone are not very high. Values of 1.8 ppm respectively 13 ppm were measured. The two samples also vary in other parameters like Th/U which is 0.43 in C55A-1-M and 3.6 in C73A-M

9.2.3.3. Rare earth elements

Rare earth element data are listed in Table 9.2.2. As shown in Figure 9.2.4. the patterns of the two samples are quite different. C73A-M is enriched in LREE and depleted in HREE shown by $La_N/Lu_N = 3.8$. It shows a negative Eu anomaly with Eu/Eu* = 0.8. Contrariwise C55A-1-M shows nearly flat chondrite normalised REE patterns ($La_N/Lu_N = 0.73$). This sample also shows a negative Eu anomaly (Eu/Eu* = 0.88). The Gd/Lu ratio of C73A-M is 15; i.e. compared to 6.8 in sample C55A-1-M (Figure 9.2.4).

Sample	2T16-17	2T19	C51B-1	C51BIV	IV5/2	IV5/4
SiO_2	43.46	45.89	40.89	44.93	42.30	41.71
Al_2O_3	5.18	11.33	7.94	11.12	11.43	11.97
Fe_2O_3	13.25	10.51	12.50	10.31	9.88	10.03
MnO	0.29	0.36	0.24	0.35	0.33	0.30
MgO	6.06	5.86	4.71	5.77	3.01	3.30
CaO	26.55	23.76	24.73	23.29	28.26	27.85
Na_2O	0.11	0.41	0.08	0.39	0.05	0.08
K_2O	< 0.05	< 0.05	< 0.05	< 0.05	< 0.05	< 0.05
TiO_2	1.10	0.74	0.82	0.72	1.39	1.41
P_2O_5	0.11	0.08	0.10	0.07	0.12	0.12
LOI	1.16	1.19	2.57	3.06	2.07	1.98
Total	97.28	100.13	94.58	100.01	98.84	98.74
Ba	< 5.0	< 5.0	17	8.1	< 5.0	< 5.0
Be	0.49	3.4	7.2	7.0	8.7	6.6
Bi	< 1.0	< 1.0	21	< 1.0	11	19
Co	24	38	85	97	63	66
Cr	11	201	708	921	677	683
Cu	8.1	11	42	42	4.7	8.3
Ga	9.7	6.3	9.8	6.7	11	12
Hf	1.5	1.4	1.4	1.6	2.4	2.6
Mo	25	0.73	122	60	49	38
Nb	3.4	2.9	29	18	32	33
Pb	9.3	6.8	10	5.5	4.0	5.3
Rb	1.6	0.54	0.98	0.87	0.42	0.78
Sr	325	190	1567	1072	107	174
Ta	0.29	< 0.20	3.6	2.2	1.6	1.8
Th	0.66	0.47	1.3	1.8	2.5	2.6
U	0.24	0.22	0.66	0.50	1.9	2.1
V	282	216	133	135	220	210
W	1560	56	12064	8386	1648	1295
Y	12	28	13	9.7	23	25
Zn	48	117	110	115	108	122
Zr	44	48	65	62	119	110
Th/U	2.9	2.4	2.0	3.4	1.34	1.3
Zr/Hf	29	34	46	39	50	43
Nb/Ta	12	18	8.2	8.2	20	19

Table 9.3.1: Major element (wt. %, XRF analyes) and trace element (ppm, ICP-MS) data of tungsten-enriched rocks. LOI Loss on ignition.

Sample	2T16-17	2T19	C51B-1	C51BIV	IV5/2	IV5/4
La	7.9	5.2	18	22	31	31
Ce	17	12	38	46	64	64
Pr	2.3	1.7	4.7	5.8	7.6	7.8
Nd	10.3	8.2	19	23	30	31
Sm	2.6	2.6	3.6	4.2	5.9	6.3
Eu	1.3	0.81	1.1	1.1	1.7	1.8
Gd	2.9	3.5	3.1	3.4	4.7	5.3
Tb	0.44	0.63	0.42	0.45	0.62	0.71
Dy	2.7	4.3	2.3	2.4	3.3	3.8
Ho	0.51	0.96	0.39	0.43	0.57	0.64
Er	1.4	3.0	1.0	1.1	1.5	1.8
Tm	0.19	0.47	0.13	0.16	0.20	0.25
Yb	1.1	3.1	0.76	0.92	1.2	1.5
Lu	0.17	0.49	0.11	0.14	0.16	0.22
La/Lu	47	11	164	156	190	137
La_N/Lu_N	4.8	1.1	17	16	20	14
Gd/Lu	17	7.1	28	24	29	24
Eu/Eu*	1.4	0.82	1.0	0.92	0.98	0.97

Table 9.3.2: REE data (ppm) of tungsten rich samples.

9.3 Tungsten enriched calc-silicate rocks

Calc-silicate rocks enriched in scheelite were also sampled using UV lamping. The results are presented in this chapter. From field relations and petrography these rocks can be assigned to the Type II calc-silicate rocks.

9.3.1 Major elements

Results from major element analyses are listed in Table 9.3.1. Samples have SiO_2 concentrations between 40.9 and 45.9 wt. %. CaO concentrations vary between 23.3 and 28.3 wt. % and those of Al_2O_3 are between 5.2 and 12.0 wt. %. Fe_2O_3 varies from 9.9 to 13.3 wt. %, MgO from 3.0 to 6.1 wt. %. The concentrations of alkalis are very low; Na_2O ranges between 0.05 to 0.4 wt. %, K_2O is always below the detection limit.

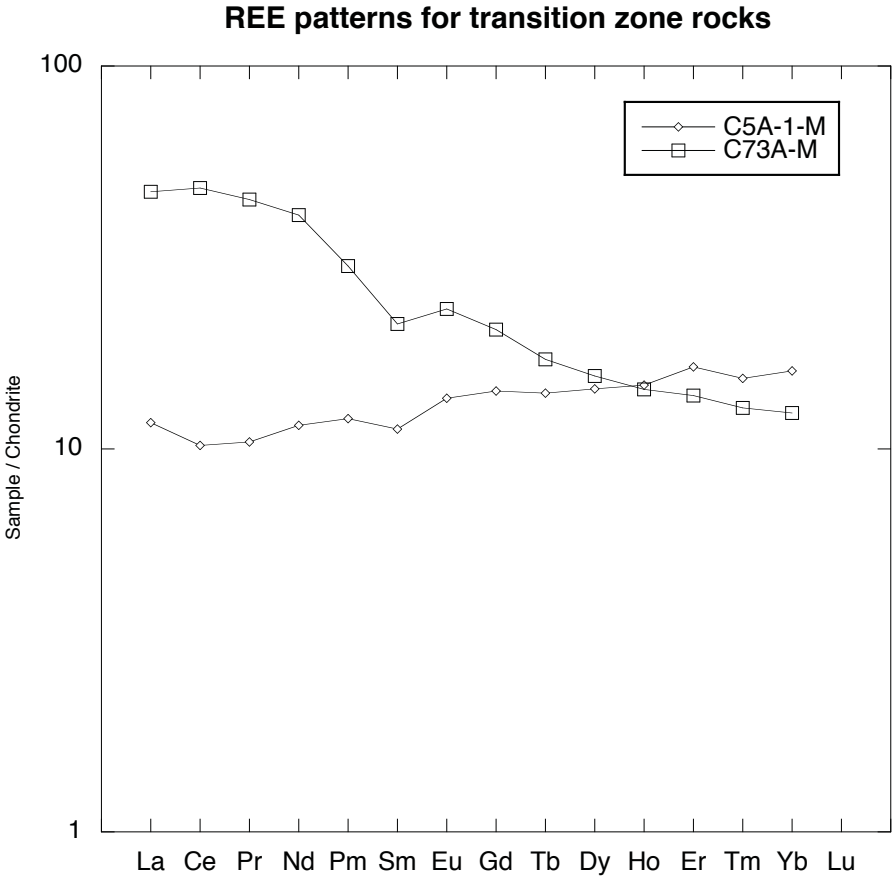

Figure 9.2.4: REE distribution of transition zone rocks normalised to chondrite; logarithmic scale

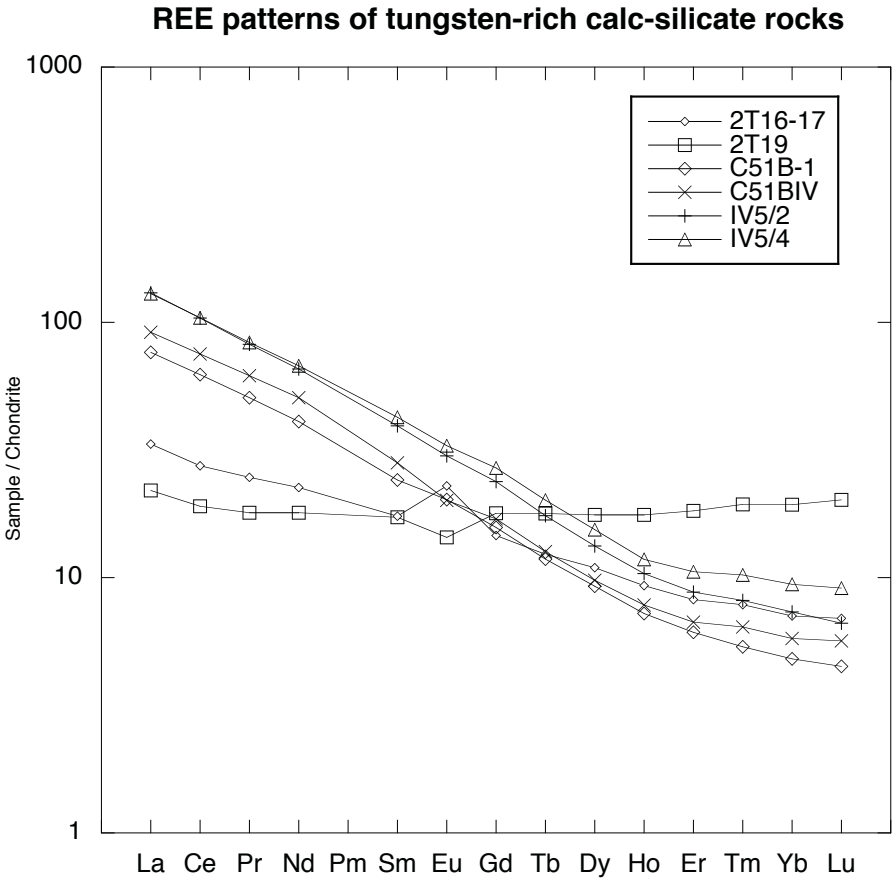

Figure 9.2.5: REE distribution of rocks with high tungsten content normalised to chondrite; logarithmic scale

9.3.2. Trace elements

Some of the trace elements in these tungsten-enriched rocks show higher values than in other rocks of Type II. Sample C51B-1 for example has a Sr content of 1567 ppm. Sr generally varies from 107 ppm to this maximum value in this kind of rocks (Table 9.3.1). Chromium concentration is as high as 921 ppm in C51BIV. Otherwise the minimum Cr value is only 11 ppm in sample 2T16-17. Vanadium values range from 133 to 281 ppm. All these samples show a generally high content in tungsten. The maximum value is 12064 ppm of sample C51B-1. 8386 ppm in sample C51BIV comes in second place. Other values range between 1295 and 1648 ppm. The minimum tungsten content in this series of samples is 56 ppm (sample 2T19). Mo has a minimum value of 0.73 ppm in sample 2T19 but can reach up to 122 ppm in sample C551B-1, which is also the sample with the highest W content.

.

9.3.3. Rare earth elements

Data for REE are listed in Table 9.3.3. Chondrite normalised patterns show a very clear trend although two samples do not fit to this general trend. Most samples are clearly enriched in LREE and depleted in HREE (Figure 9.2.5) having a La_N/Lu_N ratio between 1.1 and 20. They show a weakly negative to no Eu anomalies. Eu/Eu* = 0.92 to 1.0. REE patterns for samples 2T16-17 and 2T19 are exceptional. The pattern of 2T16-17 is flatter than that of other rocks. Thus, enrichment of LREE did not happen to the same extent, which is shown by La_N/Lu_N = 4.8 in comparison to much higher values from the other samples. This sample is also characterised by a positive Eu anomaly which is lacking in all other samples. The REE pattern of sample 2T19 is totally flat. LREE are only slightly enriched (La_N/Lu_N = 1.1). A strong negative Eu anomaly (Eu/Eu* = 0.82) is peculiar

9.4. Chemical characteristics of calc-silicate alterations

9.4.1. Isocon calculations

Calc-silicate alteration of pillow basalts (Type I) and formation of massive calc-silicate rocks (Type II), the latter associated with scheelite mineralisation are the two main alteration types in the IGB. The chemical changes of these alterations and the mobility of certain elements during these two alteration events are to be investigated in the following chapter using the data presented in chapters 9.1 to 9.4. For this purpose fresh and altered samples of each alteration type are to be compared with each other. A very good way of showing which elements are mobile during alteration is to draw Iscon-diagrams based on Gresens equation (Grant, 1986). The calculations were done with the programme ISOCON created by Jean-Luc Potdevin and using the approach of (Baumgartner & Olsen, 1995).

9.4.1.1. Calc-silicate alteration (Type I) of pillow basalts

Five samples (C42A, C67A, C57A, C57B and IV35B) have been selected. Pillow basalts having altered cores containing Type I calc-silicate assemblages were compared to calc-silicate-free pillow rims. Results are shown graphically in Figures 9.4.1 to 9.4.5. It is important to notice that calculations for samples C57B and IV35B yielded lower quality results, which should be treated with caution. For these two samples it was difficult to define element associations unaffected by alteration; this is indicated by slope values for the isocon significantly < 1 in the figures.

Aluminium is regarded as stable during this kind of alteration and in all calculations it was treated as immobile and (together with other immobile trace elements) was used for calculating the isocons. Most major elements do not show a systematic trend on the isocon plots. Silicium is unaffected to slightly depleted in the altered cores. Only in sample C57B it is significantly enriched. This can probably be explained by inaccurate sampling. As shown in Figure 4.3.4 the inner pillow core of this sample contains a quartz vein. The pillow core sample could therefore be contaminated with this quartz-rich material. This fact could also weaken the proportion of other elements in this sample pair. Ca is not enriched to

significantly enriched in the five studied sample pairs, and also Fe and Mg show inconsistent trends. The loss on ignition (LOI) shows no enrichment in the altered cores for two sample pairs but is very strongly enriched or depelted in others.

Large ion lithophile elements (LIL) like Na, Pb, Sr, K and Rb must be regarded as mobile although they do not define totally consistent trends. Sodium is depleted in all samples except C57A; Ba for example is depleted in all samples except C57B and IV35B. K, Rb and Pb show enrichment in some and depletion in other samples. Sr is the only element of this group that shows a comparable trend in all five pairs of samples although the observed enrichment varies from very strong (sample C57B) to nearly not existing (sample C67A).

High field strength elements (HFSE) are broadly scattered throughout the five studied sample pairs. Tantalum, Zr and Hf have no tendency in any direction. Similarly, Nb can be either depleted or enriched. In most altered samples U is slightly enriched. Titanium is generally depleted except in sample IV35, which was already highlighted as to be handled with care.

The two transition elements Zn and Cr follow a distinct trend. Both are depleted throughout the entire series of samples (except IV35B). Copper seems to be mobile, it shows considerable depletion (C42A, C67-II) or enrichment (C57B, IV35B).

Tungsten, which is of special interest in the context of this thesis, shows depletion in the cores of all four sample pairs for which the W concentrations were above the detection limit compared to the rims

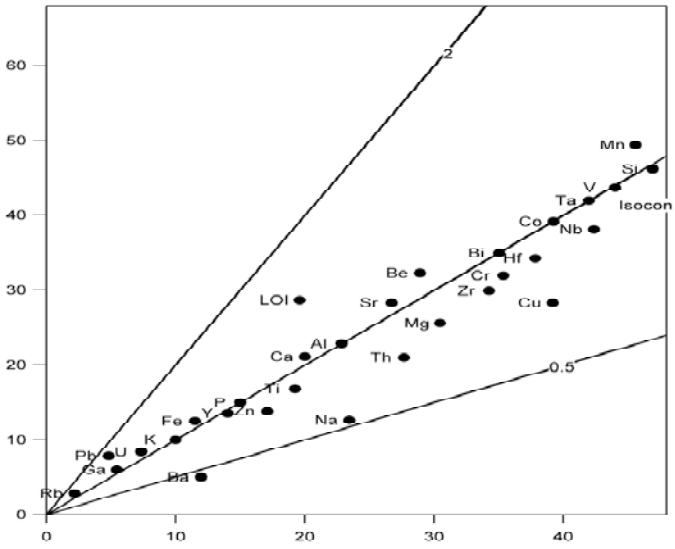

Fig 9.4.1: Isocon-diagram for sample C42A; Isocon calculated from Al, Si, K, P, Co. Slope = 0.99749 ± 0.00456; values were multiplied with constants for better presentability

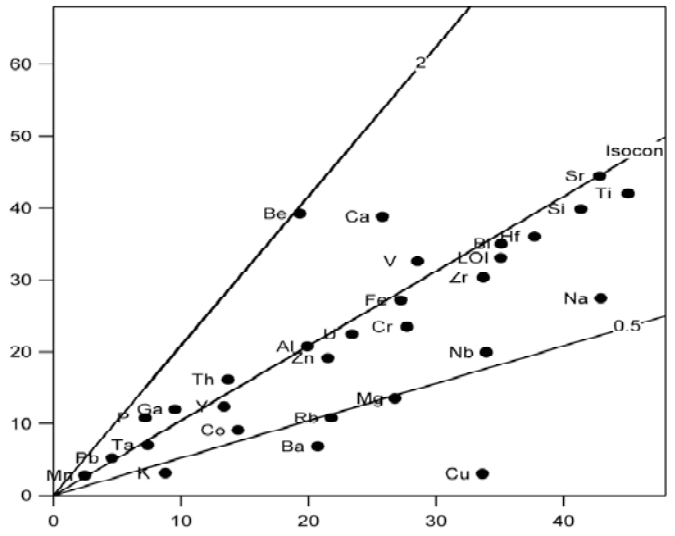

Fig 9.4.2: Isocon-diagram for sample C67A-II; Isocon calculated from Al, Sr. Slope = 1.04039 ± 0.00137; values were multiplied with constants for better presentability

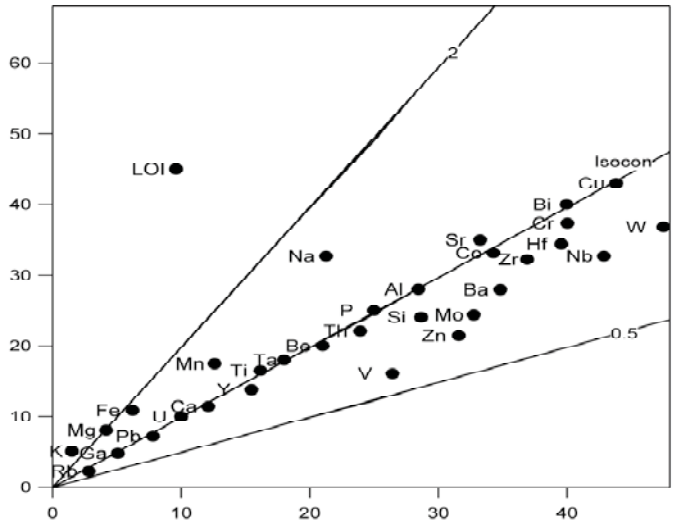

Figure 9.4.3: Isocon-diagram for sample C57A; Isocon calculated from Al, P, Be, Ta, Th. Slope = 0.9888 ± 0.00793; values were multiplied with constants for better presentability

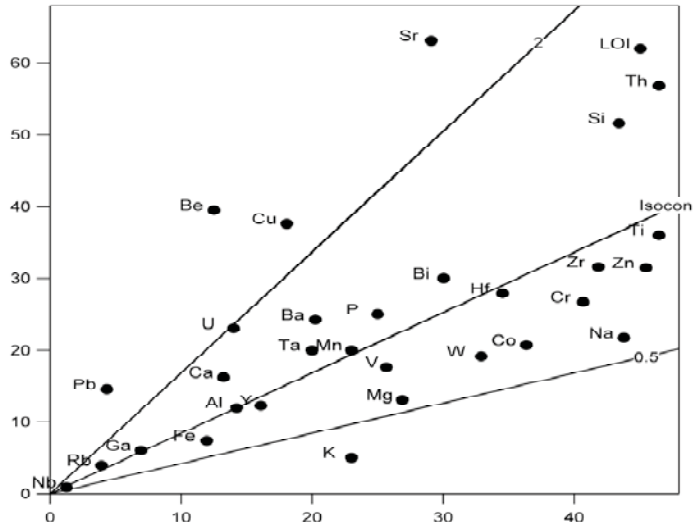

Figure 9.4.4: Isocon-diagram for sample C57B; Isocon calculated from Al, Mn, Ti. Slope = 0.84117 ± 0.001149; values were multiplied with constants for better presentability

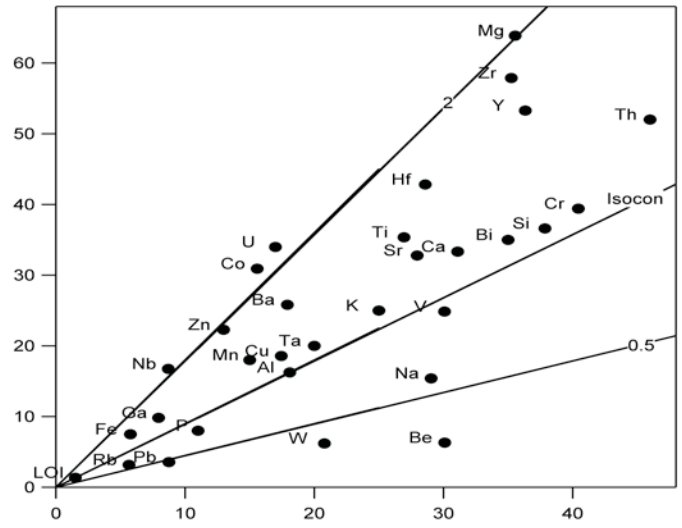

Figure 9.4.5: Isocon-diagram for sample IV35B; Isocon calculated from Al, K, LOI, Ta. Slope = 0.89314 ± 0.00946; values were multiplied with constants for better presentability

9.4.1.2. Type II calc-silicate alteration

Four sample pairs (C55A, C73A, IV10C and IV20B) have been selected to investigate chemical changes during this second type of calc-silicate alteration. The results of isocon calculations are shown on Figures 9.4.6 to 9.4.9. Due to the enhanced mobility of most elements during this type of calc-silicate alteration it is rather difficult to define valid isocons. For individual pairs often isocons can be calculated using an alternative set of elements and in all four isocon plots the slopes deviate very strongly from the ideal value of 1 Hence, results presented in the following only give some clue about how elements behaved during Type II calc-silicate alteration. Statements regarding relative depletion versus enrichment of individual elements must be considered with caution.

Except for Ca major elements behave in different ways. Ca is strongly enriched in all sample pairs (e.g. C73A) The trends for Si, Al and Fe are less clear. Si and Fe are enriched in the altered calc-silicate rocks except for sample IV10C. The LOI is lower in the altered part of sample pair IV20B but is enriched in the three other samples.

LIL elements are generally strongly depleted. In many cases elements like Ba, Pb, Sr, K and Rb have more than five times higher values in unaltered rocks than in altered ones. Only two exceptions of this general trend have to be reported. In sample pair C73A Sr lies very close to the isocon what means that it has not undergone such a significant alteration. Most peculiar is the behaviour of Pb in sample IV10C. It is the only LIL element that is enriched in the altered part.

Some HFSE were enriched during alteration. Nb, Hf and Ta are, partly strongly (Nb in IV10C and IV20B; U in IV10C; Ta in IV20B), enriched in the altered rock (calc-silicate rock). Ti on the other hand is only enriched in IV20B and lies below the Isocon line in all other samples. The same is valid for Hf. Zr is enriched in the altered zone in samples IV10C and IV20B but depleted in C55A and C73A.

The behaviour of transition elements is also inconsistent. Manganese shows enrichment in the altered zone in all four samples. Copper is depleted in all samples. Cobalt and Zn tend to show enrichment in the altered zone but both elements have mavericks in sample C55A for Co and in sample IV10C for Zn.

Tungsten is very strongly enriched during Type II calc-silicate alteration and to a minor extent is Mo.

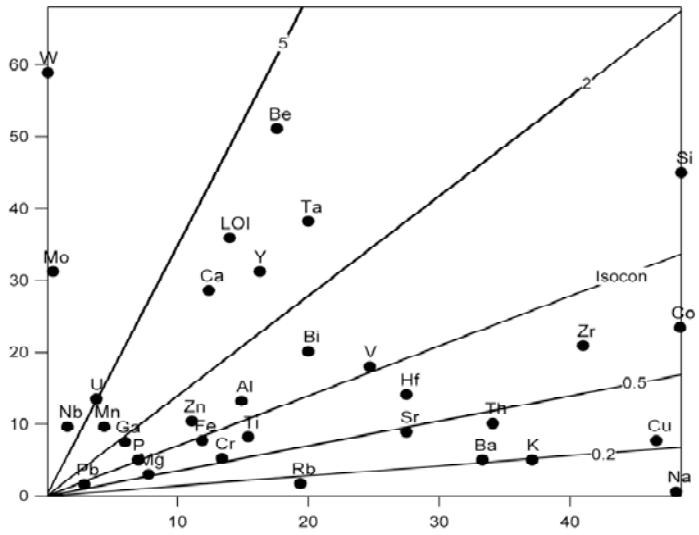

Figure 9.4.6: Isocon-diagram for sample C55A; ISocon calculated from Fe, P, V. Slope = 0.69507 ± 0.05722; values were multiplied with constants for better presentability

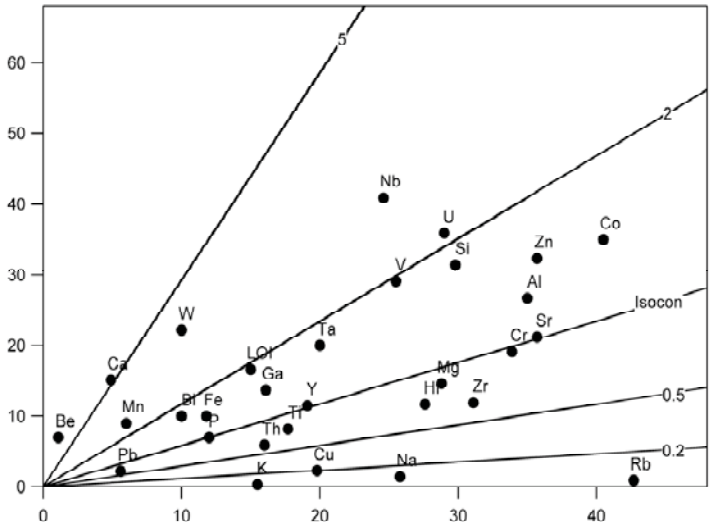

Figure 9.4.7: Isocon-diagram for sample C73A; Isocon calculated from P, Cr, Sr, Y. Slope = 0.58539 ± 0.04144; values were multiplied with constants for better presentability

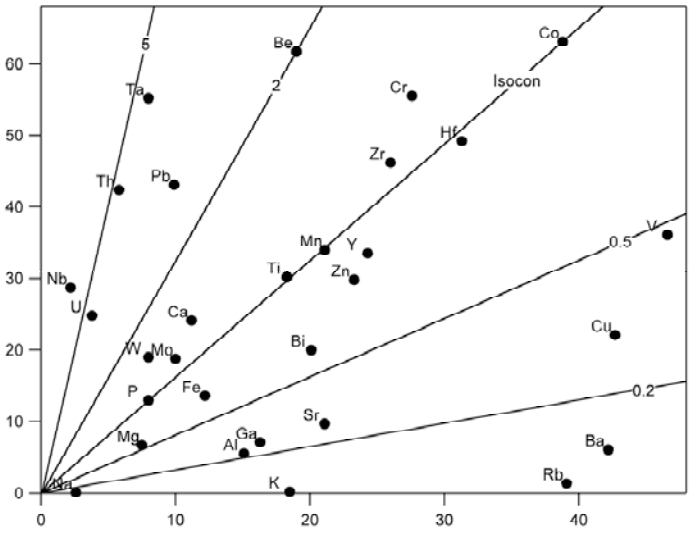

Figure 9.4.8: Isocon-diagram for sample IV10C; Isocon calculated from Mn, Ti, P, Co. Slope = 1.62761 ± 0.01167; values were multiplied with constants for better presentability

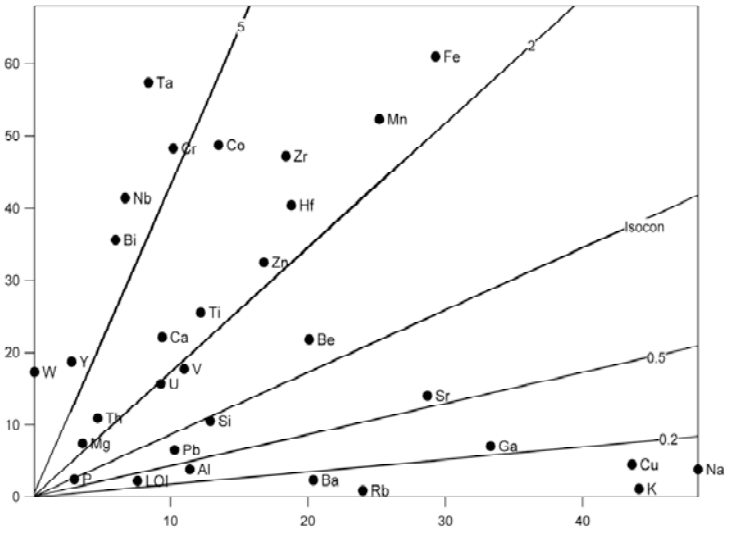

Figure 9.4.9: Isocon-diagram for sample IV20B; Isocon calculated from Si, P, Mo. Slope = 0.86265 ± 0.07117; values were multiplied with constants for better presentability

9.4.2. Mass balance calculations

Total mass changes can also be calculated with the Isocon program. For this purpose the Isocon programme normalises element concentrations to 100 g. As for the calculations of isocons one or more elements must be considered as immobile during the alteration processes. In most cases Al (plus other elements; as suggested by the Isocon programme) has been treated as immobile and mass balance calculations were based on this assumption

9.4.2.1. Calc-silicate alteration (Type I) of pillow basalts

Total mass changes for major elements within these samples are in the range of about –0.5 mass % (sample C42A) to +17 mass % (sample C57B). As shown in Figures 9.4.10 – 9.4.14 major quantitative changes are in Si. This is followed by Ca, Fe, Mg, Na and LOI. K and P contents can be neglected. Mostly because of the chosen immobile element association for mass balance calculations changes in Al, Mn and Ti are not significant.

The pillow basalt alteration cannot be linked to a systematic variation in major elements. Si as well as Fe, Mg and Na shows gains and losses in different samples. The only exception to this behaviour is Ca, which is enriched in all altered samples compared to their parents. Peculiar are the big changes of Si in samples C57A and C57B. C57B has quartz veins in the core of the pillow what can explain enrichment in Si.

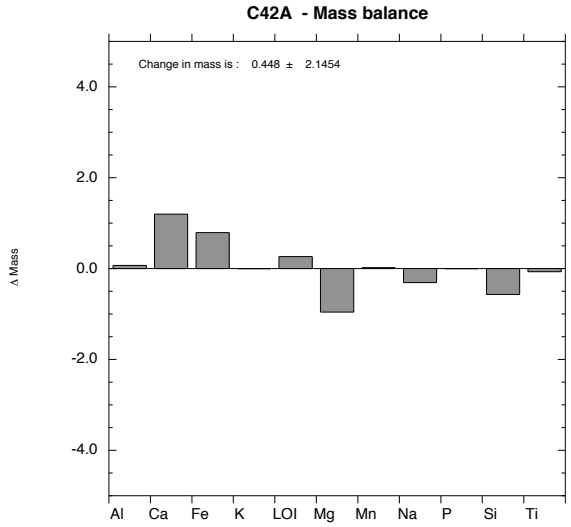

Figure 9.4.10: Mass balance for major elements of sample C42A

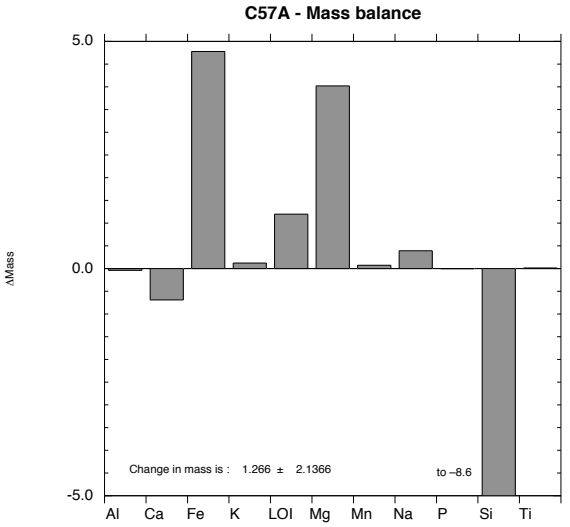

Figure 9.4.11: Mass balance for major elements of sample C57A

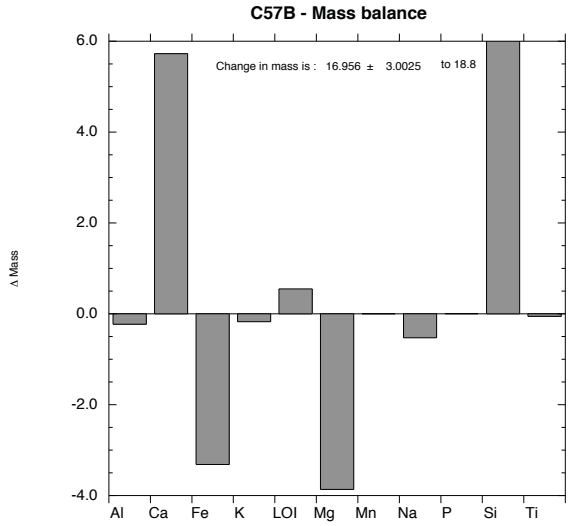

Figure 9.4.12: Mass balance for major elements of sample C57B

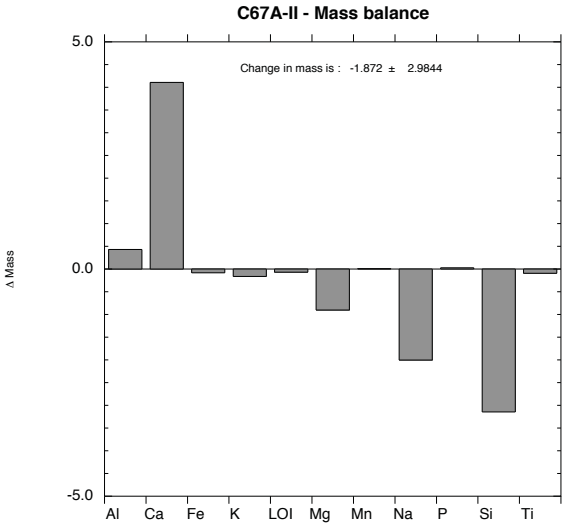

Figure 9.4.13: Mass balance for major elements of sample C67A-II

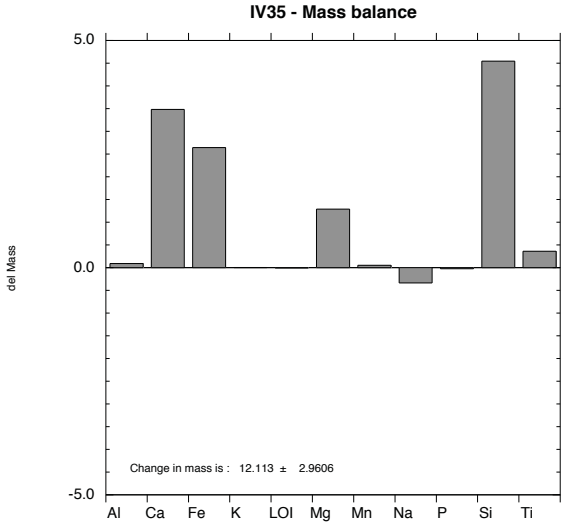

Figure 9.4.14: Mass balance for major elements of sample IV35

9.4.2.2. Type II calc-silicate alteration

Type II calc-silicate alteration lead to mass changes for major elements ranging from –7 mass % to +10.5 mass %. Most major elements were mobile during Type II calc-silicate alteration. As shown in Figures 9.4.15 – 9.4.17 major quantitative changes can be reported for Al and Ca. This contrasts changes in pillow basalts, where Al remains rather stable during alteration. Calcium, however, shows systematic enrichment throughout the whole set of samples. Partly Na and Mg show major changes, too whereas Si, Fe, K and LOI show only minor changes during this type of alteration. Changes in Ti, P and Mn are very small. Generally the alkalis Na, K as well as Mg are depleted during this kind of alteration.

No calculations are reported for sample pair IV20B. It is assumed that there is excessive pre-alteration variation in the major element composition of these rocks. Hence, calculations with these rock pair are considered to be meaningless.

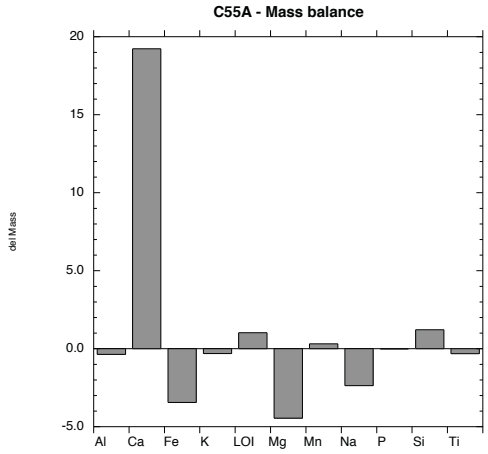

Figure 9.4.15: Mass balance for major elements of sample C555A

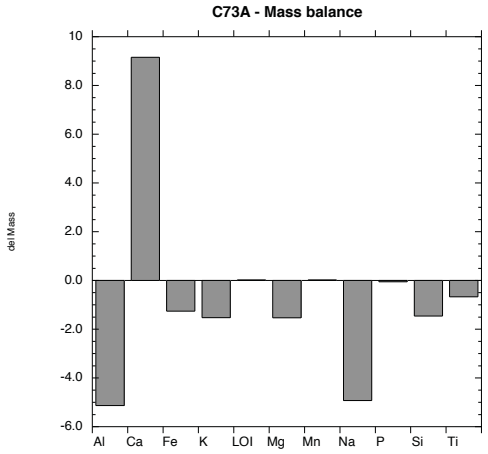

Figure 9.4.16: Mass balance for major elements sample C73A

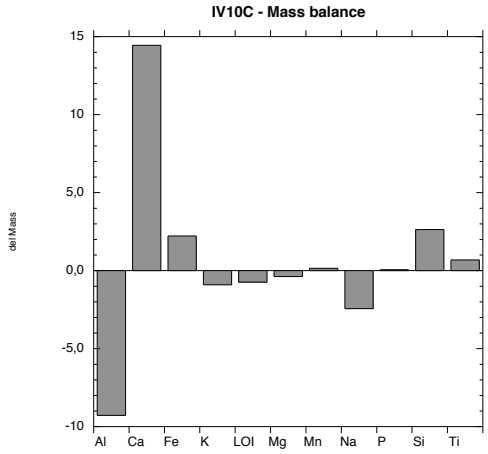

Figure 9.4.17: Mass balance for major elements of sample IV10C

9.4.3. Element mobilities

Another way of displaying the mobility of certain elements during alteration processes is to create a “staircase plot” (Figures 9.4.18 – 9.4.23). Here the values of altered samples are divided by the sum of altered and unaltered samples (ratio = altered / (altered + unaltered)). Hence a pair that was not affected by alteration has a ratio of 0.5 whereas total depletion or enrichment in one element pair would be illustrated by 0.0 and accordingly by 1.0.

9.4.3.1. Calc-silicate rocks Type I

Generally Type I calc-silicate rocks show rather flat patterns in staircase plots. Only few elements show significant enrichment or depletion. In sample C42A only U, Rb, LOI and Pb are enriched. However all four elements plot very close to the 0.50 line with larger error bars (Figure 9.4.18). On the other hand only Ba, Na and Cu are significantly depleted in this sample pair. Enrichment of certain elements like Sr, Mn, Na, Fe, Mg, K and LOI is much more significant in sample C57A. No elements are significantly depleted in this sample. However, the big error bar of W, due to the low concentrations, has to be regarded with caution. Like in sample C42A also in sample C57B U, Be and Pb are under the most enriched elements along with Th, LOI, Cu and Sr. Very obvious is the strong depletion of K and also Mg, Na, Co, W, Fe and Cr which is the opposite trend as in sample C57A but is similar to sample C67A-II where these elements are also under the most depleted. Additionally Cu and Rb are very strong depleted in sample C67A-II whereas Ca, P and Be are most enriched during alteration of this rock. Sample IV35B is different to other samples of this series. Here Be and Pb, which are enriched throughout all other samples, are very strongly depleted. Also W, Na, Rb and P are strongly depleted whereas Mg, Nb, Co and U are the most enriched samples.

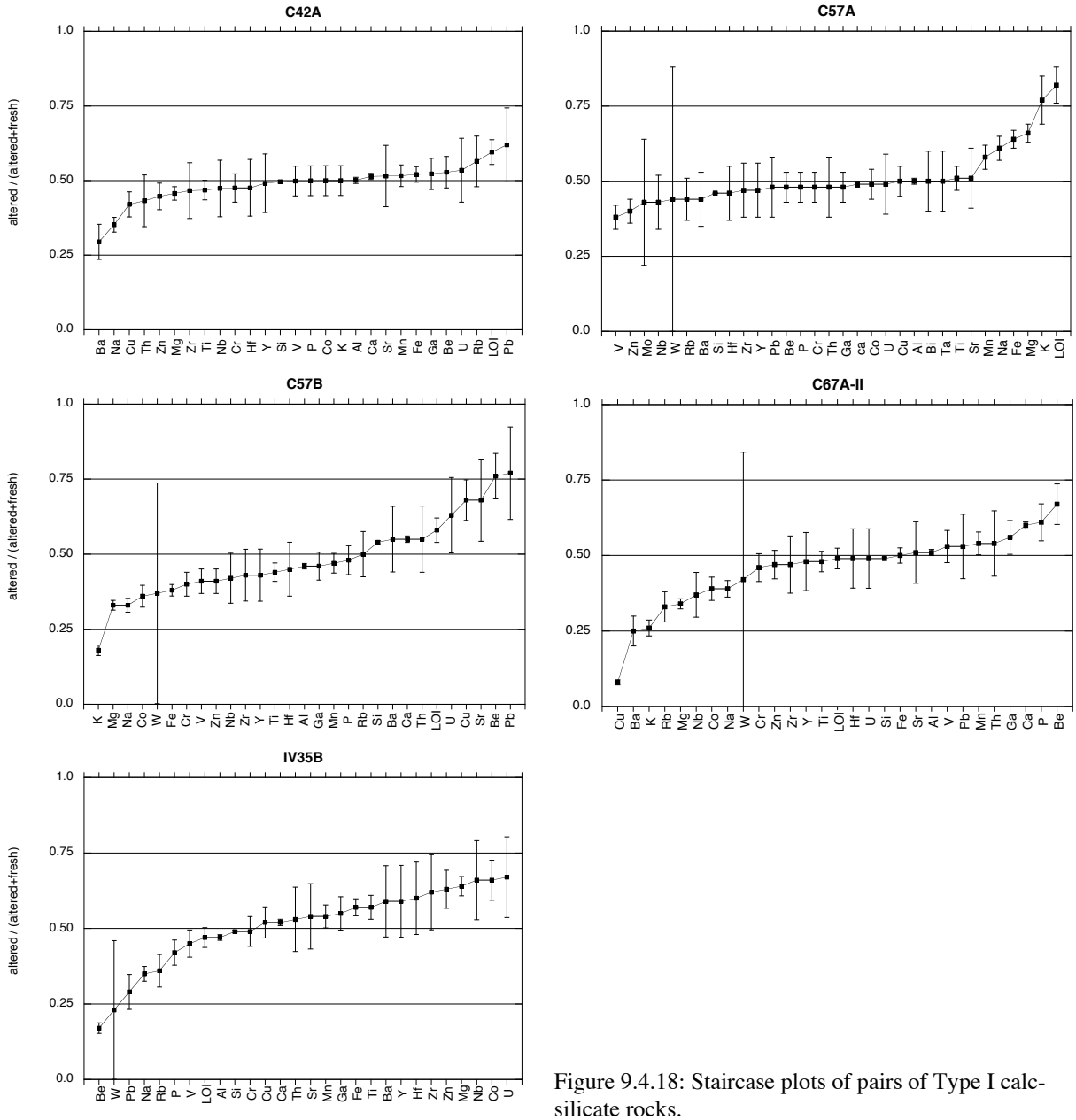

Figure 9.4.18: Staircase plots of pairs of Type I calc-silicate rocks.

9.4.3.2. Calc-silicate rocks Type II

In contrary to Type I calc-silicate rocks Type II calc-silicate rocks show more distinct patterns. The depletion of certain elements especially K, Rb, Na, Ba, Al, Ga and Sr is very obvious and can nearly reach as high as 100 % for K, Rb and also Ba in several samples of this type (Figures 9.4.19, 9.4.20 & 9.4.22). Pb, U, W and Ta were clearly enriched during this kind of alteration. However these calculations have to be considered with caution due to the low concentrations for all these elements and the resulting big uncertainties.

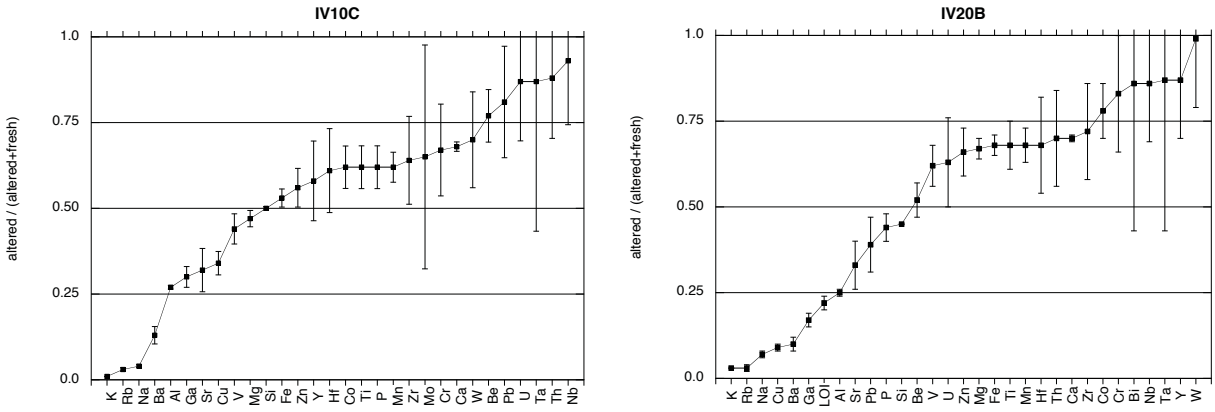

9.4.19: Staircase plots of samples IV10C and IV20B of Type II calc-silicate rocks.

9.4.4. Chemical changes in the transition zone vs Type II calc-silicate rocks

In some outcrops a distinct transition zone is developed between the unaltered host rocks and Type II calc-silicate rocks (see chapter 4; Figures 4.3.7 – 4.3.9 and chapter 6; Figure 6.2.10). This transition zone is interpreted to have formed by the progressive interaction of hydrothermal fluid with the host rock. In the following the chemical changes between transition type rocks and the unaltered host rocks are presented graphically and compared with the chemical changes recorded in the calc-silicate rocks, which are interpreted as the final products of alteration.

Figures 9.4.20 and 9.4.21 compare the mobility of elements in transition zone and in totally altered rocks during alteration. As shown in Figure 9.4.21 elements between Th and Si remain stable in the transition zone, whereas many of these elements seem to be more mobile in the

calc-silicate rocks. Interesting is the behaviour of Ga and V, which are slightly depleted in transition zone, and Zn, which is enriched in transition zone. Their trend in the transition zone is in opposition to that in completely altered calc-silicate rocks.

In both diagrams – those for calc-silicate rocks and transition zone rocks, respectively – some elements show consistent depletion or enrichment with respect to the unaltered rock. Elements exhibiting a significant enrichment include Mn, Nb, W, Ca, and Be, those exhibiting a significant depletion include the LIL elements Ba, K, Rb, Na ± Sr ± Th as well as Cu.

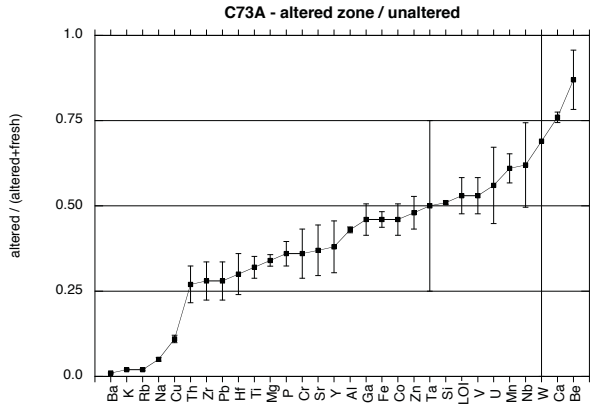

Figure 9.4.20: Element mobility in altered zone of sample C73A compared to unaltered zone; a value of 0 indicates total depletion of a certain element whereas 1 stands for 100 % enrichment; elements with a value of 0.5 are neither enriched nor depleted. Error bars indicate the 1 sigma analytical uncertainty of the chemical analysis.

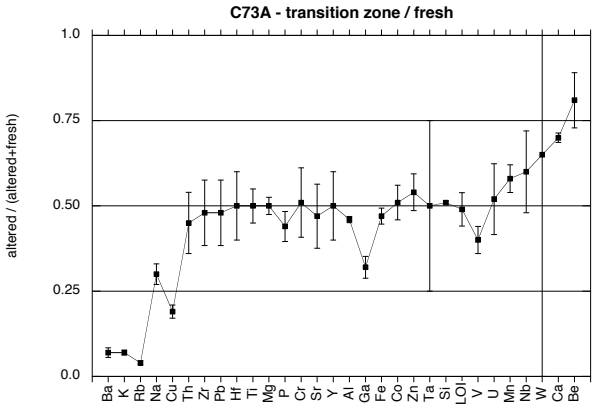

Figure 9.4.21: Element mobility in transition zone of sample C73A compared to unaltered zone; a value of 0 indicates total depletion of a certain element whereas 1 stands for 100 % enrichment; elements with a value of 0.5 are neither enriched nor depleted. Error bars indicate the 1 sigma analytical uncertainty of the chemical analysis.

Although there is more scatter in sample C55A (Figures 9.4.22 and 9.4.23) a similar behaviour of elements is documented for this sample. In addition to the elements listed for sample C73A U and Ta are enriched in this sample and Sr and Th are depleted.

Some elements in the middle parts of the diagrams like Cr, Mg, Co Zr, Hf etc. seem to be depleted in the calc-silicate vs. unaltered plots (Figures. 9.4.20 but 9.4.22) but do not show this depletion trend in the transition zone vs. unaltered plots (Figures 9.4.21 and 9.4.23). A possible explanation for this phenomenon could be that the *apparent* depletion of these elements simply reflects their dilution in the Ca-rich calc-silicate rocks, which gained a lot of Ca during the alteration process. Hence, for evaluating relative enrichment and depletion trends of elements during the alteration process the comparison of transition zone rocks gives the clearer results and is therefore preferable.

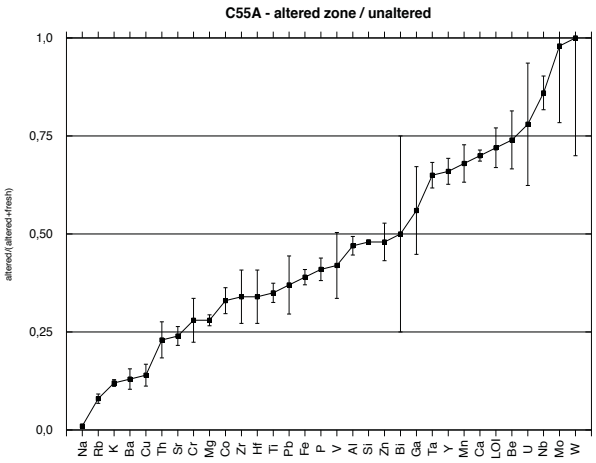

Figure 9.4.22: Element mobility in altered zone of sample C55A compared to unaltered zone; a value of 0 indicates total depletion of a certain element whereas 1 stands for 100 % enrichment; elements with a value of 0.5 are neither enriched nor depleted.

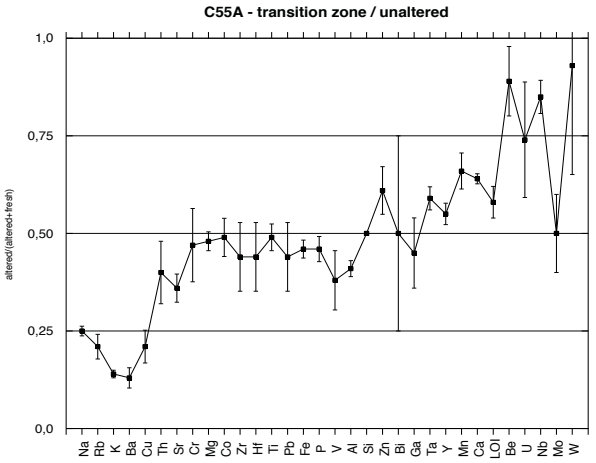

Figure 9.4.23: Element mobility in transition zone of sample C55A compared to unaltered zone; a value of 0 indicates total depletion of a certain element whereas 1 stands for 100 % enrichment; elements with a value of 0.5 are neither enriched nor depleted.

9.5. Classification of metabasites

The Jensen plot is a classification scheme for subalkaline volcanic rocks. The elements plotted in this diagram are chosen because of their inverse proportion to each other and because of their stability under low grades of metamorphism. It clearly discriminates komatiites, tholeiites from calc-alkaline rocks and is thus especially useful for classifying Archaean metavolcanics (Rollinson, 1993). As shown in chapters 9.1 to 9.4 alkalis have been quite mobile during both types of calc-silicate alteration, especially during Type II calc-silicate formation. It was also shown in Chapter 8 that P-T conditions reached upper amphibolite facies conditions in the study area. Thus, classical discrimination plots like the TAS-diagram cannot be applied and would lead to erroneous classifications. In contrast, Fe, Ti, Mg and Al were rather immobile during Type I calc-silicate alteration justifying their use for classifying the metvolcanics in the Ivisaartoq Greenstone Belt.

Data from pillow rims and the ocelli-rich intermediate pillow zones are plotted in figure 9.4.24. The samples represent the least altered metabasites (i.e., Type I altered pillow cores and samples influenced by Type II calc-silicate alteration were omitted) and hence can give a clue about the protoliths and magma characteristics. To extend our limited data set data by Polat et al. (2007) are included for comparison. Most samples plot in the field of High-Mg tholeiitic basalts, a few samples straddling the basalt field. Our own samples exhibit a larger spread and extend the total data set to andesitic and dacitic compositions. According to the

Jensen plot the samples studied show calc-alkaline magma characteristics. Only one sample (IV35B-R) plots at the border to the tholeiitic field.

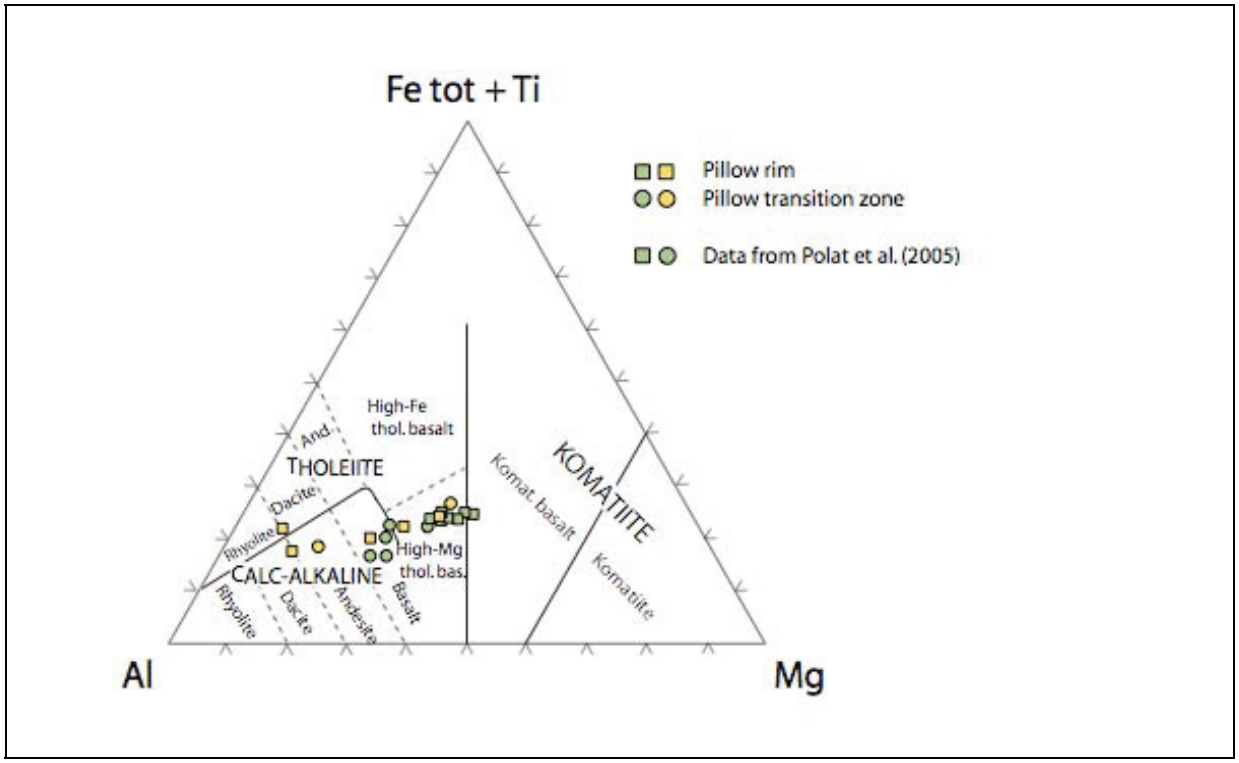

Figure 9.5.24: Jensen plot of pillow rims and transition zone samples; Data from Polat (2007) (green symbols) were added for comparison.

10. Discussion

The focus of this M.Sc. thesis is to provide answers to major scientific questions arising from field observations. It should be determined (1) if the two different types of calc-silicate rocks that can be distinguished in the field are comparable with respect to their chemical composition and (2) which geochemical signatures are to be related with calc-silicate rocks hosting strata-bound tungsten mineralisation.

10.1. Comparison of the two types of calc-silicate rocks

In the following chapter we shall compare the two main types of calc-silicate alteration present in the Ivisaartoq Greenstone Belt. It will be documented that the two types can be distinguished on the basis of field relations, relative timing of calc-silicate formation, as well as petrographic and geochemical criteria. The main differences of the two types of calc-silicate rocks are summarised in Table 10.1.

As shown in chapter 4 on the regional geology major differences have already been established in the field and resulted in a preliminary separation of the calc-silicate rocks into two main types. Type I is mostly linked to cores of altered pillow basalts (see Figures 4.3.2 – 4.3.6) whereas Type II can be found in discordant veins as well as in stratabound calc-silicate layers in metabasites, felsic gneisses and ultramafic rocks. It is clearly documented that Type II calc-silicate rocks replace structures (foliation, early folds) of an early penetrative deformation event (referred to as early D2 by Raith, 2004). A good example is given in Figures 4.3.11 & 4.3.12 of outcrop IV20. In contrast, Type I calc-silicate rocks are restricted to pillow cores, which have been deformed by this major deformation event. With respect to the timing of the events Type I calc-silicate alteration is considered as pre-metamorphic. Following the interpretation of Polat *et al.* (2007) this first calc-silicate alteration resulted in formation of low-grade calc-silicate rocks (e.g. epidosites) and was related to hydrothermal metamorphism on the seafloor. During subsequent isochemical (?) regional metamorphism these assemblages recrystallised and adapted to P-T conditions of the upper amphibolite facies.

As pointed out in chapter 6 on the petrography Type I alteration is characterised by mineral assemblages containing epidote, clinopyroxene, plagioclase, quartz, ± scapolite, ± titanite. In

contrast Type II calc-silicate rocks are dominated by assemblages containing calcic garnet, calcic clinopyroxene, epidote, quartz, calcite and titianite. Vesuvianite, calcic amphiboles and plagioclase have also been reported from some outcrops but are quantitatively less important. Scheelite is exclusively occurring in Type II calc-silicate rocks. Sulphides containing Cu, Fe, Ni, and Bi, (chalcopyrite, bornite, parkerite) are also restricted to the marginal zones of Type II calc-silicate alteration (Stückler, 2007)

In summary the main differences in petrography therefore are: the common assemblage of ep + qtz + plg + cpx with abundant plagioclase in Type I rocks, which contrasts with the common assemblage grt + cpx + ep + qtz in Type II calc-silicate rocks. Moreover, scapolite has so far only be found in Type I rocks whereas scheelite is restricted to those of Type II.

	Type I alteration	Type II alteration
Relative timing	pre-peak metamorphic (Polat *et al.*, 2007)	syn-peak metamorphic; post-date early D1 structures
Field relations	pillow cores	• veins; stratabound layers in metabasites, felsic gneisses and ultramafic rocks • replace first deformation event
Petrography	ep + cpx + plg + qtz ± scap ± ilm	qtz + cpx + ep + grt ± tit ± scheelite
Mineralisation	none	scheelite (W-Mo), minor Cu
Chemistry		
Major elements	immobile: Al, Ti some mobility: Si, Fe, strong mobility: Na, Ca, Mg	strong mobility of all major elements including Al Ca strongly enriched, Na strongly depleted
Trace elements		
LIL elements	some mobility: Ba, Pb,Th,	strongly depleted (up to 5 times): Ba, K, Rb, Na
HFS	some depletion: Nb, Zr, Hf, W	strongly enriched: Nb, Ta, U, W !
Transition elements	some mobility: Cu, Zn, Mn, Co; Be	Depletion in Cu; enrichment in Be
REE	flat, very minor LREE-enrichment	Most samples strongly LREE-enriched; rarely LREE depleted and flat patterns
	no to weakly negative Eu anomalies	Negative to positive Eu anomaly
	REE largely immobile except Eu	REE quite mobile !

Table 10.1: Comparison of characteristic features of Type I and Type II calc-silicate alteration

As pointed out in this study the two different types of alteration can also be discriminated using geochemical criteria. Major elements behave immobile (Al, Ti) to strongly mobile (Na, Ca, Mg) during Type I alteration whereas they are all considerably mobile during Type II alteration; in the latter, Ca is strongly enriched, and Na and even Al can be strongly depleted. There are significant differences in trace element distribution between the two types of calc-silicate rocks. LIL elements are to some extent (Na, Ba) affected by Type I alteration of pillow basalts (Figures 9.4.1 – 9.4.5) although the changes are not very systematic. In contrast, in calc-silicate rocks of Type II LIL elements are strongly depleted in a very systematic manner. K, Na, Ba, Pb, Sr and Rb are strongly depleted; concentrations of some of LIL elements can be as low as one fifth of the value in the unaltered host rock (Figures 9.4.6 – 9.4.9).

Some HFS elements behave mobile during Type I calc-silicate alteration. Niobium, Zr and Hf tend to be depleted during this alteration. In contrast Nb, Ta, U, Be are enriched up to five times during Type II alteration. W, and in some cases Mo are also strongly enriched during Type II alteration (Figures 9.4.6 – 9.4.9).

Transition elements like Cu, Zn, Mn, Co and Be show some mobility in both directions in Type I calc-silicate rocks. Type II is characterised by the depletion of Cu ($^1/_5$) and a strong enrichment of Be (up to 5 times).

The REE patterns for Type I calc-silicate rocks are generally flat to slightly enriched in LREE. They are very similar to those of the unaltered protoliths. Only rarely a slight increase in LREE is recognised. From the similarity of the patterns we conclude that the REE were not significantly affected during Type I alteration and that even the strongly altered pillow cores have largely preserved the REE pattern of the protolith. The only exception is sample C57B in which Eu is enriched in the altered part.

REE patterns of Type II rocks differ significantly from those of Type I. The patterns are far less consistent. Very different REE patterns are recorded for individual sample pairs showing either LREE or HREE enrichment (Figures 9.2.3 and 9.2.5). Comparison of the altered with the adjacent unaltered host rock sample (Figure 10.2) moreover indicates that the REE patterns of the calc-silicate rocks are not controlled by the host rock but e.g. by the mineralogy of the calc-silicate rocks and the REE composition of the infiltrating fluid. To

completely understand and discuss the processes controlling REE distribution in Type II calc-silicate rocks is beyond the scope of this thesis but what has to be stated here is that the REE were obviously strongly mobile during Type II calc-silicate alteration.

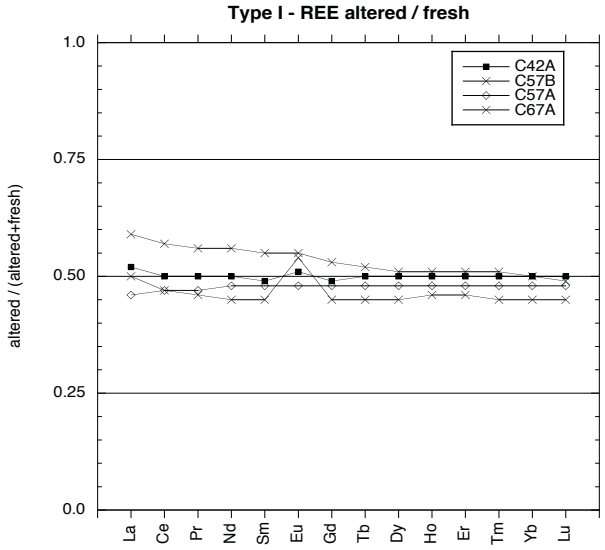

Figure 10.1: Mobility of REE in Type I altered rocks; a value of 0 indicates total depletion of a certain element whereas 1 stands for 100 % enrichment; elements with a value of 0.5 are neither enriched nor depleted.

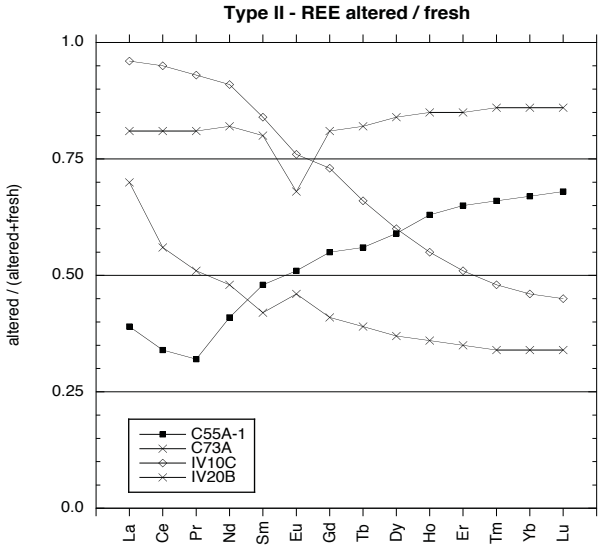

Figure 10.2: Mobility of REE in Type II altered rocks; a value of 0 indicates total depletion of a certain element whereas 1 stands for 100 % enrichment; elements with a value of 0.5 are neither enriched nor depleted.

10.2. Stratabound tungsten deposits

10.2.1. Overview about stratabound tungsten deposits

Stratabound tungsten deposits can form by various processes in different geological settings. According to the review by Cheilletz (1988) one can distinguish three major classes of stratabound tungsten deposits: 1) continental weathering deposits, 2) exhalative-volcanogenic deposits and, 3) concordant replacement deposits.

The source of the metal in continental weathering deposits (1) is of an exogene one. Tungsten minerals have a high susceptibility to surface alteration processes. This fact leads to decomposition of these minerals under a wide range of physico-chemical conditions, especially in the oxidation zone of primary deposits (Cheilletz, 1988 and literature therein). Alkaline or nitrogenous solutions provide best conditions for the transport of tungsten (Krainov, 1965 in Cheilletz, 1988). Precipitation of tungsten can occur by sorption of tungsten on iron and manganese hydroxides over a wide pH-range (Ivanova, 1966 in Cheilletz, 1988). Although detrital transport is possible it may only happen over very short distances in

alluvium or elluvium due to the cleavage properties of both scheelite and wolframite. Examples for this class are Searles Lake, California, USA, where tungsten is precipitated in terrestrial evaporites and continental placers in USSR and China (Cheilletz, 1988 and literature therein).

The second important group of stratiform tungsten deposits are the exhalative-volcanogenic deposits (2). Metals are thought to be of an endogene origin and their deposition is assumed to be driven by syn- and epigenetic processes. Exhalative-volcanogenic deposits are subdivided into “proximal” and “distal” deposits in relation to the distance to a volcanic centre (Cheilletz, 1988). Proximal deposits are characterised by explosive volcanism, acid magma compositions development, subvolcanic plutonism and intense wall-rock alteration caused by stockwork-type hydrothermal fluid circulation. Distal deposits on the contrary are formed in back-arc sedimentary basin environments in tension structures. They are typically associated with calc-alkaline and tholeiitic tuffs, black shales and W-Pb-Zn-Cu bedded mineralisation interlayered with chemically precipitated exhalites like chert, limestone, dolomite, barite and tourmalinite. Typical is also the association with silica-, iron- and manganese-bearing formations, tourmaline-bearing pelitic beds, calc-silicate formations, laminated Pb-Zn base-metal sulphides and amphibolites.

A transitional type between volcanogenic-exhalative and concordant replacement deposits are tungsten deposits hosted in amphibolites. They are made up of scheelite mineralisations that can be traced over considerable lateral distances and are linked to metabasites of volcanic origin. These deposits underwent intense folding, stretching and metamorphism during several orogenic cycles and thus Cheilletz (1988) used the spatial relationship of the mineralisation with amphibolites as the only argument for an exhalative-volcangenic origin.

What Cheilletz (1988) described as concordant replacement deposits (3) has also been referred to as some subtype of skarn type deposits (Einaudi & Burt, 1982; Kwak, 1987; Newberry, 1998). Those deposits are always stratabound and often stratiform. In contrast to proper magmatogenic skarns, however, concordant replacement deposits are not clearly connected with a granitic intrusion from where mineralised hydrothermal fluids emanate and replace (meta-) sedimentary Ca- or Mg-rich rocks. After Kwak (1987) the vast majority of economic Sn-W deposits have a granite-related origin. He states that 85 % of all investigated skarns occur within 800 m of a felsic intrusion.

Kwak (1987), however, also pointed out that there is some genetic ambiguity and that there exists a class of skarn type deposits which are not related to a granitic intrusion but which are instead found in regional metamorphic terrains. For these he introduced the term “regional” tungsten skarns. The latter show almost the same mineral assemblages as “normal” skarns containing garnet, pyroxene, epidote, chlorite, quartz, and calcite. Examples of this type are given in the Broken Hill block, N.S.W., Australia (Kwak, 1987, and references therein), the Bindal area, Norway (Berg Larsen, 1991), the Blacklite Prospect area, N.M., U.S.A. (Kwak, 1987, and references therein), the Bunte Serie, Bohemian Massif (Beran *et al.*, 1985) and Eastern Alps, Austria (Raith, 1991)

What all these deposits have in common is the relatively large distance to igneous contacts (> 5 km), the long distance over which mineralised horizons can be followed (5 – 10 km), the restriction of scheelite mineralisation to specific stratigraphic horizons, and the lack of mineralogical and chemical zoning of the ore bodies. Moreover, scapolite is common in some of these deposits and most deposits occur in medium to high-grade metamorphic regions. In many deposits like those of the Broken Hill Block tourmalinites, interpreted as boron-rich metaexhalaties, are spatially associated with scheelite mineralisation or even host the scheelite (Kwak, 1987; Plimer, 1987, 1994).

10.2.2. Genesis of tungsten mineralisation in the IGB

Syngenetic-exhalative models were favoured to explain the genesis of tungsten mineralisation in the IGB (Appel, 1988, a, b; 1994). In the following the arguments for this syngenetic model will be briefly summarised and opposed to alternative non-syngenetic models of tungsten concentration.

Pro syngenetic-exhalative model

- Tungsten mineralisation is stratiform to stratabound
- Mineralisation can be traced over several kilometres along strike
- Lithostratigraphic control of mineralisation (i.e. Magnetic Marker)
- No direct spatial link to felsic intrusive rocks
- Association of mineralisation with exhalites (tourmaline rocks)

Contra syngenetic-exhalative model

- Occurrence of intrusive rocks (pegmatites) in the vicinity of W mineralisation
- No restriction of mineralisation to specific stratigraphic horizons
- W mineralisation post-dates a first stage of calc-silicate alteration (Type I) related to ocean floor metamorphism
- Formation of W-bearing calc-silicate rocks (Type II) postdates a first deformational event
- Chemical analyses (enrichment of Nb, Ta, U, Be together with W) indicate a geochemical relation to felsic intrusive rocks

Appel (1988a, 1988b) was the first to recognise that scheelite in the Ivisaartoq Greenstone Belt is bound to specific horizons within the greenstone belt sequence. He reports that scheelite-bearing calc-silicate rocks can be traced over several kilometres along strike. They are mainly associated with metamorphosed mafic and ultramafic rocks. Furthermore a lithostratigraphic control of the mineralisation, which is mostly (but not exclusively) bound to the Magnetic Marker horizon, can be assumed. Scheelite mineralisation is spatially associated with tourmaline rocks as well as sulphide mineralisation; tourmaline rocks were interpreted as exhalative tourmalinites. All these arguments were used in support of a syngenetic-exhalative model for the origin of the tungsten mineralisation in the IGB (Appel, 1994).

Protolithic komatiites and tholeites underwent a first low grade ocean floor metamorphic event with the formation of an epidote-rich assemblages (Polat *et al.*, 2007). This first event was overprinted by a second amphibolite facies regional metamorphic event characterised by formation of diopside + epidote + plagioclase + quartz dominated assemblages in the former epidote-rich pre-metamorphically altered pillow cores (Polat *et al.*, 2007). Field observations (UV lamping) and results of chemical analysis of Type I calc-silicate alteration show that W is not an important element during this pre-metamorphic alteration stage. This is supported by (a) the lack of scheelite in this type of calc-silicate rocks and (b) by low W concentrations of Type I calc-silicate rocks.

Pegmatites are widespread in the study area and commonly occur in vicinity to W mineralisation (Chadwick 1988; Figure 4.3.1). However, they were ruled out to play a

significant role in forming W mineralisation because crosscutting field relationships with the calc-silicate rocks were reported (Ordonez-Calderon *et al.*, 2007) and they lack W mineralisation (Appel, 1994). Pegmatites are postulated to postdate regional amphibolite facies metamorphism and are therefore unlikely to be the source of the mineralisation (Ordonez-Calderon *et al.*, 2007). This would also exclude the idea of a classical magmatogenic skarn type deposit. However, these statements conflict with field observations (J. Raith, personal communication) indicating that some pegmatites are affected by the lateD2 and the D3 deformation events. Thus, a temporal relation of at least some of the pegmatites with the formation of Type II calc-silicate rocks cannot be excluded a priori. Additionally the geochemical signature of Type II calc-silicate rocks (enrichment of Nb, Ta, Be, U with W) gives independent evidence for the involvement of felsic magmas or hydrothermal fluids expelled from them in the mineralisation process.

As an alternative hypothesis to a magmatic-hydrothermal fluid source Ordonez – Calderon *et al.* (2007) suggested that mineralising fluids derived from metamorphic dehydration reactions. According to Van Hees *et al.* (1999) and Shelton *et al.* (2004) in Ordonez – Calderon (2007) dehydration of clastic metasedimentary rocks in greenstone belts have been recognised as an important source of fluids during regional metamorphism. This could result in intense metasomatism and ore deposition or mobilisation of pre-existing (e.g. syngenetic) ore deposits. As quantified in this study peak metamorphic conditions in the IGB reached upper amphibolite facies conditions. According to Kwak (1987) the link of stratiform tungsten deposits to amphibolite facies rocks as well as their association with tourmaline rocks may be good indications for a “regional” tungsten skarn deposit; in these, metamorphic fluids would be the preferential agent for transporting W.

Irrespective of the possible fluid source – magmatic vs. metamorphic – the stratabound appearance of scheelite mineralisation and its close spatial association to the Magnetic Marker horizon have still to be explained, if any of the epigenetic models is preferred over the syngenetic one. A possible explanation would be that the Magnetic Marker represents a synmetamorphic shear zone forming the tectonic contact between the upper and lower amphibolite units. This could have been a zone of enhanced fluid flow and fluid focussing. Reaction of W-transporting fluids migrating along this structurally controlled pathway with the chemically unusual rocks exposed along this zone (ultramafic to intermediate igneous

rocks, metasediments) could have caused formation of scheelite-bearing calc-silicate rocks along this zone.

10.3. Conclusions

1. Tungsten mineralisation is strata-bound and hosted by calc-silicate rocks of Type II, which are often associated with the Magnetic Marker horizon. In contrary to Type I calc-silicate rocks, which formed prior to the regional deformation and metamorphic events and which do not host any tungsten mineralisation, they formed after a first (D1) deformational event.

2. Tungsten-bearing Type II calc-silicate alteration lead to formation of a mineral paragenesis of quartz + clinopyroxene + epidote + garnet ± titanite ± scheelite as compared to epidote + clinopyroxene + plagioclase + quartz ± scapolite ± ilmenite for the tungsten free Type I alteration

3. A significant geochemical difference can be observed between the two types of calc-silicate rocks. Tungsten-bearing Type II calc-silicate rocks show strong mobility of major elements, especially enrichment of Ca and depletion of Na, enrichment of HFS elements (W, Nb, Ta, U), enrichment and depletion of REE, as well as strong and systematic depletion of LIL elements (Na, K, Ba, Rb). This behaviour of elements contrasts Type I calc-silicate alteration in pillow basalts, which shows less systematic changes.

4. The Magnetic Marker horizon is interpreted as a synmetamorphic shear zone and thus a tectonic contact along which fluids were focused and reacted with various host rocks to form skarn-type W mineralisation.

5. The role of pegmatite intrusions and magmatic-hydrothermal fluids derived from them has to be reconsidered. Especially the enrichment of certain elements such as Be, Nb, Ta, U together with W during Type II calc-silicate alteration indicates a pegmatitic influence.

6. Geothermobarometry yielded metamorphic temperatures between 550 and 650°C and pressures between 5.0 and 5.7 kbar confirming upper amphibolite facies conditions for the peak of regional metamorphism.

11. Acknowlwedgments

First of all I thank Ao. Prof. Dr. Johann G. Raith for offering me the opportunity to work on this interesting topic. I am grateful for his scientific input but also for his patience in correcting and editing my thesis.

Ao. Prof. Mag. Dr. Thomas Meisel, Institute for General and Analytical Chemistry, University of Leoben, is thanked for guiding me through the process of analytical chemistry and processing of REE and trace element data. Major element analyses were done at the Institute for Geosciences at Karl Franzens Universität Graz with the help of Ao. Prof. Mag. Dr. Christoph Hauzenberger.

Electron microprobe analyses were done at the E.F. Stumpfl microprobe laboratory of the UZAG Steiermark located at the University of Leoben. Dr. Frederica Zaccarini and Helmut Mühlhans are thanked for their support with these analyses. Special thanks go to late Mr. J. Seiser for preparing 70 excellent thin sections.

The Geological Society of Denmark and Greenland (GEUS) provided logistical and financial support for field work and also covered some of the analytical costs. Dr. Peter W.U. Appel is thanked for having made all this possible.

The Austrian Academy of Sciences (ÖAW), Kommission für Grundlagen der Mineralrohstofforschung, supported the project “Schichtgebundene Wolframvererzungen in Westgrönland” through a grant to J.G. Raith.

I also acknowledge the Society of Economic Geologists (SEG) for supporting this project through a Hugh E. McKinstry Fund student research grant.

I specially want to thank B.Sc (hons) Janine Pink for guiding me through the shallow waters of the English language and several problems MS office produces. The support of the “Dreimäderlzimmer” comprised of DI Angelika Ressler and DI Christoph Piribauer has to be thanked particularly for its creative input.

12. References

Appel, P.W.U., 1988a. Stratiform tourmalinites in the Archaean tungsten province of West Greenland. Mineralogy and Petrology, 39: 79 - 91.

Appel, P.W.U., 1988b. Tungsten mineralization in the Archaean of West Greenland. Krystalinikum, 19: 9 - 20.

Appel, P.W.U., 1994. Stratabound scheelite in altered Archaean komatiites, West Greenland. Mineralium Deposita, 29: 341 - 352.

Baadsgaard, H., McGregor, V.R., 1981. The U-Th-Pb systematics of zircons from type Nuuk gneisses, Godthabsfjord, West Greenland. Geochimica et Cosmochimica Acta, 50: 2173 - 2183.

Baumgartner, L.P., Olsen, S.N., 1995. A least-squares approach to mass transport calculations using the isocon method. Economic Geology and the Bulletin of the Society of Economic Geologists, 90: 1261 - 1270.

Beran, A., Göd, R., Götzinger, M., Zemann, J., 1985. A scheelite mineralization in calc-silicate rocks of the Moldanubicum (Bohemian Massif) in Austria. Mineral. Deposita, 20: 16 - 22.

Berg Larsen, R., 1991. Tungsten skarn mineralizations in a regional metamorphic terrain in northern Norway: a possible meetamorphic ore deposit. Mineral. Deposita, 26: 281 - 289.

Black, L.P., Gale, N.H., Moorbath, S., Pankhurst, R.J., McGregor, V.R., 1971. Isotopic dating of very early Precambrian amphibolite facies gneisses from the Godthab district, West Greenland. Earth and Planetary Science Letters, 12: 245 - 259.

Brown, M., Friend, C.R.L., McGregor, V.R., Perkins, W.T., 1981. The late Archaean Qorqut granite complex of southern West Greenland. Journal Geophysical Research, 86: 10617 - 10632.

Chadwick, B., 1985. Contrasting styles of tectonism and magmatism in the late Archaean crustal evolution of the northeastern part of the Ivisaartoq region, inner Godthabsfjord, southern West Greenland. Precambrian Research, 27: 215 - 236.

Chadwick, B., 1986. Malene stratigraphy and late Archaean structure: new data from Ivisaartoq, inner Godthabsfjord, southern West Greenland. Rapport Gronlands Geologiske Undersogelske, 130: 74 - 85.

Chadwick, B., 1990. The stratigraphy of a sheet of supracrustal rocks within the high-grade orthogneisses and its bearing on late Archaean structure in southern West Greenland. Journal of the Geological Society, London, 147: 639 - 652.

Chadwick, B., Coe, K., 1988. Geologisk kort over Gronland, 1:100.000, Ivisartoq 64 V.2 Nord. In: Appel, P.W.U. (Editor), Is there a gold province in the Nuuk region? Danmarks og Gronlands Geologiske Undersogelske Rapport.

Cheilletz, A., 1988. Stratiform tungsten deposits: a review. Geologie en Mijnbouw, 67: 293 - 311.

Einaudi, M.T., Burt, D.M., 1982. Skarn deposits. Economic Geology, 77 (Special issue devoted to skarn deposits): 745 - 754.

Friend, C.R.L., Nutman, A.P., 2005a. Complex 3670-3500 Ma orogenic episodes superimposed on juvenile crust accreted between 3850 and 3690 Ma, Itsaq Gneiss Complex, southern West Greenland. The Journal of Geology, 113: 375 - 397.

Friend, C.R.L., Nutman, A.P., 2005b. New pieces to the Archaean jigsaw puzzle in the Nuuk region, southern West Greenland: steps in transforming a simple insight into a complex regional tectonothermal model. Journal of the Geological Society, London, 162: 147 - 162.

Friend, C.R.L., Nutman, A.P., Baadsgaard, H., Kinny, P.D., McGregor, V.R., 1996. Timing of late Archaean terrane assembly, crustal thickening and granite emplacement in the Nuuk region, southern West Greenland. Earth and Planetary Science Letters, 142: 353 - 365.

Friend, C.R.L., Nutman, A.P., McGregor, V.R., 1987. Late-Archaean tectonics in the Faeringhaven-Tre Brodre area, south of Buksefjorden, southern West Greenland. Journal of the Geological Society, London, 144: 369 - 376.

Friend, C.R.L., Nutman, A.P., McGregor, V.R., 1988. Late Archaean terrane acretion in the Gothab region, southern West Greenland. Nature, 335: 535 - 538.

Grant, J.A., 1986. The isocon diagram - a simple solution to Gresens' equation for metasomatic alteration. Economic Geology, 81: 1976 - 1982.

Hall, R.P., Friend, C.R.L., 1983. Intrusive relationships between young and old Archaean gneisses: evidence from Ivisaartoq, southern West Greenland. Geological Journal, 18: 77 - 91.

Holland, T.J.B., Powell, R., 1998. An internally consistent thermodynamic data set for phases of petrological interest. Journal of Metamorphic Geology, 16(3): 309 - 343.

Kwak, T.A.P., 1987. W-Sn skarn deposits and related metamorphic skarns and granitoids. Developments in economic geology, 24. Elsevier, 451 pp.

Leake, B.E., Woolley, A.R., Arps, C.E.S., Birch, W.D., Gilbert, M.C., Grice, J.D., Hawthorne, F.C., Kato, A., Kisch, H.J., Krivovichev, V.G., Linthout, K., Laird, J., Mandarino, J.A., Maresch, W.V., Nickel, E.H., Rock, N.M.S., Schumacher, J.C., Smith, D.C., Stephenson, N.C.N., Ungaretti, L., Whittaker, E.J.W., Guo, Y., 1997. Nomenclature of amphiboles; report of the subcommittee on amphiboles of the International Mineralogical Association, Commission on New Minerals and Mineral Names. The Canadian Mineralogist, 35(1): 219 - 246.

McGregor, V.R., 1973. The early gneisses of the Godthab dstrict, West Greenland. Philosophical Transactions of the Royal Society of London, Series A(273): 343 - 358.

McGregor, V.R., 1979. Archaean gray gneisses and the origin of the continental crust: evidence from the Godthab region, West Greenland. In: Barker, F. (Editor), Trondhjemites, dacites and related rocks. Developments in Petrology, 6: 169 - 204.

Meisel, T., Schoener, N., Paliulionyte, V., Kahr, E., 2002. Determination of rare earth elements, Y, Th, Zr, Hf, Nb and Ta in geological reference materials G-2, G-3, SCo-1 and WGB-1 by sodium peroxide sintering and inductively coupled plasma-mass spectrometry. Geostandards Newsletter, 26(1): 53 - 61.

Moorbath, S., O'Nions, R.K., Pankhurst, R.J., Gale, N.H., McGregor, V.R., 1972. Further rubidium-strontium age determinations on the very early Precambrian rocks of the Godthab district, West Greenland. Nature, 240: 78 - 82.

Newberry, R.J., 1998. W - and Sn-skarn deposits: A 1998 status report. In: Lentz, D.R. (Editor), Mineralized intrusion-related skarn systems. Short Course Series. Mineralogical Association of Canada, 26, pp. 289 - 335.

Nutman, A.P., Friend, C.R.L., Bennett, V.C., McGregor, V.R., 2004. Dating of the Ameralik dyke swarms of the Nuuk district, southern West Greenland: mafic intrusion events starting from c. 3510 Ma. Journal of the Geological Society, London, 161: 421 - 430.

Nutman, A.P., McGregor, V.R., Friend, C.R.L., Bennett, V.C., Kinny, P.D., 1996. The Itsaq Gneiss Complex of southern West Greenland; the world's most extensive record of early crustal evolution (3900-3600 Ma). Precambrian Research, 78: 1 - 39.

Ordonez-Calderon, J.C., Polat, A., Fryer, B., Gagnon, J.E., Raith, J.G., Appel, P.W.U., 2007. Evidence for HFSE and REE mobility during calc-silicate metasomatism, Mesoarchean (~3075 Ma) Ivisaartoq greenstone belt, southern West Greenland. Precambrian Research, Precambrian Research, 61, 317 - 340.

Plimer, I.R., 1987. The association of tourmalinite with stratiform scheelite deposits. Mineral. Deposita, 22: 282 - 291.

Plimer, I.R., 1994. Strata-bound scheelite in meta-evaporites, Broken Hill, Australia. Economic Geology, 89(3): 423 - 437.

Polat, A., Appel, P.W.U., Frei, R., Pan, Y., Dilek, Y., Ordonez-Calderon, J.C., Fryer, B., Hollis, J.A., Raith, J.G., 2007. Field and geochemical characteristics of the Mesoarchean (~3075) Ivisaartoq greenstone belt, southern West Greenland: Evidence for seafloor hydrothermal alteration in supra-subduction oceanic crust. Gondwana Research, 11: 69 - 91.

Powell, R., Holland, T.J.B., 1988. An internally consistent dataset with uncertainties and correlations; 3, Applications to geobarometry, worked examples and a computer program. Journal of Metamorphic Geology, 6(2): 173 - 204.

Raith, J.G., 1991. Stratabound tungsten mineralization in regional matamorphic calc-silicate rocks from the Austroapline Crystalline Complex, Austria. Mineral. Deposita, 26: 72 - 80.

Raith, J.G., 2004. Scheelite mineralization in the Ivisaartoq greenstone belt, southern West Greenland. In: Appel, P.W.U. (Editor), Is there a gold Province in the Nuuk region? Danmarks og Gronlands Geologiske Undersogelske rapport, 2005/27, pp. 58 - 63.

Rollinson, H., 1993. Using geochemical data: evaluation, presentation, interpretation. Geochemistry Series, Longman, Harlow.

Rosing, M.T., Nutman, A.P., Lofqvist, L., 2001. A new fragment of the early Earth crust: the Aasivik terrane of West Greenland. Precambrian Research, 105: 115 - 128.

Stückler, P., 2007. Erzmikroskopische und mineralchemische Untersuchung von Erzproben aus der Nuuk Region, SW - Grönland, unveröffentlichte Bakkalaureatsarbeit Montanuniversität, Leoben, 44 pp.

Wells, P.R.A., 1976. Late Archaean metamorphism in the Buksefjorden region, southwest Greenland. Contributions to Mineralogy and Petrology., 56: 229 - 242.

Wells, P.R.A., 1979. Chemical and thermal evolution of Archaean sialic crust. Journal of Petrology, 20: 187 - 226.

13. Appendices

Appendix A – Sample list

Samples Year 2004

Sample no.:		Sample description	West		North		Altitude (m)
JR04	IV 5/1	cs rock, grt-cpx-qtz, scheelite in qtz vein (blue pole; mineralised horizon)	64°	44.03	49°	54.60	760
JR04	IV 5/2	cs rock, grt-cpx-qtz, scheelite (blue pole; mineralised horizon)	64°	44.03	49°	54.60	760
JR04	IV 5/3	cs rock, grt-cpx-qtz, scheelite (blue pole; mineralised horizon)	64°	44.03	49°	54.60	760
JR04	IV 5/4	cs rock, grt-cpx-qtz, scheelite in qtz vein (blue pole; mineralised horizon)	64°	44.03	49°	54.60	760
JR04	IV 5B	cs gneiss, white-green	64°	44.03	49°	54.60	760
JR04	IV 5C	cs gneiss, white-green; bt schist; qtz; sulfides and Cu staining	64°	44.03	49°	54.60	760
JR04	IV 5D	cs rock, grt-cpx-qtz (banded cs rock, mineralised horizon)	64°	44.03	49°	54.60	760
JR04	IV 6A	cs rock, green, coarse ep xx	64°	44.09	49°	54.29	737
JR04	IV 6B	amphibolite, banded	64°	44.09	49°	54.29	737
JR04	IV 6C	cs gneiss, white-green	64°	44.09	49°	54.29	737
JR04	IV 6D	mus-bt gneiss, well foliated	64°	44.09	49°	54.29	737
JR04	IV 6E	biotite gneiss, garnet-bearing	64°	44.09	49°	54.29	737
JR04	IV 7	biotite gneiss, garnet-bearing; elongate white mineral	64°	44.13	49°	54.20	
JR04	IV 9	altered pillow basalt, ep and amph-rich parts	64°	44.46	49°	52.25	1030
JR04	IV 10A	grt, cpx, cc xx	64°	44.58	49°	51.43	
JR04	IV 10B	cs marble?, magnetite	64°	44.58	49°	51.43	
JR04	IV 10C	cs rock-amphibolite contact	64°	44.58	49°	51.43	
JR04	IV 10D	mica schist	64°	44.58	49°	51.43	
JR04	IV 10E, F, G	chips with MoS2	64°	44.58	49°	51.43	
JR04	IV 10H	cs rock (green) with cs vein (fsp?+ep+Mos2)	64°	44.58	49°	51.43	
JR04	IV 10J	cs boudin in amphibolite	64°	44.58	49°	51.43	
JR04	IV 20A	cs rock, coarse (ep-cpx?-amph?), qtz	64°	44.30	49°	53.07	1000
JR04	IV 20B	cs rock, coarse, banded (ep-cpx?-amph?), qtz veins	64°	44.30	49°	53.07	1000
JR04	IV 20C	tourm? -qtz	64°	44.30	49°	53.07	1000
JR04	IV 26	cs rock, grt-cpx-cc; grt xx	64°	44.41	49°	52.33	1008
JR04	IV 26B	marble, weathered	64°	44.41	49°	52.33	1008
JR04	IV 26C	cpx ? xx in marble	64°	44.41	49°	52.33	1008
JR04	IV 26D	black cs minerals in calciate matrix	64°	44.41	49°	52.33	1008
JR04	IV 26E	black green cs rock	64°	44.41	49°	52.33	1008
JR04	IV 26F	mica schist	64°	44.41	49°	52.33	1008
JR04	IV 33	mica schist, garnet-bearing	64°	44.41	49°	52.18	1007
JR04	IV 34	amphibolite, spotted	64°	44.54	49°	51.15	980
JR04	IV 35A	felsic gneiss	64°	44.40	49°	52.18	1053
JR04	IV 35B	pillow basalt, alteration zones (grt-qtz in core)	64°	44.40	49°	52.18	1053
JR04	IV 37A	felsic gneiss, fine-grained					
JR04	IV 37B	mica schist, garnet-bearing					
JR04	IV 37C	amphibolite, banded + cs boudin					

Samples Year 2005

Sample no.:		GEUS no.:	Sample describtion:	West			North		Altitude (m)
JR05	C42A + C42B	482780	epidotizised part of pillow basalt	64°	44,90		49°	51,82	1011
JR05	C45A	482781	contact of massive grt-cpx +- ep cs rock to grey fine-gr. gneiss	64°	44,50		49°	51,39	1028
JR05	C45B	482782	calc-silicate rock, calcite-rich	64°	44,50		49°	51,39	1028
JR05	C46	482783	biotite gneiss	64°	44,51		49°	51,28	1014
JR05	C49	482784	molybdenite?-bearing biotite-chlorite schist	64°	44,46		49°	51,51	1130
JR05	C50	482785	rusty weathered cs-rock with secondary Cu minerals	64°	44,47		49°	51,44	1060
JR05	C51	482786	dissem. sulphide in cs-rock	64°	44,46		49°	51,35	1039
JR05	C52	482787	sulphide-bearing chlorite schist, green	64°	44,48		49°	51,03	1033
JR05	C55A	482788	transition zone of cs-layer to amphibolite	64°	44,65		49°	51,92	971
JR05	C55B	482789	qz vein	64°	44,65		49°	51,92	971
JR05	C55C	482790	qz vein	64°	44,65		49°	51,92	971
JR05	C57A + C57B	482791	transition of epidot-rich core zone to frescher amphibolite (pillow basalt)	64°	44,79		49°	52,46	963
JR05	C58	482792	ultramafic rock with chromite? - magnetite vein	64°	44,92		49°	52,03	1009
JR05	C60A	482793	vesuvianite-bearing calcite-rich cs-rock	64°	44,51		49°	51,43	1019
JR05	C60B	482794	vesuvianite-bearing calcite-rich cs-rock; contact sample	64°	44,51		49°	51,43	1019
JR05	C61	482795	contact of pegmatite to cs-rock	64°	44,53		49°	51,19	1009
JR05	C62	482796	grt-bt-chl? schist	64°	44,31		49°	51,59	959
JR05	C64	482797	amphibolite with dissem. sulphide	64°	44,20		49°	50,94	922
JR05	C65	482798	rusty red brown vein quartz; sulphide-bearing	64°	44,21		49°	50,83	935
JR05	C67A + C67B + C67C	482799	altered pillow basalt; core + middle + rim	64°	44,63		49°	52,27	
JR05	C68A + C68B	482101	cs-rock with epidote vein and contact to amphibolite	64°	44,52		49°	53,33	950
JR05	C69A	482102	felsic "gneiss"	64°	44,31		49°	52,95	952
JR05	C69B	482103	magnetic marker schist	64°	44,31		49°	52,95	952
JR05	C70	482104	leucocratic gneiss with layer of fine-grained tourmaline	64°	44,35		49°	52,79	956
JR05	C71A + C71B + C71C	482105	garnet-biotite (-sillimanite) schist	64°	44,43		49°	52,04	1013
JR05	C73A	482106	grt-qtz-ep cs-vein	64°	44,53		49°	52,97	969
JR05	C73B	482107	cs-vein within mafic dyke	64°	44,53		49°	52,97	969
JR05	C73C	482108	biotite gneiss (silicified pillow basalt)	64°	44,53		49°	52,97	969
JR05	C73D	482109	core of ep-qtz altered pillow basalt	64°	44,53		49°	52,97	969

Sample no.:		GEUS no.:	Sample describtion:	West			North		Altitude (m)
JR05	C74A + C74B	482110	scapolite-bearing vein	64°	44,44		49°	52,23	1001
JR05	C74C	482111	hbl crystrals on foliation plane of amphibolite	64°	44,44		49°	52,23	1001
JR05	C74D	482112	felsic gneiss with ?tourmaline?	64°	44,44		49°	52,23	1001
JR05	C74E	482113	part of altered pillow core	64°	44,44		49°	52,23	1001
JR05	C74F	482114	white vein in cs-rock (?scapolite - qtz?)	64°	44,44		49°	52,23	1001
JR05	C75	482115	hbl-zone at the contact of massive cs-layer and amphibolite	64°	44,36		49°	52,43	1004
JR05	C75A + C75B	none	scapolite-bearing vein	64°	44,36		49°	52,43	1004
JR05	C75C	none	amphibolite with hbl crystals on foliation plane	64°	44,36		49°	52,43	1004
JR05	C75D	none	felsic gneiss with biotite and possibly tourmaline?	64°	44,36		49°	52,43	1004
JR05	C77	482116	cs-rock, ?grt-rich	64°	44,34		49°	52,73	977
JR05	C78	482117	sulphide-stained felsic / quartzitic gneiss	64°	44,50		49°	51,75	1008
JR05	C79	482118	felsic gneiss; rusty weathering	64°	44,52		49°	51,79	1003
JR05	C80	482119	garnet-clinopyroxene cs-rock with qtz vein	64°	44,53		49°	51,58	1000
JR05	C81	482120	amphibole-magnetite meta-ultramafic rock	64°	44,78		49°	51,48	980
JR05	C82	482121	cumulate-textured ultramafic rock (?cumulus mineral?)	64°	44,76		49°	51,32	993
JR05	C83A	482122	amphibole-rich rock, fine-grained	64°	44,75		49°	51,41	992
JR05	C83B	482123	ultramafic rock, coarse grained; with large porphyroblast?	64°	44,75		49°	51,41	992
JR05	C84A + C84B	482124	pegmatite (hughe fsp xx-qtz-mus), for fluid analyses	64°	44,49		49°	51,80	1006
JR05	C85	482125	qtz-ep vein in amphibolite, for fluid analyses	64°	44,44		49°	51,88	1016
JR05	C44	482126	amphibole relics in cs-rock	64°	44,49		49°	51,57	1014
JR05	C86A	482127	grt-schist / gneiss	64°	44,48		49°	51,68	1013
JR05	C86B	482128	rusty quartzitic gneiss with sulphides?	64°	44,48		49°	51,68	1013
JR05	C86C	482129	felsic gneiss, orientated sample	64°	44,48		49°	51,68	1013
JR05	C87A	482130	tourmaline?-bearing rock	64°	44,47		49°	52,00	998
JR05	C87B	482131	rusty quartzitic rock with sulphides?	64°	44,47		49°	52,00	998
JR05	C87C	482132	felsic rock with leucosome material	64°	44,47		49°	52,00	998
JR05	C88	482133	felsic gneiss with ?tourmaline?	64°	44,44		49°	52,14	1011
JR05	C89	482134	cs-marble	64°	44,41		49°	52,24	1011
JR05	C90	482135	amphibolite with large white patchy spots	64°	44,44		49°	51,88	1016
JR05	C91	482136	hbl-bt-gneiss with folded cs-layer	64°	44,38		49°	52,23	1013
JR05	C72	482137	cs-marble	64°	44,41		49°	52,28	1009
JR05	C51B I	none	calc-silicate rock, banded; scheelite in s// stringers and in thin vein	64°	44,46		49°	51,35	1039
JR05	C51B II	none	calc-silicate rock, banded; scheelite in s// stringers and in thin ep- cal? vein	64°	44,46		49°	51,35	1039
JR05	C51B III	none	calc-silicate rock, scheelite	64°	44,46		49°	51,35	1039
JR05	C51B IV	none	calc-silicate rock, scheelite preferentially in fractures/veins	64°	44,46		49°	51,35	1039
JR05	C51B V	none	calc-silicate rock, scheelite preferentially in fractures/veins	64°	44,46		49°	51,35	1039
JR05	C51B VI	none	calc-silicate rock, scheelite preferentially in fractures/veins	64°	44,46		49°	51,35	1039
	2T3	none	calc-silicate rock, cpx-rich; dissem. And porph. Scheelite (blue)	64°	44,43		49°	52,01	1013
	2T6A	none	calc-silicate rock, fine grained; small grt-xx	64°	44,41		49°	52,13	1011

Sample no.:		GEUS no.:	Sample describtion:	West			North		Altitude (m)
	2T6B	none	calc-silicate rock, fine grained; elongate scheelite stringers (mm-cm long; white to blue)	64°	44,41		49°	52,13	1011
	2T6C	none	calc-silicate rock, fine grained; elongate scheelite stringers (mm-cm long; white to blue)	64°	44,41		49°	52,13	1011
	2T8A	none	qtz vein with lichen; a few specks of blue scheelite	64°	44,41		49°	52,20	1019
	2T8B	none	calc-silicate rock, banded (grt-cpx); s // scheelite stringers (whiteyellow)	64°	44,41		49°	52,20	1019
	2T8C	none	calc-silicate rock, banded (grt-cpx); NO scheelite	64°	44,41		49°	52,20	1019
	2T8D	none	calc-silicate rock, banded (grt-cpx); s // scheelite stringers (cm, whiteyellow to blue)	64°	44,41		49°	52,20	1019
	2T12A	none	calc-silicate rock, banded (grt-cpx); s // scheelite stringers (whiteyellow)	64°	44,37		49°	52,44	994
	2T12B	none	calc-silicate rock, banded (green) with thin grt-richer "vein" cm scheelite (yellowwhite)	64°	44,37		49°	52,44	994
	2T12C	none	calc-silicate rock with scheelite vein	64°	44,37		49°	52,44	994
	2T12D	none	calc-silicate rock, banded (grt-cpx); s // scheelite stringers (cm, whiteyellow to blue)	64°	44,37		49°	52,44	994
	2T12E	none	calc-silicate rock, banded (grt-cpx); s // scheelite stringers (cm, whiteyellow to blue)	64°	44,37		49°	52,44	994
	2T16-17	none	calc-silicate rock, fine-gr. in contact with amphibolite; 5cm scheelite // s; blue)	64°	44,36		49°	52,57	983
	2T18 = C77	none	calc-silicate rock (grt-rich) in contact with amphibolite	64°	44,34		49°	52,73	977
	2T19	none	calc-silicate rock, banded (green) with grt-rich "nest" cm; scheelite stringers + porph. (yellow white)	64°	44,43		49°	52,27	1005
JR05	C21A	none	calc-silicate rock (grt-rich) contact with amphibolite; mm sized scheelite	64°	44,34		49°	52,73	976
JR05	C21B	none	metabasite, fine-grained; mm s// qtz vein with scheelite	64°	44,34		49°	52,73	976

Appendix B

B1. EMP – data and calculated cations for sample C71B

Mineral	b	b	b	b	b	b	g	g	g	g	g
Sample	1c71b_k3	2c71b_k3	3c71b_k3	1c71b_k5	2c71b_k5	3c71b_k5	1C71B_k2	2C71B_k2	9C71B_k2	1c71b_k3	2c71b_k3
SiO_2	33.54	33.75	33.45	33.35	33.60	33.15	36.37	36.30	36.05	35.79	35.85
TiO_2	2.54	2.50	2.33	2.52	2.60	2.44	0.04	0.01	0.01	0.00	0.00
Al_2O_3	19.70	19.82	20.01	19.60	19.91	19.99	20.54	20.79	20.61	20.50	20.54
FeO^*	23.03	23.17	23.11	23.65	23.04	22.71	36.66	36.58	37.11	36.85	37.04
MnO	0.01	0.01	0.00	0.00	0.00	0.01	2.03	2.09	2.05	1.90	1.98
MgO	6.56	6.68	6.83	6.54	6.60	6.67	2.07	2.14	2.00	2.07	2.24
CaO	0.00	0.00	0.00	0.00	0.00	0.01	1.53	1.60	1.83	1.70	1.61
Na_2O	0.17	0.20	0.21	0.25	0.21	0.27	0.00	0.00	0.00	0.03	0.00
K_2O	9.58	9.60	9.47	9.63	9.56	9.73	0.02	0.00	0.00	0.01	0.01
Total	95.12	95.72	95.39	95.54	95.51	94.98	99.24	99.51	99.64	98.84	99.26
Cations											
Oxygens	22	22	22	22	22	22	12	12	12	12	12
Si	5.231	5.231	5.200	5.201	5.216	5.182	2.985	2.971	2.958	2.958	2.952
Al	3.622	3.620	3.666	3.604	3.643	3.684	1.987	2.006	1.993	1.997	1.994
Ti	0.298	0.292	0.272	0.295	0.303	0.286	0.002	0.001	0.000	0.000	0.000
Fe^{2+}	3.004	3.003	3.004	3.085	2.991	2.968	2.516	2.503	2.547	2.547	2.550
Mn	0.002	0.001	0.000	0.000	0.000	0.002	0.141	0.145	0.142	0.133	0.138
Mg	1.525	1.543	1.584	1.521	1.527	1.554	0.253	0.261	0.245	0.255	0.275
Ca	0.000	0.000	0.000	0.000	0.000	0.002	0.134	0.140	0.160	0.151	0.142
Na	0.050	0.061	0.062	0.075	0.062	0.082	0.000	0.000	0.000	0.005	0.000
K	1.907	1.897	1.877	1.916	1.894	1.941	0.002	0.000	0.000	0.001	0.001
Total	15.639	15.647	15.665	15.697	15.637	15.701	8.021	8.026	8.045	8.046	8.052

b biotite, g garnet, m muscovite, p plagioclase; *) total Fe as FeO

Mineral	g	g	g	g	g	g	g	g	m	m	m
Sample	3c71b_k3	4c71b_k3	8c71b_k3	9c71b_k3	10c71b_k3	11c71b_k3	1c71b_k5_1_grt	2c71b_k5_1_grt	4c71b_k5	5c71b_k5	6c71b_k5
SiO_2	35.54	35.07	35.94	35.88	35.83	36.33	36.66	35.43	43.94	44.16	44.38
TiO_2	0.01	0.02	0.04	0.06	0.00	0.00	0.00	0.01	0.53	0.63	0.80
Al_2O_3	20.38	20.29	21.04	20.49	20.59	20.42	21.17	21.12	35.16	35.41	35.55
FeO*	36.72	36.61	36.94	36.66	36.83	36.91	37.08	36.78	2.00	1.77	1.67
MnO	2.04	2.05	1.95	2.06	2.00	1.96	2.22	2.14	0.00	0.00	0.00
MgO	2.17	2.01	2.05	2.04	2.16	1.82	2.03	1.82	0.38	0.40	0.35
CaO	1.65	1.67	1.68	1.82	1.61	1.65	1.63	1.67	0.00	0.02	0.00
Na_2O	0.00	0.02	0.03	0.00	0.01	0.03	0.01	0.00	0.91	0.89	0.86
K_2O	0.02	0.00	0.00	0.00	0.01	0.01	0.02	0.00	10.56	10.80	10.81
Total	98.53	97.74	99.67	99.01	99.04	99.13	100.81	98.97	93.48	94.06	94.41
Cations											
Oxygens	12	12	12	12	12	12	12	12	22	22	22
Si	2.950	2.939	2.943	2.960	2.954	2.990	2.964	2.926	6.016	6.008	6.010
Al	1.994	2.004	2.031	1.992	2.001	1.981	2.018	2.056	5.674	5.679	5.674
Ti	0.001	0.001	0.003	0.004	0.000	0.000	0.000	0.001	0.054	0.064	0.082
Fe	2.549	2.566	2.530	2.529	2.540	2.540	2.507	2.541	0.229	0.201	0.189
Mn	0.143	0.146	0.135	0.144	0.140	0.137	0.152	0.149	0.000	0.000	0.000
Mg	0.268	0.251	0.250	0.251	0.266	0.223	0.244	0.224	0.078	0.081	0.071
Ca	0.147	0.150	0.147	0.161	0.143	0.146	0.141	0.148	0.000	0.003	0.000
Na	0.000	0.003	0.005	0.000	0.002	0.005	0.002	0.000	0.241	0.234	0.225
K	0.002	0.000	0.000	0.000	0.001	0.001	0.002	0.000	1.844	1.874	1.867
Total	8.054	8.060	8.042	8.041	8.046	8.023	8.029	8.045	14.136	14.143	14.117

b biotite, g garnet, m muscovite, p plagioclase; *) total Fe as FeO

Mineral	p	p	p	p	p	p	p	p	p	p	p
Sample	1c71b_k2	2c71b_k2	3c71b_k2	4c71b_k2	5c71b_k2	4c71b_k3	5c71b_k3	6c71b_k3	7c71b_k3	8c71b_k3	7c71b_k5
SiO_2	57.27	56.56	57.03	57.09	57.02	56.27	56.64	57.27	57.53	57.02	57.05
TiO_2	0.02	0.00	0.01	0.00	0.01	0.00	0.03	0.01	0.02	0.01	0.00
Al_2O_3	26.63	26.65	26.68	26.56	26.65	26.47	26.42	26.54	26.35	26.16	26.21
FeO*	0.08	0.03	0.07	0.03	0.00	0.06	0.06	0.05	0.14	0.17	0.09
MnO	0.00	0.00	0.00	0.00	0.00	0.00	0.00	0.00	0.00	0.00	0.00
MgO	0.00	0.00	0.00	0.00	0.00	0.00	0.00	0.00	0.00	0.00	0.00
CaO	8.22	8.12	8.13	8.09	8.09	8.13	8.18	8.17	7.81	7.91	8.00
Na_2O	8.15	8.13	8.30	8.38	8.42	8.18	8.22	8.21	8.31	8.51	8.28
K_2O	0.05	0.06	0.06	0.07	0.10	0.08	0.05	0.06	0.08	0.05	0.09
Total	100.41	99.55	100.28	100.21	100.30	99.21	99.59	100.32	100.24	99.84	99.71
Cations											
Oxygens	8	8	8	8	8	8	8	8	8	8	8
Si	2.568	2.558	2.562	2.566	2.562	2.556	2.562	2.570	2.582	2.574	2.576
Al	1.407	1.421	1.413	1.407	1.411	1.418	1.409	1.404	1.394	1.392	1.395
Ti	0.001	0.000	0.000	0.000	0.000	0.000	0.001	0.000	0.001	0.000	0.000
Fe	0.003	0.001	0.002	0.001	0.000	0.002	0.002	0.002	0.005	0.006	0.003
Mn	0.000	0.000	0.000	0.000	0.000	0.000	0.000	0.000	0.000	0.000	0.000
Mg	0.000	0.000	0.000	0.000	0.000	0.000	0.000	0.000	0.000	0.000	0.000
Ca	0.395	0.394	0.391	0.390	0.389	0.396	0.396	0.393	0.376	0.383	0.387
Na	0.708	0.713	0.723	0.730	0.734	0.721	0.721	0.714	0.723	0.745	0.725
K	0.003	0.003	0.003	0.004	0.006	0.005	0.003	0.004	0.005	0.003	0.005
Total	5.084	5.090	5.095	5.097	5.102	5.098	5.094	5.086	5.084	5.103	5.091

b biotite, g garnet, m muscovite, p plagioclase; *) total Fe as FeO

B2. EMP – data and calculated cations for sample IV26F

Mineral	amph	amph	amph	amph	amph	b	b	b	chl	ilm	p
Sample	34iv26f_k2	35iv26f_k2	40iv26f_k2	41iv26f_k2	42iv26f_k2	38iv26f_k2	39iv26f_k2	45iv26f_k2	36iv26f_k2	37iv26f_k2	43iv26f_k2
SiO_2	39.38	24.77	36.46	39.25	39.12	33.94	34.17	34.16	23.24	0.01	64.49
TiO_2	0.37	0.08	0.02	0.38	0.30	2.58	2.53	2.60	0.58	54.45	0.02
Al_2O_3	15.31	19.86	20.84	15.67	15.10	16.77	17.00	16.99	21.89	0.02	21.81
FeO^*	23.64	31.57	32.41	23.19	24.92	25.03	24.73	24.59	31.57	46.10	0.27
MnO	0.05	0.04	0.80	0.05	0.04	0.02	0.02	0.01	0.04	0.02	0.01
MgO	3.55	10.53	0.93	3.68	3.33	6.74	6.76	6.74	9.19	0.23	0.00
CaO	11.05	0.02	3.45	11.22	11.01	0.05	0.01	0.00	0.01	0.03	2.30
Na_2O	1.85	0.00	0.03	1.82	1.81	0.09	0.06	0.04	0.01	0.04	12.35
K_2O	0.68	0.01	0.04	0.61	0.74	9.40	9.81	9.84	0.01	0.03	0.05
Total	95.88	86.87	94.98	95.87	96.38	94.61	95.08	94.98	86.53	100.92	101.29
Cations											
Oxygens	23	23	23	23	23	22	22	22	28	6	8
Si	6.223	4.489	5.875	6.188	6.194	5.390	5.397	5.398	5.157	0.001	2.830
Al	2.851	4.241	3.959	2.913	2.818	3.138	3.164	3.165	5.724	0.001	1.128
Ti	0.043	0.010	0.003	0.045	0.036	0.309	0.300	0.309	0.096	2.031	0.001
Fe	3.124	4.784	4.368	3.058	3.300	3.324	3.267	3.251	5.857	1.913	0.010
Mn	0.006	0.006	0.109	0.007	0.006	0.002	0.003	0.002	0.007	0.001	0.000
Mg	0.837	2.845	0.223	0.865	0.786	1.596	1.591	1.588	3.038	0.017	0.000
Ca	1.870	0.004	0.595	1.895	1.869	0.009	0.001	0.000	0.003	0.001	0.108
Na	0.567	0.000	0.011	0.557	0.554	0.026	0.019	0.013	0.005	0.004	1.051
K	0.138	0.003	0.007	0.122	0.150	1.904	1.976	1.983	0.003	0.002	0.003
Total	15.661	16.381	15.151	15.651	15.713	15.698	15.718	15.709	19.889	3.970	5.132

amph amphibole, b biotite, g garnet, m muscovite, p plagioclase, chl chlorite, il ilmenite; *) total Fe as FeO

Mineral	p	p	p	p	amph	amph	b	b	b	b	b
Sample	44iv26f_k2	46iv26f_k2	47iv26f_k2	48iv26f_k2	61iv26f_k4	62iv26f_k4	49iv26f_k4	52iv26f_k4	53iv26f_k4	54iv26f_k4	57iv26f_k4
SiO_2	65.28	63.64	61.37	61.94	36.23	36.41	33.77	34.01	34.03	33.81	33.24
TiO_2	0.03	0.00	0.00	0.00	0.16	0.07	2.48	2.45	2.45	2.49	2.44
Al_2O_3	20.89	22.02	23.70	22.91	21.09	20.96	16.90	16.91	16.90	17.11	16.86
FeO*	0.29	0.04	0.06	0.05	35.12	34.98	24.97	25.19	25.13	25.29	26.08
MnO	0.00	0.00	0.00	0.00	0.57	0.71	0.01	0.02	0.01	0.01	0.01
MgO	0.01	0.01	0.00	0.00	1.01	0.92	5.98	6.08	6.10	6.18	6.31
CaO	1.50	2.72	4.43	3.89	2.55	2.50	0.03	0.06	0.03	0.01	0.06
Na_2O	12.83	12.24	10.92	11.35	0.02	0.04	0.13	0.13	0.12	0.07	0.07
K_2O	0.04	0.05	0.08	0.05	0.01	0.01	9.46	9.14	9.58	9.56	8.97
Total	100.86	100.71	100.56	100.19	96.76	96.59	93.73	93.98	94.35	94.54	94.02
Cations											
Oxygens	8	8	8	8	23	23	22	22	22	22	22
Si	2.872	2.812	2.726	2.759	5.783	5.818	5.418	5.432	5.425	5.383	5.337
Al	1.083	1.147	1.241	1.203	3.968	3.948	3.195	3.182	3.176	3.212	3.190
Ti	0.001	0.000	0.000	0.000	0.019	0.008	0.300	0.294	0.294	0.298	0.294
Fe	0.010	0.002	0.002	0.002	4.687	4.675	3.350	3.365	3.350	3.368	3.502
Mn	0.000	0.000	0.000	0.000	0.078	0.096	0.001	0.002	0.001	0.001	0.001
Mg	0.001	0.001	0.000	0.000	0.240	0.218	1.430	1.447	1.449	1.468	1.510
Ca	0.071	0.129	0.211	0.185	0.436	0.429	0.005	0.010	0.006	0.002	0.010
Na	1.094	1.049	0.941	0.980	0.007	0.013	0.040	0.039	0.038	0.022	0.021
K	0.002	0.003	0.004	0.003	0.002	0.002	1.935	1.862	1.948	1.941	1.836
Total	5.134	5.141	5.126	5.131	15.219	15.207	15.673	15.634	15.687	15.695	15.702

amph amphibole, b biotite, g garnet, m muscovite, p plagioclase, chl chlorite, il ilmenite; *) total Fe as FeO

Mineral	b	b	b	b	b	ilm	ilm	p	p	p	p
Sample	60iv26f_k4	63iv26f_k4	64iv26f_k4	67iv26f_k4	68iv26f_k4	51iv26f_k4	59iv26f_k4	50iv26f_k4	58iv26f_k4	65iv26f_k4	66iv26f_k4
SiO_2	33.85	33.93	33.99	33.88	33.94	0.01	0.04	63.55	63.25	63.31	63.83
TiO_2	2.61	2.51	2.55	2.42	2.60	53.94	53.83	0.01	0.00	0.00	0.03
Al_2O_3	16.82	16.88	16.52	16.78	16.92	0.01	0.03	21.97	21.95	22.07	21.89
FeO*	25.04	25.70	25.75	24.92	24.91	45.59	45.14	0.03	0.03	0.11	0.05
MnO	0.02	0.02	0.01	0.02	0.01	0.05	0.09	0.00	0.00	0.00	0.00
MgO	6.09	6.08	6.30	5.80	6.02	0.15	0.13	0.01	0.00	0.02	0.00
CaO	0.06	0.02	0.11	0.03	0.05	0.06	0.07	2.96	2.76	3.11	2.86
Na_2O	0.04	0.10	0.09	0.09	0.09	0.01	0.03	11.89	11.91	11.89	12.11
K_2O	9.43	9.46	8.97	8.88	9.34	0.00	0.01	0.06	0.08	0.07	0.05
Total	93.96	94.69	94.28	92.82	93.88	99.81	99.36	100.49	99.99	100.58	100.82
Cations											
Oxygens	22	22	22	22	22	6	6	8	8	8	8
Si	5.415	5.401	5.423	5.466	5.426	0.001	0.002	2.813	2.813	2.803	2.817
Al	3.172	3.167	3.108	3.192	3.189	0.001	0.002	1.146	1.151	1.152	1.139
Ti	0.314	0.301	0.305	0.294	0.313	2.034	2.037	0.000	0.000	0.000	0.001
Fe	3.350	3.421	3.436	3.362	3.330	1.912	1.900	0.001	0.001	0.004	0.002
Mn	0.002	0.002	0.001	0.002	0.001	0.002	0.004	0.000	0.000	0.000	0.000
Mg	1.453	1.443	1.498	1.395	1.434	0.011	0.010	0.001	0.000	0.001	0.000
Ca	0.011	0.004	0.019	0.005	0.008	0.003	0.004	0.140	0.132	0.147	0.135
Na	0.012	0.030	0.028	0.029	0.028	0.001	0.003	1.021	1.027	1.021	1.036
K	1.923	1.920	1.826	1.828	1.905	0.000	0.001	0.003	0.005	0.004	0.003
Total	15.653	15.690	15.644	15.573	15.634	3.965	3.962	5.126	5.128	5.133	5.133

amph amphibole, b biotite, g garnet, m muscovite, p plagioclase, chl chlorite, il ilmenite; *) total Fe as FeO

Mineral	g	g	g	g	g	g	g	g	g	g	g
Sample	1iv26f_kr1	2iv26f_kr1	3iv26f_kr1	4iv26f_kr1	5iv26f_kr1	1iv26f_kr2	2iv26f_kr2	3iv26f_kr2	1iv26f_kr4	4iv26f_kr4	5iv26f_kr4
SiO_2	35.97	35.30	35.75	35.58	35.95	35.33	35.64	36.13	36.02	35.75	36.29
TiO_2	0.04	0.09	0.03	0.07	0.07	0.03	0.03	0.02	0.05	0.08	0.06
Al_2O_3	20.60	20.45	20.42	20.27	20.29	20.19	20.33	20.29	20.41	20.33	20.33
FeO*	35.42	34.97	34.86	32.79	34.73	34.33	35.27	35.01	35.63	35.23	35.67
MnO	2.98	3.02	3.28	4.59	3.45	3.09	3.19	3.26	2.90	3.23	2.93
MgO	1.71	1.68	1.57	1.37	1.56	1.50	1.39	1.26	1.66	1.44	1.59
CaO	2.47	2.72	2.81	3.92	3.00	3.15	2.81	3.00	2.67	2.69	2.58
Na_2O	0.02	0.00	0.04	0.06	0.01	0.01	0.02	0.00	0.03	0.00	0.00
K_2O	0.01	0.01	0.01	0.00	0.01	0.00	0.00	0.00	0.00	0.00	0.00
Total	99.21	98.23	98.77	98.65	99.08	97.62	98.69	98.97	99.37	98.75	99.46
Cations											
Oxygens	12	12	12	12	12	12	12	12	12	12	12
Si	2.961	2.939	2.959	2.951	2.967	2.958	2.958	2.984	2.964	2.963	2.981
Al	1.998	2.007	1.992	1.981	1.973	1.993	1.988	1.975	1.980	1.986	1.969
Ti	0.002	0.005	0.002	0.004	0.005	0.002	0.002	0.001	0.003	0.005	0.004
Fe	2.438	2.435	2.413	2.274	2.397	2.403	2.448	2.418	2.452	2.442	2.451
Mn	0.208	0.213	0.230	0.322	0.241	0.219	0.224	0.228	0.202	0.226	0.204
Mg	0.209	0.208	0.193	0.169	0.192	0.187	0.172	0.155	0.203	0.178	0.195
Ca	0.218	0.243	0.249	0.348	0.266	0.283	0.250	0.266	0.235	0.239	0.227
Na	0.003	0.000	0.006	0.010	0.001	0.001	0.004	0.000	0.005	0.000	0.000
K	0.001	0.001	0.001	0.000	0.001	0.000	0.000	0.000	0.000	0.000	0.000
Total	8.039	8.052	8.046	8.059	8.043	8.045	8.048	8.027	8.046	8.039	8.031

amph amphibole, b biotite, g garnet, m muscovite, p plagioclase, chl chlorite, il ilmenite; *) total Fe as FeO

Mineral	g	p	p	amph	amph	amph	amph	b	chl	chl	p
Sample	6iv26f_kr4	78iv26f_	81iv26f	69iv26f_	70iv26f	71iv26f	79iv26f	76iv26f	72iv26f	73iv26f	74iv26f
SiO_2	35.77	66.26	66.44	39.63	40.26	40.42	39.62	34.23	23.95	24.13	62.32
TiO_2	0.14	0.02	0.01	0.36	0.38	0.34	0.20	2.83	0.10	0.13	0.01
Al_2O_3	20.53	20.22	19.86	16.25	15.40	15.89	16.09	16.17	20.96	21.62	22.69
FeO*	35.78	0.20	0.26	22.21	22.04	21.40	21.24	22.86	29.63	29.89	0.19
MnO	2.73	0.00	0.00	0.03	0.04	0.04	0.04	0.02	0.03	0.03	0.00
MgO	1.63	0.00	0.01	4.14	4.38	4.32	3.98	6.99	9.52	9.58	0.00
CaO	2.38	0.90	0.41	11.17	11.29	11.30	11.08	0.02	0.07	0.03	3.81
Na_2O	0.01	13.52	13.81	1.61	1.67	1.56	1.64	0.02	0.01	0.04	11.26
K_2O	0.01	0.03	0.05	0.58	0.59	0.62	0.59	9.89	0.31	0.15	0.04
Total	98.98	101.16	100.86	95.96	96.04	95.87	94.47	93.03	84.59	85.59	100.32
Cations											
Oxygens	12	8	8	23	23	23	23	22	28	28	8
Si	2.954	2.903	2.919	6.192	6.282	6.290	6.261	5.489	5.392	5.356	2.771
Al	1.999	1.045	1.028	2.993	2.832	2.914	2.997	3.055	5.560	5.657	1.189
Ti	0.009	0.001	0.000	0.042	0.045	0.040	0.024	0.342	0.017	0.022	0.000
Fe	2.471	0.007	0.010	2.903	2.875	2.784	2.807	3.065	5.577	5.549	0.007
Mn	0.191	0.000	0.000	0.004	0.005	0.005	0.005	0.003	0.006	0.005	0.000
Mg	0.201	0.000	0.001	0.964	1.019	1.001	0.937	1.670	3.196	3.168	0.000
Ca	0.211	0.042	0.019	1.870	1.888	1.884	1.876	0.004	0.017	0.008	0.181
Na	0.002	1.148	1.177	0.487	0.504	0.470	0.503	0.005	0.005	0.015	0.971
K	0.001	0.002	0.003	0.115	0.116	0.122	0.118	2.024	0.089	0.041	0.002
Total	8.039	5.149	5.157	15.570	15.567	15.509	15.528	15.656	19.859	19.822	5.121

amph amphibole, b biotite, g garnet, m muscovite, p plagioclase, chl chlorite, il ilmenite; *) total Fe as FeO

Mineral	p	p	p
Sample	75iv26f_symplectitic	77iv26f_symplectitic	80iv26f_symplectitic
SiO_2	66.03	65.52	65.57
TiO_2	0.02	0.00	0.01
Al_2O_3	19.94	20.88	20.47
FeO^*	0.37	0.12	0.19
MnO	0.01	0.00	0.00
MgO	0.00	0.00	0.01
CaO	0.85	1.37	1.15
Na_2O	13.35	12.68	13.01
K_2O	0.04	0.05	0.05
Total	100.60	100.63	100.46
Cations			
Oxygens	8	8	8
Si	2.910	2.882	2.892
Al	1.036	1.083	1.064
Ti	0.000	0.000	0.000
Fe	0.014	0.004	0.007
Mn	0.000	0.000	0.000
Mg	0.000	0.000	0.001
Ca	0.040	0.064	0.054
Na	1.141	1.081	1.112
K	0.002	0.003	0.003
Total	5.143	5.118	5.133

amph amphibole, b biotite, g garnet, m muscovite, p plagioclase, chl chlorite, il ilmenite; *) total Fe as FeO

B3. EMP – data and calculated cations for sample IV33

Mineral	b	b	b	b	b	m	m	m	p	p	p
Sample	1iv33_k1	2iv33_k1	4iv33_k1	7iv33_k1	8iv33_k1	9iv33_k1	10iv33_k1	11iv33_k1	5iv33_k1	12iv33_k1	13iv33_k1
SiO_2	34.16	33.73	33.83	33.77	33.67	44.15	44.26	44.12	57.60	57.78	57.68
TiO_2	1.15	2.06	2.03	1.99	1.93	0.45	0.30	0.25	0.00	0.01	0.00
Al_2O_3	19.70	19.58	20.14	19.99	19.90	34.81	34.80	34.50	25.96	25.59	25.66
FeO^*	22.53	22.36	22.20	21.42	22.06	1.83	2.02	2.54	0.09	0.15	0.08
MnO	0.01	0.01	0.00	0.00	0.00	0.00	0.00	0.00	0.00	0.00	0.00
MgO	7.02	6.74	6.90	6.84	6.90	0.41	0.29	0.41	0.00	0.00	0.00
CaO	0.00	0.00	0.00	0.00	0.00	0.00	0.00	0.00	7.18	7.06	7.20
Na_2O	0.27	0.28	0.29	0.29	0.24	1.08	1.11	1.24	8.89	9.03	9.04
K_2O	9.40	9.39	9.45	9.43	9.37	10.20	10.42	9.92	0.04	0.06	0.04
Total	94.23	94.15	94.84	93.73	94.06	92.95	93.22	92.97	99.75	99.68	99.70
Cations											
Oxygens	22	22	22	22	22	22	22	22	8	8	8
Si	5.351	5.293	5.261	5.296	5.277	6.062	6.073	6.071	2.596	2.607	2.603
Al	3.637	3.622	3.691	3.694	3.677	5.634	5.627	5.595	1.379	1.361	1.365
Ti	0.135	0.243	0.238	0.235	0.227	0.047	0.031	0.026	0.000	0.000	0.000
Fe	2.951	2.935	2.887	2.810	2.892	0.210	0.232	0.292	0.003	0.006	0.003
Mn	0.001	0.001	0.000	0.000	0.001	0.000	0.000	0.000	0.000	0.000	0.000
Mg	1.639	1.576	1.599	1.598	1.611	0.085	0.060	0.083	0.000	0.000	0.000
Ca	0.000	0.000	0.000	0.000	0.000	0.000	0.000	0.000	0.347	0.341	0.348
Na	0.083	0.086	0.087	0.088	0.073	0.289	0.295	0.332	0.777	0.790	0.791
K	1.878	1.880	1.875	1.887	1.872	1.787	1.824	1.742	0.002	0.003	0.002
Total	15.676	15.636	15.637	15.609	15.630	14.112	14.142	14.142	5.104	5.109	5.112

b biotite, g garnet, m muscovite, p plagioclase, chl chlorite, il ilmenite; *) total Fe as FeO

Mineral	b	b	b	g	g	g	g	g	g	ilm	m
Sample	14iv33_k2	15iv33_k2	16iv33_k2	1iv33_k2	2iv33_k2	3iv33_k2	4iv33_k2	5iv33_k2	6iv33_k2	20iv33_k2	18iv33_k2
SiO_2	33.63	34.08	33.62	33.05	36.62	36.00	36.17	35.04	35.02	0.24	44.26
TiO_2	2.12	2.08	2.03	0.01	0.02	0.05	0.00	0.03	0.00	52.11	0.56
Al_2O_3	19.55	19.59	19.50	17.78	20.51	20.79	20.56	20.54	20.46	0.28	35.36
FeO^*	22.38	22.35	22.31	35.39	36.05	36.49	35.97	36.00	37.24	45.48	1.70
MnO	0.01	0.00	0.01	1.65	1.59	1.58	1.51	1.45	1.47	0.02	0.00
MgO	6.80	6.91	7.04	1.99	2.45	2.46	2.39	2.40	2.15	0.06	0.32
CaO	0.00	0.00	0.00	1.97	1.88	1.79	1.83	2.16	1.37	0.02	0.00
Na_2O	0.24	0.30	0.28	0.01	0.02	0.00	0.02	0.04	0.02	0.04	1.25
K_2O	9.48	9.45	9.09	0.02	0.00	0.01	0.00	0.02	0.01	0.14	10.28
Total	94.21	94.76	93.88	91.86	99.14	99.17	98.45	97.67	97.74	98.38	93.73
Cations											
Oxygens	22	22	22	12	12	12	12	12	12	6	22
Si	5.279	5.308	5.282	2.968	2.995	2.953	2.981	2.926	2.933	0.012	6.028
Al	3.617	3.597	3.612	1.882	1.977	2.010	1.997	2.022	2.019	0.017	5.676
Ti	0.250	0.244	0.240	0.000	0.001	0.003	0.000	0.002	0.000	1.999	0.057
Fe	2.938	2.912	2.932	2.658	2.466	2.503	2.479	2.514	2.608	1.940	0.194
Mn	0.001	0.000	0.001	0.125	0.110	0.110	0.106	0.103	0.104	0.001	0.000
Mg	1.592	1.605	1.650	0.266	0.299	0.301	0.293	0.299	0.268	0.004	0.065
Ca	0.001	0.000	0.000	0.189	0.165	0.158	0.161	0.193	0.123	0.001	0.000
Na	0.072	0.089	0.087	0.001	0.003	0.000	0.003	0.007	0.004	0.004	0.330
K	1.897	1.878	1.823	0.003	0.000	0.001	0.000	0.002	0.001	0.009	1.785
Total	15.647	15.633	15.626	8.093	8.017	8.039	8.021	8.066	8.060	3.987	14.135

b biotite, g garnet, m muscovite, p plagioclase, chl chlorite, il ilmenite; *) total Fe as FeO

Mineral	m	b	b	b	ilm	m	p	b	g	g	g
Sample	19iv33_k2	21iv33_k3	23iv33_k3	26iv33_k3	25iv33_k3	22iv33_k3	24iv33_k3	28iv33_k4	1iv33_k4	2iv33_k4	3iv33_k4
SiO_2	43.88	33.63	33.31	29.17	0.08	44.42	58.33	33.94	35.89	35.17	35.72
TiO_2	0.49	2.03	2.06	0.11	52.06	0.35	0.00	2.01	0.00	0.01	0.04
Al_2O_3	35.35	19.57	20.05	21.25	0.02	35.07	25.48	19.77	20.63	20.66	20.32
FeO*	1.44	22.74	22.49	22.93	46.15	2.20	0.05	21.73	36.59	37.00	35.80
MnO	0.00	0.01	0.00	0.01	0.23	0.00	0.00	0.00	1.36	1.50	1.30
MgO	0.36	6.81	7.11	11.56	0.05	0.38	0.00	7.19	2.49	2.24	2.51
CaO	0.00	0.00	0.00	0.01	0.01	0.01	6.80	0.01	1.41	1.42	1.77
Na_2O	1.71	0.29	0.31	0.14	0.01	1.20	9.07	0.28	0.04	0.02	0.02
K_2O	9.46	9.49	9.08	3.84	0.02	10.21	0.05	9.45	0.00	0.00	0.00
Total	92.69	94.57	94.40	89.02	98.61	93.84	99.79	94.38	98.40	98.02	97.49
Cations											
Oxygens	22	22	22	22	6	22	8	22	12	12	12
Si	6.017	5.269	5.210	4.750	0.004	6.053	2.623	5.293	2.964	2.931	2.974
Al	5.713	3.613	3.696	4.079	0.001	5.632	1.351	3.635	2.009	2.030	1.994
Ti	0.051	0.239	0.242	0.013	2.001	0.036	0.000	0.236	0.000	0.000	0.002
Fe	0.165	2.980	2.942	3.123	1.973	0.250	0.002	2.834	2.528	2.579	2.493
Mn	0.000	0.001	0.000	0.001	0.010	0.000	0.000	0.000	0.095	0.106	0.092
Mg	0.074	1.590	1.658	2.806	0.003	0.077	0.000	1.672	0.307	0.279	0.312
Ca	0.000	0.001	0.000	0.002	0.000	0.001	0.327	0.002	0.125	0.127	0.158
Na	0.454	0.089	0.094	0.045	0.001	0.316	0.791	0.084	0.006	0.003	0.004
K	1.654	1.897	1.811	0.797	0.001	1.775	0.003	1.881	0.000	0.000	0.000
Total	14.129	15.678	15.653	15.618	3.995	14.141	5.098	15.636	8.034	8.055	8.029

b biotite, g garnet, m muscovite, p plagioclase, chl chlorite, il ilmenite; *) total Fe as FeO

Mineral	g	g	g	m	m
Sample	4iv33_k4	5iv33_k4	13iv33_k4	27iv33_k4	30iv33_k4
SiO_2	35.75	35.36	36.95	44.39	44.39
TiO_2	0.01	0.02	0.03	0.33	0.36
Al_2O_3	20.59	20.61	20.55	35.28	35.44
FeO^*	36.79	36.19	36.24	1.74	1.95
MnO	1.29	1.32	1.32	0.00	0.00
MgO	2.07	2.64	2.53	0.36	0.39
CaO	1.92	1.91	1.48	0.00	0.00
Na_2O	0.02	0.00	0.05	1.08	1.21
K_2O	0.00	0.01	0.01	10.24	10.44
Total	98.44	98.05	99.17	93.42	94.18
Cations					
Oxygens	12	12	12	22	22
Si	2.960	2.935	3.014	6.058	6.028
Al	2.010	2.017	1.976	5.675	5.672
Ti	0.001	0.001	0.002	0.034	0.037
Fe	2.547	2.513	2.472	0.199	0.221
Mn	0.091	0.092	0.091	0.000	0.000
Mg	0.256	0.327	0.308	0.073	0.078
Ca	0.170	0.170	0.129	0.000	0.000
Na	0.002	0.000	0.008	0.285	0.319
K	0.000	0.001	0.001	1.782	1.809
Total	8.036	8.055	8.001	14.105	14.163

b biotite, g garnet, m muscovite, p plagioclase, chl chlorite, il ilmenite; *) total Fe as FeO

Appendix C

C1. Thermocalc 3.26, calculations for sample C71B

```
[display/print with fixed width font (eg Monaco)]

THERMOCALC 3.26  running at 11.55 on Mon 28 Jan,2008, with
tcds55.txt produced at 19:29:59 on 22 Nov 2003 (with sigma fit =  1.067)


an independent set of reactions has been calculated

Activities and their uncertainties

                an       ab      phl      ann     east       mu      cel
a             0.561    0.662   0.0180   0.0930   0.0270    0.757   0.0110
sd(a)/a     0.05000  0.05000  0.22222  0.15000  0.22222  0.10000  0.90909

               fcel       pa       py       gr      alm        q      H2O
a            0.0290    0.529  0.00100 0.000200    0.498     1.00     1.00
sd(a)/a     0.34483  0.05000  0.24300  0.51299  0.15000        0

               sill
a              1.00
sd(a)/a           0

Independent set of reactions
1)  gr + q + 2sill = 3an
2)  2pa + gr + 3q = 3an + 2ab + 2H2O
3)  3east + 6q = phl + 2mu + py
4)  7phl + 12sill = 3east + 4mu + 5py
5)  phl + cel + 2sill = 2east + 5q
6)  ann + q + 2sill = mu + alm
7)  5phl + 3fcel + 12sill = ann + 7mu + 5py

Calculations for the independent set of reactions
(for x(H2O) = 1.0)
        P(T)   sd(P)       a   sd(a)         b        c     ln_K sd(ln_K)
1        3.6    0.65   27.23    0.58  -0.11622    5.359    6.783    0.534
2        2.1    0.43  145.03    0.69  -0.26888    8.330    7.232    0.553
3        5.5    1.46   13.24    1.23   0.01324   -3.490   -0.646    0.770
4        7.8    1.91  196.49    2.16  -0.02862   -7.222  -18.366    2.121
5        7.0    3.34   -0.96    0.96  -0.02776    2.014    1.303    1.036
6        3.8    0.87  -10.05    1.00   0.01144   -2.072    1.400    0.235
7        3.1    2.19  101.88    2.11  -0.03911   -6.167   -8.154    2.072

Average PT (for x(H2O) = 1.0)

Single end-member diagnostic information

avP, avT, sd's, cor, fit are result of doubling the uncertainty on ln a :
a ln a suspect if any are v different from lsq values.
e* are ln a residuals normalised to ln a uncertainties :
large absolute values, say >2.5, point to suspect info.
hat are the diagonal elements of the hat matrix :
large values, say >0.47, point to influential data.
For 95% confidence, fit (= sd(fit)) < 1.49
however a larger value may be OK - look at the diagnostics!

           avP    sd    avT    sd   cor   fit
     lsq   5.7   0.9    634    21 0.871  1.40

             P  sd(P)      T  sd(T)    cor    fit     e*   hat
      an  5.75   0.88    635     22  0.877   1.39   0.24  0.03
      ab  5.69   0.85    637     25  0.775   1.39  -0.19  0.43
     phl  5.74   0.88    636     22  0.880   1.39   0.31  0.06
     ann  5.68   0.90    634     22  0.879   1.40  -0.03  0.06
    east  5.64   0.87    633     22  0.876   1.39  -0.28  0.05
      mu  5.95   0.85    640     21  0.884   1.30  -0.84  0.08
     cel  5.66   0.85    634     21  0.872   1.39   0.48  0.01
    fcel  5.24   0.63    623     16  0.881   0.81   2.75  0.10
      pa  5.69   0.85    637     25  0.775   1.39   0.19  0.43
      py  5.75   0.95    636     24  0.896   1.40  -0.18  0.18
      gr  5.99   0.96    640     23  0.894   1.35  -0.81  0.33
     alm  5.76   0.87    636     22  0.875   1.38  -0.37  0.04
```

```
      q   5.68   0.85    634     21  0.871   1.40      0     0
    H2O   5.68   0.85    634     21  0.871   1.40      0     0
   sill   5.68   0.85    634     21  0.871   1.40      0     0


T = 634°C, sd = 21, P = 5.7 kbars, sd = 0.9, cor = 0.871, sigfit = 1.40
```

C2. Thermocalc 3.26, calculations for sample IV26F

```
[display/print with fixed width font (eg Monaco)]

THERMOCALC 3.26  running at 9.28 on Tue 29 Jan,2008, with
tcds55.txt produced at 19:29:59 on 22 Nov 2003 (with sigma fit =  1.067)


an independent set of reactions has been calculated

Activities and their uncertainties

                 tr     fact       ts     parg      phl      ann     east
a           0.00130   0.0262 0.000170 0.000230   0.0169    0.130   0.0180
sd(a)/a     0.55449  0.25000  1.53393  0.49565  0.24852  0.15000  0.24444

                 an       ab     clin     daph     ames       py       gr
a             0.310    0.820  0.00360   0.0890  0.00710 0.000490 0.000970
sd(a)/a     0.07129  0.05000  0.34167  0.15000  0.30141  0.38571  0.36598

                alm      ilm     geik        q      H2O
a             0.410    0.960  0.00560     1.00     1.00
sd(a)/a     0.15000  0.05000  1.78571        0

Independent set of reactions
1)  15ts + 6gr + 22q = 7tr + 34an + 2clin
2)  8ts + 3gr + 11q = 4tr + 17an + ames
3)  3ts + 2py + 4gr + 12q = 3tr + 12an
4)  5ts + 3gr + 11q = 3tr + 13an + 2H2O
5)  daph + 7gr + 5alm + 19q = 4fact + 13an
6)  6fact + 21an = 11gr + 10alm + 27q + 6H2O
7)  3east + py + 2gr + 6q = 3phl + 6an
8)  45ts + 10ann + 18gr + 66q = 21tr + 10phl + 102an + 6daph
9)  71ts + 22ab + 24gr = 17tr + 22parg + 136an + 8clin
10)  2tr + parg + 16an + 2clin + 3alm + 9geik = 11ts + ab + 9ilm

Calculations for the independent set of reactions
(for x(H2O) = 1.0)
        P(T)   sd(P)       a   sd(a)         b        c     ln_K sd(ln_K)
1        3.1    3.31  109.36   31.34  -0.94659   46.730   74.239   23.572
2        2.4    3.58   48.05   16.65  -0.45528   23.029   38.816   12.581
3        4.5    1.58  -26.19    6.48  -0.38286   21.655   35.046    5.236
4        3.0    2.67  143.14   10.48  -0.50137   19.627   29.054    7.978
5        3.1    0.61  186.38    7.49  -0.58928   33.669   25.651    3.001
6        3.5    0.61   -9.61   11.26   0.58010  -53.657  -38.790    4.790
7        7.0    0.85   -2.20    1.59  -0.21407   10.798   14.281    1.400
8        2.8    3.39  318.67   94.91  -2.74689  136.993  221.560   70.752
9        5.3    4.23  406.76  149.97  -4.08296  171.739  285.585  110.674
10       6.0   11.43 -195.92   23.23   0.31540  -13.299    4.956   23.380

Average PT (for x(H2O) = 1.0)

Single end-member diagnostic information

avP, avT, sd's, cor, fit are result of doubling the uncertainty on ln a :
a ln a suspect if any are v different from lsq values.
e* are ln a residuals normalised to ln a uncertainties :
large absolute values, say >2.5, point to suspect info.
hat are the diagonal elements of the hat matrix :
large values, say >0.53, point to influential data.
For 95% confidence, fit (= sd(fit)) < 1.39
however a larger value may be OK - look at the diagnostics!

            avP    sd    avT    sd   cor   fit
     lsq    5.0   2.2    548    31 0.192  3.65

              P  sd(P)      T  sd(T)    cor    fit     e*   hat
      tr   5.03   2.23    547     31  0.178   3.64   0.52  0.03
    fact   5.69   2.00    547     27  0.185   3.19   3.73  0.03
      ts   5.00   2.22    548     31  0.193   3.64  -0.59  0.00
    parg   5.35   1.88    553     26  0.201   3.06  -5.86  0.02
     phl   4.98   2.23    548     31  0.185   3.65  -0.36  0.01
     ann   4.88   2.19    546     30  0.199   3.57  -1.59  0.01
    east   4.66   2.15    547     30  0.194   3.48   2.95  0.03
      an   4.53   2.58    547     31  0.189   3.62  -0.74  0.13
      ab   5.00   2.21    548     31  0.192   3.63   0.59  0.00
    clin   4.71   2.18    543     31  0.222   3.53  -2.52  0.06
    daph   4.97   2.21    545     33  0.191   3.63  -0.69  0.07
```

ames	4.75	2.06	559	30	0.151	3.36	3.68	0.11
py	4.90	2.21	541	34	0.211	3.60	1.59	0.25
gr	4.55	3.48	549	31	0.039	3.64	0.38	0.65
alm	5.32	2.36	556	37	0.353	3.61	-0.99	0.28
ilm	4.99	2.22	548	31	0.192	3.65	0.01	0.00
geik	4.99	2.22	548	31	0.192	3.65	-0.52	0.00
q	4.99	2.22	548	31	0.192	3.65	0	0
H2O	4.99	2.22	548	31	0.192	3.65	0	0

T = 548°C, sd = 31,
P = 5.0 kbars, sd = 2.2, cor = 0.192, sigfit = 3.65

C3. Thermocalc 3.26, calculations for sample IV33

```
[display/print with fixed width font (eg Monaco)]

THERMOCALC 3.26  running at 10.29 on Mon 28 Jan,2008, with
tcds55.txt produced at 19:29:59 on 22 Nov 2003 (with sigma fit =  1.067)


an independent set of reactions has been calculated

Activities and their uncertainties

                phl      ann     east       an       mu      cel      ilm
a            0.0274   0.0970   0.0290    0.500    0.740   0.0116    0.970
sd(a)/a     0.21934  0.15000  0.21724  0.05000  0.10000  0.86207  0.05000

               geik       py       gr      alm        q      H2O     sill
a           0.00230  0.00170 0.000120    0.540     1.00     1.00     1.00
sd(a)/a     4.34783  0.34118  0.60822  0.15000        0                0

Independent set of reactions
1)  gr + q + 2sill = 3an
2)  3east + 6q = phl + 2mu + py
3)  7phl + 12sill = 3east + 4mu + 5py
4)  4phl + 3cel + 12sill = 7mu + 5py
5)  ann + q + 2sill = mu + alm
6)  3phl + 3ilm + 4gr + 12sill = 3east + 12an + 3geik + alm

Calculations for the independent set of reactions
(for x(H2O) = 1.0)
        P(T)   sd(P)       a   sd(a)         b        c     ln_K sd(ln_K)
1        3.4    0.76   27.23    0.58  -0.11622    5.359    6.949    0.626
2        6.8    1.50   13.24    1.23   0.01324   -3.490    0.045    0.793
3        7.7    2.17  196.49    2.16  -0.02862   -7.222  -18.531    2.419
4        6.1    3.38  128.49    1.99  -0.06447   -6.295   -6.234    3.295
5        3.8    0.87  -10.05    1.00   0.01144   -2.072    1.416    0.235
6        5.4    4.03  181.82    2.85  -0.45978   21.267    9.215   13.316

Average PT (for x(H2O) = 1.0)

Single end-member diagnostic information

avP, avT, sd's, cor, fit are result of doubling the uncertainty on ln a :
a ln a suspect if any are v different from lsq values.
e* are ln a residuals normalised to ln a uncertainties :
large absolute values, say >2.5, point to suspect info.
hat are the diagonal elements of the hat matrix :
large values, say >0.46, point to influential data.
For 95% confidence, fit (= sd(fit)) < 1.54
however a larger value may be OK - look at the diagnostics!

            avP    sd    avT    sd   cor   fit
     lsq    5.3   0.8    648    69 0.658  0.77

              P  sd(P)      T  sd(T)    cor    fit     e*   hat
     phl   5.68   0.92    686     83  0.736   0.65   0.61  0.24
     ann   5.35   0.84    648     70  0.591   0.77   0.01  0.13
    east   5.21   0.83    646     69  0.653   0.57  -1.05  0.04
      an   5.37   0.83    647     69  0.635   0.77   0.11  0.03
      mu   5.26   0.91    645     70  0.658   0.77   0.14  0.11
     cel   5.29   0.83    643     70  0.665   0.74   0.54  0.04
     ilm   5.35   0.82    648     69  0.658   0.77   0.01  0.00
    geik   5.36   0.82    649     69  0.658   0.73  -0.57  0.00
      py   5.20   1.25    635    110  0.858   0.77   0.10  0.66
      gr   5.51   0.88    638     71  0.496   0.73  -0.43  0.49
     alm   5.35   0.84    648     70  0.591   0.77  -0.01  0.13
       q   5.35   0.82    648     69  0.658   0.77      0     0
    sill   5.35   0.82    648     69  0.658   0.77      0     0


T = 648°C, sd = 69,
P = 5.3 kbars, sd = 0.8, cor = 0.658, sigfit = 0.77
```